ZIRCONIUM NITRIDE COATING FABRICATION VIA FLUIDIZED BED CHEMICAL VAPOR DEPOSITION

A Thesis

by

LAURA KATHRYN SUDDERTH

Submitted to the Office of Graduate and Professional Studies of
Texas A&M University
in partial fulfillment of the requirements for the degree of

MASTER OF SCIENCE

Chair of Committee,	Sean McDeavitt
Co-Chair of Committee,	Delia Perez-Nunez
Committee Member,	Raymundo Arroyave
Head of Department	Yassin Hassan

May 2015

Major Subject: Nuclear Engineering

ABSTRACT

In order to reduce the transport and use of high enriched uranium for civilian applications, research reactor fuels are being converted to use low enriched uranium under the Reduced Enrichment for Research and Test Reactors program. A uranium-molybdenum (U-Mo) dispersion type fuel is under investigation for the higher performance reactors that require a higher uranium density than can be provided with current fuel technology. Interactions between U-Mo and the aluminum matrix necessitate the use of a diffusion barrier on the particle surfaces.

A fluidized bed chemical vapor deposition system with an inverted reactor was used to create barrier coatings of zirconium nitride on the surface of U-xMo microspheres. The process utilized the metalorganic precursor tetrakis(dimethylamino)zirconium heated in a Swagelok stainless steel sample cylinder to 51 ± 2 °C. Experiments were performed over three phases: preliminary tests, system modifications, and parametric studies. The time-dependent studies analyzed coating produced after 2-8 days of operation at 100 mL/min precursor carrier flow rate and 500 mL/min fluidization flow rate. Flow rate-dependent studies produced coated samples using a total flow rate of 600 mL/min, with the precursor carrier flow rate ranging from 100-300 mL/min and the fluidization flow rate adjusted accordingly. Ultra high purity argon (99.999%) was used for the precursor carrier and fluidization gas. The CVD reaction was carried out at 280 ± 10 °C with precursor transport tubes heated to 60-75 °C.

Coatings were qualitatively characterized using energy dispersive X-ray spectroscopy, wavelength dispersive X-ray spectroscopy, and X-ray distribution mapping. Zirconium-based coatings up to 2.2 ± 0.3 μm thick after 2 days of deposition. The estimated coating thickness was not significantly impacted by extending the duration of the deposition process or increasing the precursor carrier gas flow rate. Despite apparent precursor transport throughout the duration of the experiment, the majority of the coating deposition seems to have occurred within the first 24 hours of the experiment. Imaging of the microsphere cross-sections provided evidence of the formation of uranium oxide,

zirconium oxide, and zirconium nitride layers on the surface of the particles, with nitrogen deposition becoming more favorable further from the bulk U-Mo surface.

ACKNOWLEDGMENTS

I would like to thank my committee chairs, Drs. Sean McDeavitt and Delia Perez-Nunez, for their support and guidance throughout this research project. I would also like to thank my committee member, Dr. Raymundo Arroyave for his time and attention.

I would like to acknowledge Marie Arrieta for her work in this project prior to my involvement. Her design work and advice provided me with a smooth transition into the project and enabled this study to be performed.

I would like to thank my friends and colleagues at the Fuel Cycle and Materials Laboratory, Connor Woolum, Jeffrey Clemens, and Josh Concklin for all their assistance and advice. I would also like to thank Dr. Ray Guillemette (Geology and Geophysics Department, TAMU) for his assistance with the electron microprobe and data analysis.

I want to extend my gratitude to the Idaho National Laboratory and Dr. Dennis Keiser for supporting this project, providing coating materials and experiment funding as well as guidance in this research. This project was partially supported by the U.S. Department of Energy through the Idaho National Laboratory under the National Nuclear Security Administration's Global Threat Reduction Initiative (TEES Contract M1401754).

Finally, a special thanks to my mother and father for all their support and encouragement. I could not have done this without them.

NOMENCLATURE

GTRI	Global Threat Reduction Initiative
RERTR	Reduced Enrichment for Research and Test Reactors
DOE	Department of Energy
INL	Idaho National Laboratory
PVD	Physical Vapor Deposition
ALD	Atomic Layer Deposition
CVD	Chemical Vapor Deposition
FB	Fluidized Bed
MO	Metalorganic
TAMU	Texas A&M University
TDMAZ	Tetrakis (dimethylamino) Zirconium
UHP	Ultra High Purity
RV	Reaction Vessel
EPMA	Electron Probe Micro-Analyzer
SEM	Scanning Electron Microscope
EDS	Energy Dispersive Spectroscopy
WDS	Wavelength Dispersive Spectroscopy
BSE	Back-Scattered Electron
SE	Secondary Electron
XRD	X-Ray Diffraction
U-7Mo	Uranium with 7% Molybdenum (by weight)
U-8Mo	Uranium with 8% Molybdenum (by weight)

TABLE OF CONTENTS

Page

LIST OF FIGURES

Page

LIST OF TABLES

Page

1. INTRODUCTION

The objective of this study was to demonstrate the efficacy of FB-CVD for producing diffusion barrier coatings on particulate fuel. A ZrN coating was selected as a candidate barrier for U-Mo particles dispersed in an aluminum matrix because it is chemically inert to the component materials and exhibits favorable diffusivity and thermal properties. The following sections in this chapter describe the context of the RERTR program (Section 1.1) and a brief overview of the research conducted (Section 1.2).

1.1 The Reduced Enrichment for Research and Test Reactors Program

High enriched uranium (HEU) has been used around the world for decades as a fuel in nuclear energy systems used for research and teaching, isotope production, and even naval propulsion [1]. In order to promote peaceful uses of nuclear energy, the Atoms for Peace program, announced by Dwight Eisenhower in 1953, provided equipment and information for research reactors to institutions both within the U.S. and throughout the world [2]. Although these reactors initially used low-enriched uranium (LEU), HEU was introduced to meet demands for higher specific powers and neutron fluxes. In the mid-1960s, production of HEU for nuclear weapons in the U.S. was discontinued [1], and by the late 1970s, the U.S. was exporting about 700 kg/year of HEU for foreign research and test reactors [2].

The regular export of HEU inspired concerns about potential diversion of HEU for nuclear weapons. As a result, the U.S. Department of Energy (DOE) created the Reduced Enrichment for Research and Test Reactor (RERTR) program in 1978 with the purpose of developing technology to remove the need for the use of HEU in civilian applications while maintaining the services provided by the existing nuclear systems [2]. The objective is to convert the fuel in research and test reactors around the world from HEU to LEU.

In order to convert the fuel and maintain normal operation of the reactor, the average fissile material atom density in the fuel had to be maintained. When converting fuel from HEU to LEU, there is a reduction in the number density of fissile (i.e. ^{235}U)

atoms in the uranium phase. This loss was compensated for by increasing the amount of uranium in the fuel, expressed as uranium density, thereby enabling the ^{235}U number density the fuel to remain nearly constant [2].

In 1978, the fuels in use in western designed reactors were plate-type fuels with UAl_x-Al (1.7 gU/cm^3) and U_3O_8-Al (1.3 gU/cm^3) dispersions enriched to 93% ^{235}U and rod-type $UZrH_x$ (0.5 gU/cm^3) enriched to 70% ^{235}U [2]. Low enriched dispersion fuels have been demonstrated and installed with uranium loadings up to 2.3 gU/cm^3 for UAl_x-Al [2], 3.2 gU/cm^3 for U_3O_8-Al, and 4.8 gU/cm^3 for U_3Si_2-Al [3]. The first research reactor converted to LEU was at the University of Michigan in December 1981 using the UAl_x-Al plate-type fuel [2]. Since 1988, more than 30 research reactors have been converted using LEU U_3Si_2-Al dispersion fuel. Conversion of the higher-power density reactors required a uranium density of 8-10 gU/cm^3 in the fuel plates. Fuel fabrication using existing commercial processes limits the loading of the fuel phase in the plates to 55% by volume. To meet the desired fuel characteristics, a uranium density of 14.5 gU/cm^3 in the fuel phase is required. Metallic uranium alloys and high density intermetallic fuels (e.g., U_6Me) meet this criteria. However, intermetallics have been shown to exhibit high swelling rates at relatively low burnup. For example, irradiation tests of LEU U_6Fe-Al dispersion fuels at the Oak Ridge Research Reactor (ORR) showed extensive fission gas bubbles at burnups as low as 20% and consequently fuel plate failure by 40% burnup [4]. Similarly irradiation tests of U_6Mn-Al dispersion fuels at ORR showed extensive and linked fission gas bubbles at low burnup [5]. The intermetallic class was thus suspected to exhibit similar irradiation behavior and were not further considered by the RERTR program [2].

For pure uranium metal, the orthorhombic α phase that exists at low temperatures exhibits a high rate of growth and swelling under irradiation [3]. The cubic γ has stable irradiation behavior but is thermodynamically unstable at lower temperatures. To stabilize the γ phase, transition metals with low neutron capture cross sections can be alloyed with the uranium metal. Transition metals with higher atomic numbers have a greater ability to stabilize the high temperature phase as more d-electrons will participate in bonding.

However, the solubility of the metals decreases as atomic size differences increases, promoting the formation of intermetallic compounds rather than a solid solution. The elements identified to form a solid solution with the γ uranium phase and maintain stability at lower temperatures include Zr, Nb, Ti, and Mo.

Irradiation behavior data eliminated all candidates except U-Nb-Zr and U-Mo [2]. Initial tests, RERTR-1 and RERTR-2, at the Advanced Test Reactor at Idaho National Laboratory (INL) up to a ^{235}U burnup of 70% showed that U-Mo alloys with at least 6 wt% Mo showed low swelling and stable irradiation behavior exhibited by a distribution of small, stable fission gas bubbles [6]. Meanwhile, alloys with 4 wt% Mo exhibited growth of large fission gas bubbles. Furthermore, fuel-matrix interactions were shown to occur more rapidly in in alloys with lower Mo content. The U-Nb-Zr alloys were found to exhibited characteristics of break-away swelling, thus were not further considered [2].

Further tests continued to show good irradiation behavior in the U-Mo/Al dispersion fuel with loadings up to 8 gU/cm^3. Higher uranium densities in may be possible monolithic U-Mo/Al fuel [2]. RERTR-3 irradiation experiments of the U-xMo/Al fuel (x = 6.7-10.6% by weight) showed that swelling in the U-Mo alloys under irradiation was largely due to U-Mo/Al interdiffusion, with lower Mo content alloys (i.e. U-7Mo) exhibiting higher rates of interaction than higher Mo content alloys (U-10Mo) [7]. The interaction product was determined to be stable up to 70% ^{235}U burnup and 300 °C, exhibited by few small bubbles and isolated pockets of bubbles within the layer. However, the growth of the interdiffusion layer and coupled with the loss of aluminum matrix causes the thermal conductivity to decrease and consequently increases fuel temperature [2]. Further tests classified under RERTR-4 and RERTR-5 experiments continued to show predictable irradiation behavior, but the interaction layer begins to develop large fission gas pores at high power densities [8]. At high temperatures and burnup, the interaction layer between the fuel particle and matrix has been observed to become amorphous, exhibiting a viscous behavior [9]. The low material viscosity and high fission gas diffusivity enables fission gas bubbles to form and grow. The bubbled interconnect in the interdiffusion layer and lead to fuel plate failure. Silicon was implemented to the matrix

beginning in RERTR-6 experiments to reduce the growth of the interaction layer [2]. The effect of silicon addition continued to be tested in later irradiation experiments with weight fractions of silicon up to 3.5%, and was shown to mitigate the development of the interaction layer [10].

Irradiation tests of the U-Mo/Al dispersion fuel plates were performed at the OSIRIS reactor up to 67.5% peak burnup [11]. The IRIS-1 experiment showed accumulation of fission products between the matrix and interaction layer, identified as $(U,Mo)Al_7$. However, the interface did not exhibit significant porosity, leading to a negligible contribution to the plate swelling (less than 6%). Irradiation tests of the interaction layer were also performed in the FUTURE rig of the Belgian Reactor 2 reactor at SCK-CEN with burnups up to 32.8% ^{235}U [12]. These results identified the interaction layer as $(U,Mo)Al_3$ and $(U,Mo)Al_4$. Fission products were similarly observed to build up at the interface between the interaction layer and matrix, but was not believed to significantly contribute to the swelling of the fuel. Rather, the observed swelling (up to 13%) was largely attributed to the formation of the interaction layer weakening the cohesion of the fuel meat and resulting thermal-mechanical stresses.

One proposed solution to mitigate the interaction of the fuel material with the aluminum matrix is to create a diffusion barrier coating on the surfaces of the U-Mo. Candidate barrier coatings have been reviewed and selected under the RERTR program [13]. Key selection criteria included chemical inertness to the U-Mo alloy and the Al matrix, low diffusivity, relatively high thermal conductivity, and chemical stability. Such compounds include nitrides of refractory metals and silicides. For reactor applications, the diffusion barrier should also exhibit good irradiation behavior, uniform thickness and structure across the substrate surface and low interaction cross sections with thermal neutrons. For these reasons, mononitrides of zirconium and titanium were identified as materials of particular interest. More specifically, zirconium mononitride (ZrN) was the object of the FB-CVD coating experiments described in Chapters 3-5.

1.2 FB-CVD Coating of ZrN onto U-Mo Powder

FB-CVD has been studied as a candidate process to create ZrN coatings on U-Mo powders. Other methods considered by the RERTR program include physical layer deposition (PVD) and atomic layer deposition (ALD), but these methods are not pertinent to the experimental work reported here. Most PVD methods involve a "line-of-sight" deposition process and high vacuum environments, making it difficult to produce uniform coating on complex geometries and scale to commercial production [14]. ALD and CVD are non-line-of-sight deposition processes. In ALD, deposition occurs via a two-pulse exchange reaction that produces one atomic layer of coating per cycle [15]. In CVD atoms or molecules are deposited by reduction or interaction of one or more chemical vapor precursors onto a heated surface and volatile byproducts of the reaction are transported away from the surface [16]. Although each of the above process are considered viable processes for coating U-Mo, CVD was chosen for this study to its capability for high deposition rates, uniform coatings of complex geometries, and scalability. For dispersion plate-type fuels, U-xMo microspheres must be coated uniformly. This may be accomplished by fluidizing, or suspending in a gas stream, the particles within a chamber, minimizing particle-particle contact and allowing the reactive gas to flow around each particle. This process is known as fluidized bed CVD (FB-CVD).

The experiments carried out in this study involved utilizing an inverted FB-CVD reactor, described in Chapter 3. This lab scale design was used to deposit a zirconium nitride barrier coating approximately 10 g of U-Mo microspheres (63-125 μm) at low temperature (280 ± 10 °C). Ultra high purity argon (99.999%) was used for the precursor carrier and fluidization gas. The process utilized the metalorganic precursor tetrakis(dimethylamino)zirconium heated in a Swagelok stainless steel sample cylinder to 51 ± 2 °C and heated to 60-75 °C during vapor transport. A rotary vane vacuum pump was attached at the back end of the system facilitate particle fluidization in the reaction vessel. Detailed procedures and experimental conditions are provided in Chapter 3.

Experiments were performed over three phases: preliminary tests, system modifications, and parametric studies. The preliminary tests were used to show the coating

capabilities of the system and reproduce findings described by Arrieta [17]. The second phase consisted of a series of system modifications and tests designed to improve the performance of the system with emphasis on improving precursor transport and particle fluidization and reducing of system leaks. Parametric studies were performed using two sets of experiments: duration studies and flow rate studies. The time-dependent studies analyzed coating produced after 2-8 days of operation at 100 mL/min precursor carrier flow rate and 500 mL/min flow rate. Flow rate-dependent studies produced coated samples using a combined flow rate of 600 mL/min, with the precursor carrier flow rate ranging from 100-300 mL/min and the fluidization flow rate adjusted accordingly.

The coatings produced were qualitatively characterized using an Electron Probe Micro-Analyzer (EPMA, Cameca Model SX50). Two types of samples were analyzed from each experiment: loose sphere surfaces and polished cross-sections. The samples were imaged using back-scattered electron (BSE) and secondary electron (SE) techniques. The composition of the sphere surfaces were characterized using energy dispersive X-ray spectroscopy (EDS) and wavelength dispersive X-ray spectroscopy (WDS) scans across energies corresponding to characteristic X-ray of suspected elements. The coating structure and thickness was observed using the polished cross-sections of the particles by WDS and X-ray distribution mapping across the boundary of the spheres. The results of each experiment are described in Chapter 4.

The principal findings and results describe zirconium-based coatings with estimated thickness of up to 2.4 ± 0.4 μm. The target thickness of 1-2 μm was accomplished within 2 days of deposition. The coating thickness was not significantly impacted by prolonged exposure to the chemical precursor despite apparent continuous precursor transport, and the majority of the coating deposition seems to occur within the first 24 hours of the experiment. Increasing the precursor carrier gas flow rate also did not impact the thickness of the coating, but particular combinations of flow rates may improve the quality of the coatings. Imaging of the microsphere cross-sections provided evidence of uranium oxide, zirconium oxide, and zirconium nitride layers formed within the coating, with nitrogen deposition becoming more favorable as the chemical potential for

oxygen deposition decreases further from the bulk U-Mo surface. These findings and further observations are discussed in more detail in Chapter 5, and a summary of the experiments and recommendations for further studies are described in Chapter 6.

2. BACKGROUND

Fluidized bed chemical vapor deposition is a powder coating process that comprises a bed of particles suspended in a flowing gas as the reaction zone [18]. In this zone, the vapor chemical precursor deposits the desired coating on the particle surfaces. This chapter discusses processes and technology relevant to the deposition of ZrN. Section 2.1 reviews some of the processes available for thin film deposition on powder substrates, and Section 2.2 discusses chemical precursors for ZrN coatings. Section 2.3 presents a summary of the state of development of the lab-scale FB-CVD system at the onset of this study.

2.1 Chemical Vapor Deposition

2.1.1 Overview of CVD for Coating Processes

Chemical vapor deposition denotes a family of processing techniques that comprise the creation of material layers through the conversion of vapor-phase chemicals (often in high vacuum) through either thermal decomposition or chemical reduction at a heated substrate surface [16]. The process of CVD occurs in a sequence of steps [19]. First, the reactant gases enter the reaction chamber by forced flow. Next, the gases diffuse through the boundary layer then come in contact with the substrate surface. The deposition reaction takes place on the surface, and the gaseous by-products are diffused away from the surface through the boundary layer. The slowest of these steps determines the deposition rate. The stepwise CVD process is shown in Figure 2-1. The CVD process is not a line-of-sight process, therefore complex geometries may be readily coated. CVD equipment does not typically require ultrahigh vacuum and may be easily scaled and adapted to process variations [20].

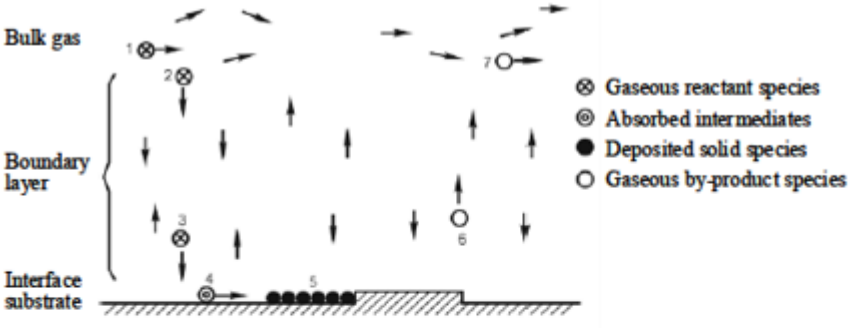

1. Mass transport of reactant gaseous species to vicinity of substrate
2. Diffusion of reactant species through the boundary layer to the substrate surface or homogeneous chemical reactions to form intermediates;
3. Adsorption of reactant species or intermediates on substrate surface;
4. Surface migration, heterogeneous reaction, inclusion of coating atoms into the growing surface, and formation of by-product species;
5. Desorption of by-product species on the surface reaction;
6. Diffusion of by-product species to the bulk gas; and
7. Transport of by-product gaseous species away from substrate (exhaust).

Figure 2-1. Sequence of the CVD mechanism [19].[1]

A nominal CVD reaction may be described by the thermodynamics of the reactants and products. In CVD, a transfer of energy occurs when the gaseous precursor compounds react to form a solid deposit on the substrate and gaseous by-products [20]. The relative magnitude and exothermic or endothermic nature of the free energies describes the driving force for the reaction. The Gibbs free energy of the reaction (ΔG_r) may be calculated from the free energy of the reactants and products by Eq. 1 [19]. If the $\Delta G_f(T)$ of the individual species at a given temperature, T, is not known, it can be calculated from the enthalpy of formation, $\Delta H_f^0(T)$, the standard entropy, $\Delta S^o(T)$, and heat capacity, $C_p(T)$, using Eq. 2. A favorable reaction will be exothermic, typically designated as a negative value of $\Delta G_r(T)$.

[1] Springer and the Engineering Materials and Processes, Chemical Vapour Deposition: An Integrated Engineering Design for Advanced Materials, 2010, Page 2, Chapter 1 Introduction to Chemical Vapour Deposition, Yongdong Xu and Xiu-Tian Yan, Figure 1.1b, original copyright notice is given to the publication in which the material was originally published, by adding; with kind permission from Springer Science and Business Media.

$$\Delta G_r = \Sigma \Delta G_f(\text{products}) - \Sigma \Delta G_f(\text{reactants}). \quad (1)$$

$$\Delta G_f(T) = \Delta H_f^0(298) + \int_{298}^{T} C_p dT - TS^0(298) - \int_{298}^{T} \left(\frac{C_p}{T}\right) dT. \quad (2)$$

The rate and quality of the reaction is also related to kinetics, which is a function of temperature. The kinetic factors that impact a functional CVD process include transporting the reactant gas to the surface of the substrate, the temperature-dependent reaction rates at the substrate surface, and the physical interactions between the process gases and the substrate.

For CVD with gaseous precursors at a relatively high pressure, the precursor gases exhibit fluid behavior as they flows across the solid surface with a boundary layer near the surface and a free stream region far from the surface [19]. The thickness of the boundary layer is defined as the distance from the solid body to the fluid layer at which the flow velocity reaches 99% of the free stream velocity, as illustrated in Figure 2-2. The thickness of the boundary layer, Δy, is described by Eq. 3, where x is the distance from inlet in flow direction, and R_e is the Reynolds number [20]. The Reynolds number is a dimensionless parameter that characterizes the flow of a fluid by relating inertial forces for a particle in terms of particle diameter, D_p, fluid density, ρ_f, and fluid velocity, v_f to the viscous force in terms of fluid viscosity, μ_f, in Eq 4. From these equations, a low pressure and low temperature system will have a thinner boundary layer. A system with a thin boundary layer will have a faster rate of diffusion through the boundary layer, facilitating the transport of the reactants to the surface. Since the two major rate limiting steps in a CVD system are the diffusion of the reactants through the boundary layer and the surface reaction kinetics, the growth rate in a system with a thin boundary layer is limited by surface kinetics, whereas a system with a thick boundary layer is limited by the diffusion of the reactant gas through the boundary layer.

$$\Delta y = \sqrt{\frac{x}{R_e}} \quad (3)$$

$$R_{e,p} = \frac{\rho_f v_f D_p}{\mu_f} \quad (4)$$

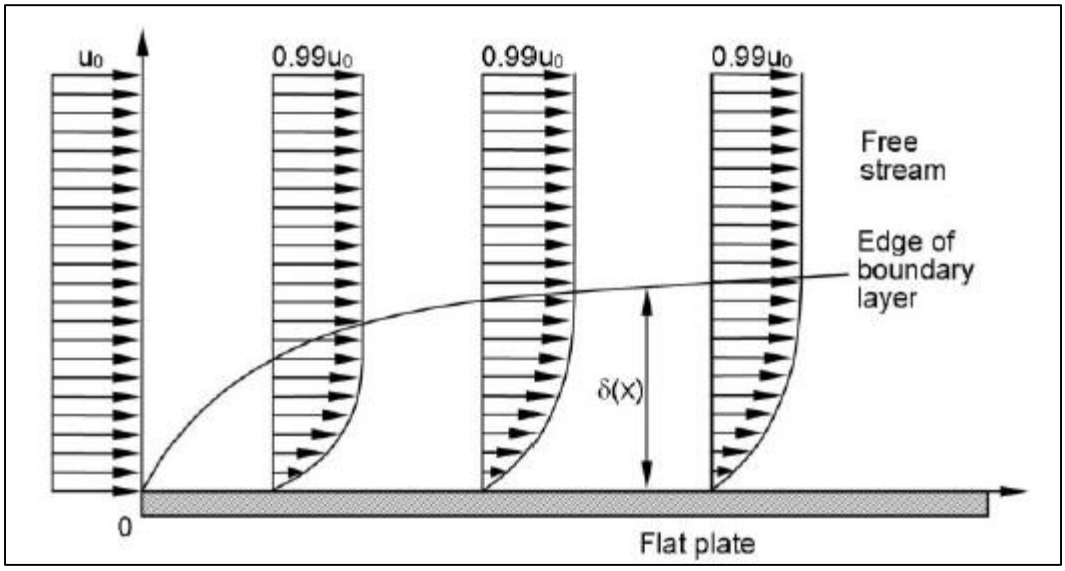

Figure 2-2. Profile of a boundary layer along a flat plate [19].[2]

The mechanism by which a film is deposited on the surface by CVD is the subject of debate in the literature. The properties of the substrate affects the quality and behavior of the deposit as well as the rate of nucleation at the very beginning of the deposition [20]. Certain factors known to control the nature and properties of the deposit include the lattice parameters and the coefficient of thermal expansion of substrate and coating. For example, epitaxial growth, or the growth of a crystalline film on a crystalline substrate, cannot occur if the difference between the lattice parameters of the substrate and deposit is too large. If the difference between the coefficient of thermal expansion between the substrate and deposit is also too large, stresses introduced during the cool down period can cause cracking and spalling of the coating. This phenomenon is of particular concern for deposition processes that occur at a high temperature.

The properties of a CVD deposit are dependent on its structure [20]. The structure of the CVD material may be classified by three major types: columnar grains with domed

[2] Springer and the Engineering Materials and Processes, Chemical Vapour Deposition: An Integrated Engineering Design for Advanced Materials, 2010, Page 63, Chapter 2 Physical Fundamentals of Chemical Vapour Deposition, Yongdong Xu and Xiu-Tian Yan, Figure 2.17, original copyright notice is given to the publication in which the material was originally published, by adding; with kind permission from Springer Science and Business Media.

tops, faceted columnar grains, and equiaxed fine grains. Examples of these structures are shown in Figure 2-3. The nature of the structure may be controlled by the deposition parameters, including temperature, pressure, and supersaturation of the reactants. Pressure controls the thickness of the boundary layer and the degree of diffusion. Low pressure minimizes the diffusion process, allowing the surface kinetics to control the reaction rate. This produces fine-grained microstructures in the deposit. Low temperatures also produce fine-grained deposits as at higher temperatures, the uninterrupted grain growth toward the reactant source causes columnar microstructures. Supersaturation also produces fine-grained structures. A fine-grained microstructure is preferred in diffusion barriers because the columnar microstructure allows faster diffusion along the grain boundaries. As the thickness of the film increases, the grain size also increases, making the columnar-grain structure become more pronounced.

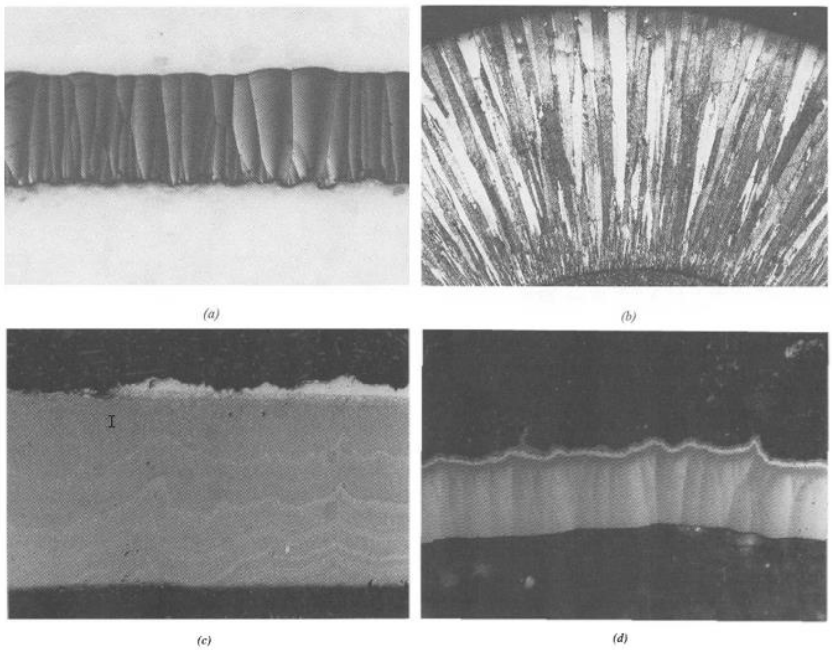

Figure 2-3. Examples of CVD structures: (a) columnar grains with domed tops, (b) faceted columnar grains, (c) equiaxed fine grains, (d) mixed structures [20].[3]

[3] Reprinted from Handbook of Chemical Vapor Deposition (CVD), 2nd Edition, Hugh O. Pierson, Chapter 2 Fundamentals of Chemical Vapor Deposition, Pages 61-62, Copyright (1999), with permission from Elsevier.

Forcing the fluid through a series of pipes and valves introduces variations in temperature and pressure. Therefore the transport system must be kept at a high enough temperature for the precursor to remain in the gas phase. However, if the temperature is sufficiently high, gas-phase precipitation may occur in which a CVD reaction occurs in the gas phase instead of at the surface of a substrate [20]. These precipitated particles may become incorporated into the deposit forming defects and poor adhesion. System contaminants (oxygen, moisture, air, etc.) may interfere with the expected reaction and introduce additional possible reactions. The sensitivities of the precursor chemicals must also be considered in the system.

2.1.2 CVD on Particulate Substrates

For CVD systems with particulate substrates, achieving a uniform coating requires that the precursor gas has sufficient contact with the entire surface of each particle [17]. To reduce the effect of particle-particle contact, the particle bed may be configured such that the particles are in constant motion relative to each other and other surfaces. Several methods have been developed to generate movement of particles in gas-solid reactors [21]. Many of these techniques involve mechanically moving or rotating the population. Although these methods generate particle motion, the particle surface may remain in contact. Since particle contact interferes with evenly depositing a species, the most popular of these methods for CVD applications is the fluidized bed reactor.

Fluidization is the process through which the behavior a bed of solid particles is made to resemble that of a liquid [21]. This is accomplished by a fluid flowing upwards through the bed such that the force exerted on the particles exactly counteracts their weight. This way, the resulting fluidized bed is held in place by the counteracting drag forces and gravity. The state of fluidization is determined by the flow rate of the fluid, illustrated in Figure 2-4 [18]. At a low flow rate, the fluid travels through the void spaces in a stationary (fixed) bed. As the flow rate increases, the particles begin to move apart and develop into an expanded bed. At a critical velocity, the particles are just suspended in the fluid stream such that the forces acting on the particle are balanced, resulting in a

bed at minimum fluidization. Above minimum fluidization in a gas-solid system, instabilities through bubbling can be observed, and the particle bed does not continue to expand.

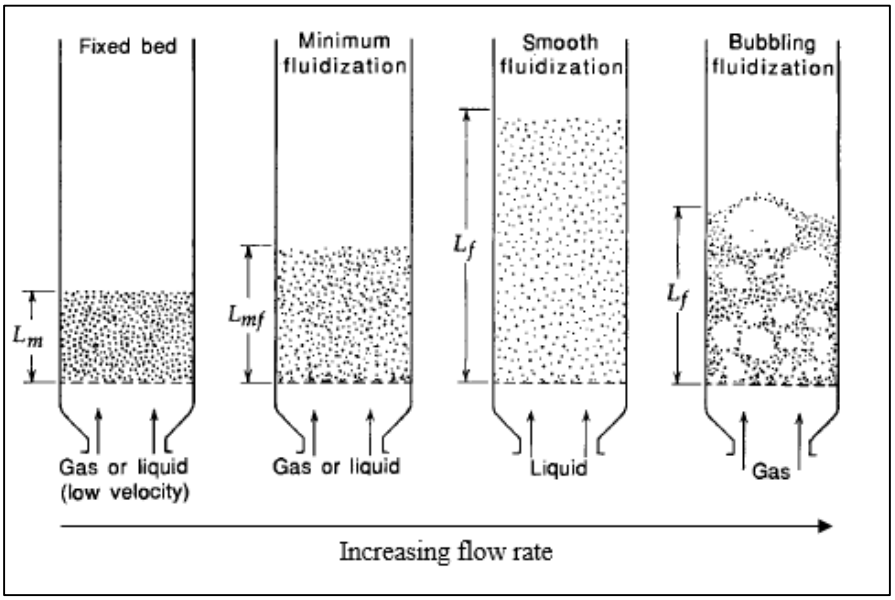

Figure 2-4. Stages of fluidization [18].[4]

The fluid flow through a bed of flow substrates exhibits different behavior than that along a flat plate. A gas stream flowing upward through a bed of particles experiences a pressure drop due to the particles resisting flow that increases with gas velocity [19]. The particle bed will become fluidized at a minimum gas velocity in which the pressure drop across the bed is equal to the weight of the particles. The minimum fluidization velocity, μ_{mf}, can then be calculated corresponding to the critical pressure drop using Eqs. 5 and 6, where d_p is the particle diameter, μ is the viscosity of the gas, and ρ_g and ρ_p are the densities of the gas and particle, respectively [19].

[4] Reprinted from Fluidization Engineering, 2nd Edition, Daizo Kunii and Octave Levenspeil, Chapter 1 - Introduction, Page 2, Copyright (1991), with permission from Elsevier.

$$\mu_{mf} = \frac{\mu}{d_P \rho_g}\left[\left(33.7^2 + 0.0408\frac{d_P^3 \rho_g (\rho_P - \rho_g) g}{\mu^2}\right)^{\frac{1}{2}} - 33.7\right], \quad d_P > 100\ \mu m. \tag{5}$$

$$\mu_{mf} = \frac{(\rho_P - \rho_g)^{0.934} g^{0.934} d_P^{18}}{1111 \mu^{0.87} \rho_g^{0.066}}, \quad d_P < 100\ \mu m. \tag{6}$$

This method, however, does not account for the effects of the particle shape. An alternative method, described by Arrieta, was found to provide a closer estimate for the fluidization requirements, although experimental values still deviated from those predicted [17]. The Archimedes number, determined by Eq. 7, is a dimensionless number used to describe the ratio of external forces to internal viscous forces, where g is the gravitational force, d_p is the particle diameter, μ is the viscosity of the gas, and ρ_g and ρ_p are the densities of the gas and particle, respectively [18]. The shape factor, φ, can be used to describe variation from a spherical shape, or sphericity, of a particle to an equivalent sphere with the same diameter as the particle measured [22]. The Archmides number can then be used to determine the Reynolds number required for minimum fluidization, Re_{mf}, based on the shape factor of the particle population using Eqs. 9-11 [22]. Since a sample of particulate substrates consists of a distribution of particle sizes, the upper bound of the fluidization velocity should be calculated using the largest particles in the population using Eq. 12 [23].

$$Ar = \frac{g d_p^3 \rho_p (\rho_p - \rho_g)}{\mu^2} \tag{7}$$

$$\varphi = \frac{\text{Surface area of equivalent sphere}}{\text{Surface area of particle}} \tag{8}$$

$$Re_{mf} = \left(29.5^2 + 0.357Ar\right)^{\frac{1}{2}} - 29.5, \qquad 0.8 \le \varphi \le 1.0 \tag{9}$$

$$Re_{mf} = \left(32.1^2 + 0.0571Ar\right)^{\frac{1}{2}} - 32.1, \qquad 0.5 \le \varphi \le 0.8 \tag{10}$$

$$Re_{mf} = \left(25.2^2 + 0.0672Ar\right)^{\frac{1}{2}} - 25.2, \qquad 0.1 \le \varphi \le 0.5 \tag{11}$$

$$v_T = \frac{2gD_P^2(\rho_p - \rho_f)}{18\mu} \tag{12}$$

The difference in the Reynolds numbers for fluidized particulate substrates versus that for a flat plate corresponds to the relative gas flow boundary layer thickness. The corresponding thickness of the boundary layer may be related to the coating deposited, as a thinner boundary layer would exhibit a higher diffusion rate of the reactive vapor species through the boundary layer to the substrate surface [24].

2.1.3 Non-CVD Powder Coating Methods

The deposition of a diffusion barrier coating on powder substrates may be accomplished by chemical vapor deposition (CVD), physical vapor deposition (PVD), and atomic layer deposition (ALD). The CVD method was applied in this study and is more fully described in following sections. A brief description of PVD and ALD is presented here for comparison.

For PVD, a selected chemical or pure substance is vaporized from a solid or liquid precursor by either thermal heating or energetic particle bombardment [19]. The vapor species is transported through a vacuum or low pressure gaseous environment to a heated substrate where it condenses on the surface. The target compounds may be formed on the surface by the reaction of the depositing material with a reactive gas species, such as nitrogen or oxygen or with the assistance of a co-depositing material. PVD may be used to deposit thin films, multilayer coatings, graded composition coatings, or thick coatings. PVD requires a linear line-of-sight for material streaming between the source and substrate. This creates challenges for the production of uniform coatings on complicated geometries [14]. PVD processes also require ultrahigh vacuum working environments which may also be challenging to adapt to larger-scale industrial capacity [19]. However, PVD provides low cost processing with material and multi-layer flexibility [25].

The main techniques used in PVD include vacuum evaporation, sputter deposition, arc vapor deposition, and ion plating, shown in Figure 2-5 [16]. Vacuum evaporation thermally vaporizes the source material in a vacuum environment to prevent interactions while it is transported from the source to the substrate. Sputtering deposition physically ejects atoms from a solid source surface, or target. This non-thermal vaporization process

occurs through momentum transfer of bombarding ions. The emitted atoms deposit directly onto a substrate surface in a vacuum environment [25]. This process provides a long-lived source with the ability to vaporize the source in any direction [16]. Arc vapor deposition uses a low voltage arc to vaporize a cathode or anode material. The ionized vapor is then deposited on the surface of a substrate. In the ion plating method, ions are periodically bombarded on the depositing film to modify the properties of the film. The effects of the bombardment are dependent on the energy, flux, and mass of the bombarding species. The depositing material may then be vaporized by a variety of techniques, including evaporation, sputtering, or arc erosion.

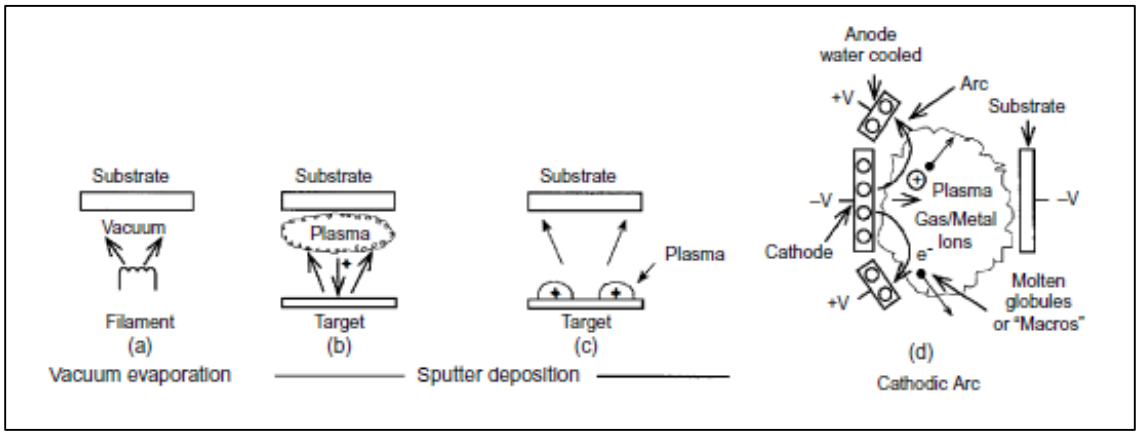

Figure 2-5. PVD processes and schematics [16].[5]

Production of ZrN barrier coatings for U-Mo dispersion fuel plates via PVD is investigated under the Surface Engineering of Low ENrIched Uranium-Molybdenum (SELENIUM) fuel development project [25]. A magnetron sputtering process, known as Sputtering Tool for Engineering Powder Surfaces & Deposition Reactor for Uranium based model Systems (STEPS&DRUMS), was developed for coating U-Mo particulate fuel. The reaction vessel, shown in Figure 2-6, consists of a rotating drum at one end to generate particle movement and coat the particles (STEPS) and a sample holder to sputter

[5] Reprinted from Handbook of Physical Vapor Deposition (PVD) Processing, 2nd Edition, Donald M. Mattox, Chapter 1 - Introduction, Page 4, Copyright (2010), with permission from Elsevier.

films on flat surfaces at the other end (DRUMS). Zirconium nitride deposition is accomplished using ultra-high purity zirconium metal targets and adding high purity nitrogen gas to the argon atmosphere for up to 7 hours. This process has been shown to produce smooth and homogeneous ZrN coatings about 1 µm thick. Diffraction analysis confirmed that the coating consisted of the cubic-ZrN phase [26]. Characterization of a sample of coatings by SEM/TEM revealed columnar microstructures with porous boundaries within the ZrN thin film. Following fuel plate fabrication, limited interactions between the coating and Al matrix occurred, but an interaction zone between the U-Mo and ZrN was observed.

Figure 2-6. STEPS&DRUMS setup (left) and schematic (right) [25].[6]

Atomic layer deposition is a deposition technique accomplished by alternatively exposing the substrate to gaseous precursors [27]. One atomic layer of the desired coating is deposited per cycle. Each cycle consists of two steps, in which one atomic layer of the first reactant is adsorbed on the surface of the substrate in the first step. The second reactant, such as NH_3, H_2O, O_2, N_2 or H_2, then initiates an exchange reaction on the substrate surface, as shown in Figure 2-7. The schematic depicts two types of methods in

[6] Reprinted from Journal of Nuclear Materials, Volume 440, A. Leenaers, S. Van den Berghe, C. Detavernier, Surface engineering of low enriched uranium-molybdenum, Pages 220-228, Copyright (2013), with permission from Elsevier.

the second half-cycle: thermal ALD and plasma-assisted (or enhanced) ALD. Thermal ALD enhances the reaction rate using increase substrate temperatures in a thermally driven process. In, Plasma-enhanced ALD (PEALD) the second reactant is a particular species of plasma that energetically enhances the exchange reaction.

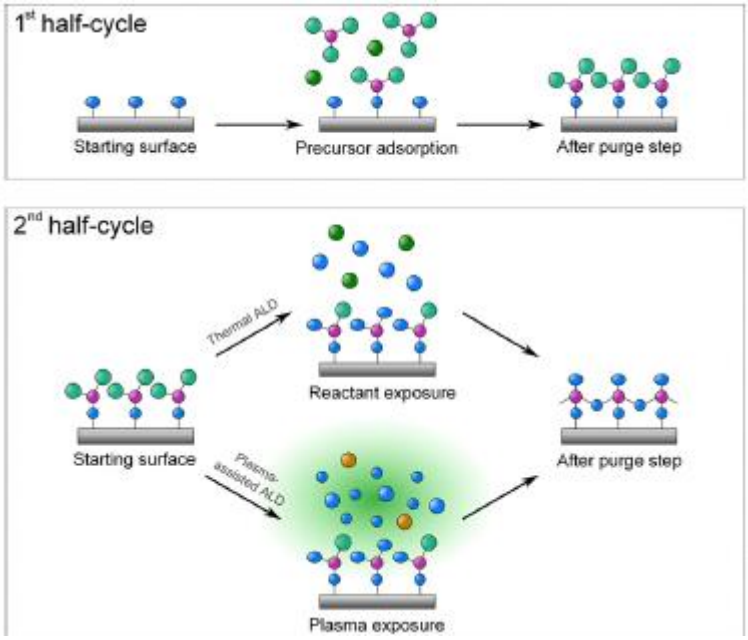

Figure 2-7. Schematic representation of thermal and plasma-assisted ALD processes [27].[7]

These processes exhibit a self-limiting behavior, in which the rate of deposition is determined by the rate of the reaction at the surface of the substrates rather than precursor flux. Since the reaction terminates when the available reactive sites are used up, the growth rate, and film thickness, is dependent on the number of cycles rather than exposure times [15]. ALD can produce films of uniform thickness and composition on complex geometries at low temperatures (150-350°C) with precise control over the

[7] Reprinted with permission from Journal of Vacuum Science and Technology A, Volume 29, Issue 5, H. B. Profijt, S. E. Potts, M. C. M. van de Sanden, et al., Plasma Assisted Atomic Layer Deposition: Basics, Opportunities, and Challenges, Copyright 2011, American Vacuum Society.

process [27, 28]. However, PEALD encounters issues with industrial scale-up due to the complexity of the equipment.

The high reactivity of the plasma reactants allows for a wider range of materials applications, including the deposition of metal oxides and nitrides [27]. Zirconium nitride films have been produced using PEALD with bis(cyclopentadienyl) zirconium(IV) amide, $ZrCp_2(NMe_2)_2$, and tetrakis(diethylamino)zirconium (TDEAZ), $Zr(NEt_2)_4$, precursors and N_2, H_2/N_2, or NH_3 plasma. In the case of the former, films thicker than 1.25 nm were unable to be grown due to difficulties with the volatility of the precursor [29]. The use of TDEAZ with N_2 plasma has been shown to produce films up to approximately 23 nm thick after 150 cycles with a linear growth rate of 0.15 nm/cycle at 300 °C [30]. The composition of the film was determined to consist of zirconium and nitrogen at approximately a 2.5 to 1 stoichiometric ratio with about 6 percent by atom carbon content.

2.2 Metal-organic CVD Precursors

A common method for producing ZrN via CVD utilizes a zirconium tetrachloride precursor with a N_2/H_2 mixture in the reaction described in Eq. 13 [31]. The deposition reaction has been shown to produce ZrN coatings at a reaction temperature of 1170 °C. The high temperature requirement makes this method incompatible with thermally sensitive substrates [32]. However, the major issue with this process on uranium substrates is the corrosion of uranium metal. As shown in Eq. 14, the metal halide reacts with uranium metal to produce uranium chloride starting at temperatures lower than the deposition reaction temperature [33].

$$ZrCl_4 + {}^{1}/_{2}\,N_2 + 2H_2 \xrightarrow{>1000\ ^\circ C} ZrN + 4HCl \qquad 13)$$

$$U + {}^{3}/_{X}\,MCl_X \xrightarrow{450\ ^\circ C} UCl_3 + {}^{3}/_{X}\,M \qquad 14)$$

Metal-organic (MO) compounds consist of an atom of a metal bound to one or more carbon atoms of a hydrocarbon group [20]. The MO complement the halides and

carbonyls precursors for the deposition of transition metals and their compounds. CVD occurs through thermal decomposition, or pyrolysis, of the precursor at the correct temperature to form the desired compound [34]. Due to the low binding energy of MO compounds, relatively low temperatures are required to break these weak bonds and initiate thermal decomposition of the precursor [19].

The alkyl class of MOCVD precursors, consisting of a combination of ethyl and methyl functional groups, are of particular interest to this work. These compounds are nonpolar and volatile [20]. Metalorganic compounds composed of methyl groups start to decompose at 200 °C, and those with ethyl groups start to decompose at 110 °C. Metalorganic precursors that have been demonstrated to create ZrN films include tetrakis(dimethylamino)zirconium (TDMAZ; $Zr[N(CH_3)_2]_4$), tetrakis(diethylamino)zirconium (TDEAZ; $Zr[N(C_2H_5)_2]_4$), and tetrakis(ethylmethylamino)zirconium (TEMAZ; $Zr[N(C_2H_5)(CH_3)]_4$) [32, 35-37]. The chemical structures of these compounds are shown in Figure 2-8. TDMAZ was chosen for use in this project by Arrieta because it was believed to involve the lowest process temperature of the selection [17]. TDMAZ exhibited the lowest boiling point, 80 °C compared to 81 °C for TEMAZ and 128 °C for TDEAZ [38]. Studies of the gas phase chemistry of TDMAZ have recommended gas phase temperatures below 300 °C for CVD processes [35] and experimental studies have shown effective deposition from 300-400 °C [36, 37].

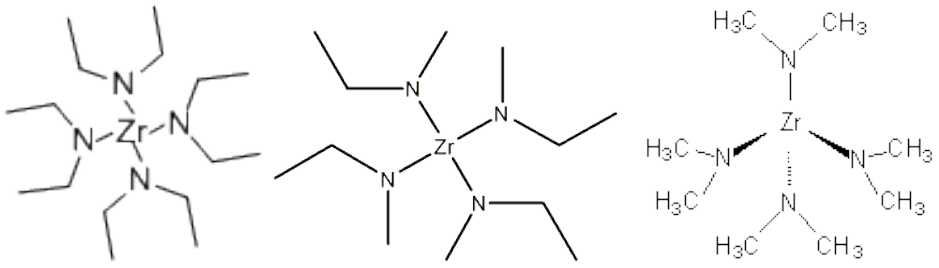

Figure 2-8. Chemical structures for MO-CVD precursors TDEAZ (left), TEMAZ (center) and TDMAZ (right) [38].

TDMAZ is a yellow crystalline solid at room temperature with a melting point of 58 °C and vapor pressure of about 1 torr at 120°C [35]. After extended heating near the melting point, the MO precursor may begin to decompose and polymerize into non-volatile species [17]. For this reason, the solid precursor must be sublimated using temperatures below the melting point (~50 °C) [35]. Once in the gas phase, the vapor species should be heated (~70°C) to avoid precursor condensation in the transport pipes. Studies of the gas phase behavior of TDMAZ has shown that the chemical precursor effectively decomposes in an argon atmosphere around 300 °C. However, above 300 °C significant dissociation of the dimethylamido groups from zirconium could lead to particle generation or a starved-reaction regime at the substrate surface. Therefore, the gas phase temperature should be maintained below 300 °C for CVD processes. The compound is also oxygen and moisture sensitive, so precursor handling techniques and preparation environments must be heavily considered.

Research has been performed using TDEAZ in CVD with substrate temperatures ranging from 200-400 °C [32]. The films produced were characterized as a zirconium nitride consistent to a stoichiometry of Zr_3N_4. Less than 1 atom percent oxygen and carbon contamination was observed in the films. Hydrogen contamination was observed as low as 10 atom percent and decreased with increasing substrate temperature.

Plasma-assissted CVD has also been used with metalorganic precursors. The films were produced using TEMAZ and TDEAZ at a substrate temperature between 200 and 500 °C resulting in a zirconium carbonitride film [36]. The deposition rate and coating structure was found to be dependent on the substrate temperature. At substrate temperatures below 300 °C, the coatings exhibited a columnar structure, while fine-grained polycrystalline structures were observed in coatings produced a substrate temperatures up to 400 °C. The carbon impurities present was also found to decrease with higher temperatures.

2.3 FB-CVD System Design

Design work of a lab-scale FB-CVD system was performed by Arrieta [17]. Spouted bed reactors with quartz and pyrex precursor bubblers were designed and tested. Effective fluidization was observed with particles of varying shapes and sizes, but a large percentage of material was lost due to over-fluidization of small particles through the exhaust and under-fluidization of large particles falling through the inlet. Issues with the glass fracturing also arose during assembly/disassembly and transport. The bubbler exhibited difficulties with vaporizing the precursor, as most of the precursor remained in the bubbler at the end of the experiment, and substantial coatings were not observed.

An inverted FB-CVD reactor was designed to overcome material loss due to fluidization issues [17]. In this reactor design, shown in Figure 2-9, the fluidization and carrier gas flow are transported to the bottom of the glass tube and then reverse flow to interact with the particle bed. The precursor bubbler, also pictured below, was designed using a Swagelok stainless steel sample cylinder. The stainless steel design was corrosion resistant to TDMAZ and easy to seal, assemble, and clean. The bubbler consisted of a concentric stainless steel inlet tube to allow argon flow gas to enter at the bottom of the sample cylinder and transport the precursor vapor out the top of the cylinder to the line on the right. A schematic of the experimental setup and components used is shown in Figure 2-10.

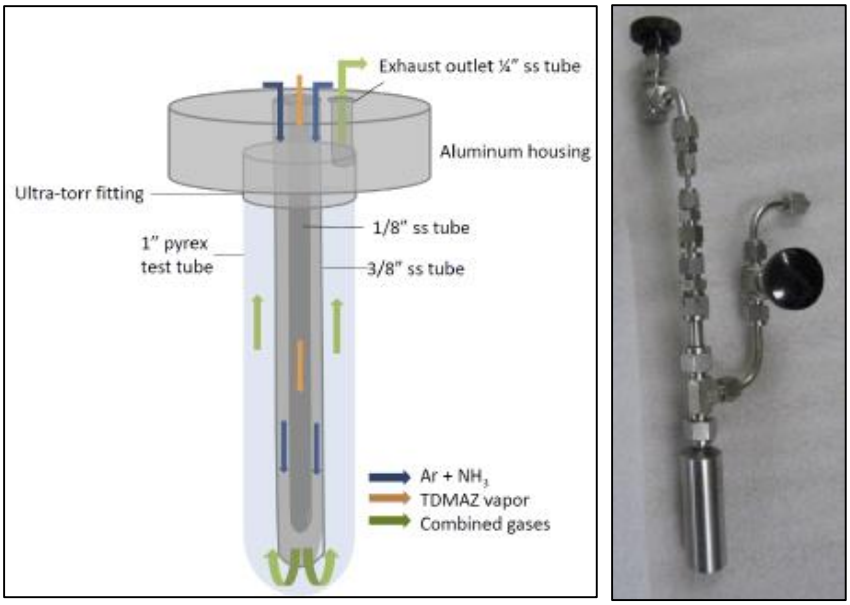

Figure 2-9. Inverted bed reaction vessel (left) and precursor bubbler (right) [17].

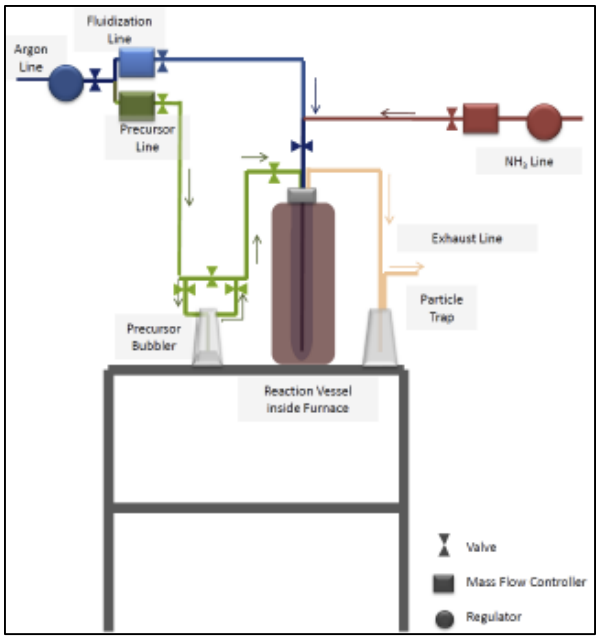

Figure 2-10. Inverted FB-CVD experiment schematic [17].

The experiments performed with the inverted reactor design were performed using zirconia-silica microspheres as a substrate with a low flow rate of 95 ± 2 mL/min [17].

The precursor sample cylinder was heated using heating tape to 51 ± 2 °C to avoid precursor decomposition over a long period of time and placed near the reaction vessel to minimize transport distance. Using this system, fluidization of the particulate substrate was successfully achieved, and the precursor vapor was successfully transported through the reaction vessel to the fluidized particles. The use of ammonia has been shown to reduce the amount of carbon deposited in the coating through a series of reactions with a metalorganic precursor for a gentle CVD system [39]. A gentle flow of ammonia was tested in the FB-CVD system. However, particle coatings were only visually observed on the particles when ammonia was not used, indicating that ammonia with the precursor gas flow in the reactor inhibited coating deposition in this FB-CVD system [17]. The thickest coatings, based on visual coatings and WDS analysis for nitrogen on the sphere surface, were observed at 280 °C. Therefore, the described temperature and flow rate conditions were used in the tests discussed in Chapter 3.

3. EXPERIMENTAL DESIGN AND PROCEDURES

This chapter describes the experimental equipment and procedures used to carry out the experiments. The experiments, reported in Chapter 4, were completed in three phases. The following sections describe the equipment common to all experiments (Section 3.1) as well as the specific descriptions of the three particular systems (Section 3.2 to 3.4). The first system in Section 3.2 was based on the previous system noted in Section 2.3 created by Arrieta [17]. Section 3.3 describes a transitional phase wherein system improvements were made between each test to strive for better coating outcomes. The final apparatus configuration in Section 3.4 was used with minimal modifications to perform a small parametric study. The final section (Section 3.5) describes specific details related to the characterization methods used to evaluate the efficacy of the powder coating process.

3.1 Description of Common Equipment Laboratory Setup for All Experiments

The experiments were conducted inside an open air chemical fume hood. The reaction vessel and bubbler were separately loaded and unloaded inside of an inert argon atmosphere glovebox to minimize exposure to oxygen and moisture. The atmosphere within the glovebox contained an oxygen content typically ranged from 5 to 30 ppm and a moisture content typically below 10 ppm. The system components were connected using stainless steel Swagelok and Hylok fittings with SS Swagelok/Hylok ball and needle valves placed accordingly to isolate and seal components when transporting between the chemical hood and glovebox.

The following list comprises various elements that were common to all experiments in this study.

- TDMAZ crystals (electronic grade, $\geq$ 99.99%) were purchased from either STREM Chemicals Incorporated (Newburyport, MA) or Sigma-Aldrich (St. Louis, MO) and stored in a refrigerator at 2 to 8 °C in a container sealed under Ar,

- Ultra High Purity (UHP) argon gas (99.999%) from Brazos Valley Welding Supply (Bryan, TX) with pressure regulators (VWR 55850-474) was used for precursor carrier and fluidization gas. The system was equipped with two source tanks with individual regulators and purge valves to allow for tank replacement without disrupting gas flow during the experiments.
- Oxygen (Agilent Technologies BOT-4, 750cc) and moisture traps (Agilent Technologies BMT-4, 750cc) were attached to the gas lines prior to entering the system to remove any excess oxygen and water. The two traps were later replaced with a single oxygen/moisture trap (Supelco Model 503088, 750cc).
- Type K thermocouples, 45.7 cm (18 in.) inside the reaction vessel (Omega KQSS-116U-18) and 30.5 cm (12 in.) elsewhere (Omega KQXL-116G-12), connected to a temperature data logger (Omega OM-CP-OCTTEMP2000-CERT) were used to monitor and record the temperatures in the various components continuously throughout an experiment via Omega 2.07 software.
- The solid precursor was contained in a Swagelok stainless steel sample cylinder (SS-4CS-TW-25) heated to 51 ± 2 °C using heating tape (Omegalux Model DHT051020LD) and insulation. The temperature inside the sample cylinder was monitored by placing the thermocouple in between the cylinder and heater tape.
- The stainless steel tubes prior to and connecting the bubbler and reaction vessel were wrapped with silicon heater tape (Omega Model SRT051-120LSE) to preheat the argon gas and prevent precursor condensation during transport. The thermocouple to monitor the temperature in the tubes was placed in between the tube and heater tape entering the bubbler.
- The reaction vessel consisted of an aluminum housing and 2.54 cm (1 in.) outer diameter Pyrex round-bottom tube produced by the TAMU chemistry glass shop[8] to contain the fluidized particulate bed during the reaction.

[8] A special thanks to Bill Merka at the TAMU Department of Chemistry for his ideas and work in designing the glassware.

- The aluminum and glass components of the reaction vessel are connected by a Swagelok Ultra-Torr stainless steel vacuum fitting with high temperature silicon O-rings (SS-16-UT-A-20).
- The particle bed was heated to 280 ± 10 °C by placing the glass tube inside a moveable aluminum annulus heated externally with high temperature fiberglass heater tape (Omega Model DHT051040LD) and monitored by thermocouples inside and outside of the glass tube.
- The heating tapes are controlled by variable transformers (Staco Energy Model 3PN1210B).
- The reaction vessel exhausted to a particle trap consisting of a 500 mL filtering flask with a rubber stopper connected by a 0.64 cm (0.25 in.) PTFE hose to contain any material that was over-fluidized and blown out of the reaction vessel.
- A rotary vane vacuum pump was attached to the filtering flask to facilitate particle fluidization in the reaction vessel.

The following substrates were used in the various tests:

- ZrO_2-SiO_2 microspheres (75 to 250 μm),
- U-7Mo microspheres (45 to 125 μm) obtained from INL (Idaho Fall, ID) stored in an air-filled radioactive material cabinet,
- U-8Mo microspheres (60 to 150 μm) containing depleted ^{235}U also obtained from INL stored in an argon atmosphere glovebox.

3.2 Description of System and Procedures for Preliminary Experiment Series

The first experiments performed for this work sought to reproduce the outcomes from the previous work by Arrieta [17]. Basic elements of the system description are discussed in Section 2.3. A schematic of the experimental setup and components is shown in Figure 3-1. This system utilizes two mass flow controllers the control the high argon flow rate (OMEGA model FMA5524) and low argon flow rate (Omega model FMA5508). Electronic grade ammonia gas (99.9992%) from Matheson (Houston, TX) is controlled by separate mass flow controller (Omega model FMA5508ST). The gas flow lines enter the

chemical hood via 0.64 cm (0.25 in.) copper tubes and connect to the bubbler and reaction vessel through 0.64 cm (0.25 in.) PTFE tubing. The experimental setup inside of the chemical hood is pictured in Figure 3-2.

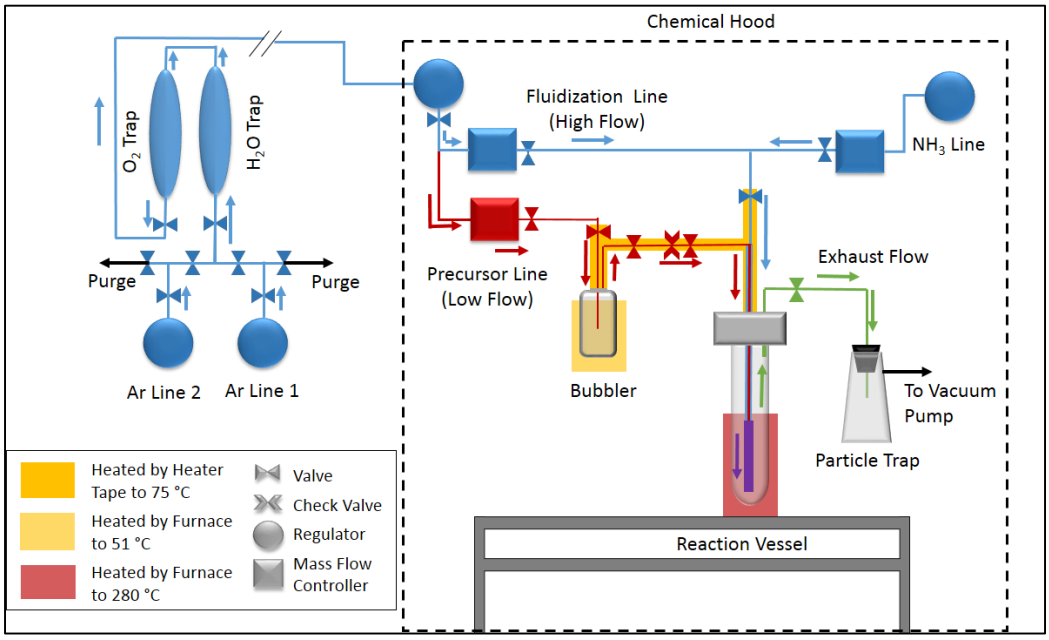

Figure 3-1. Schematic of components and flow patterns used for the preliminary experiment series.

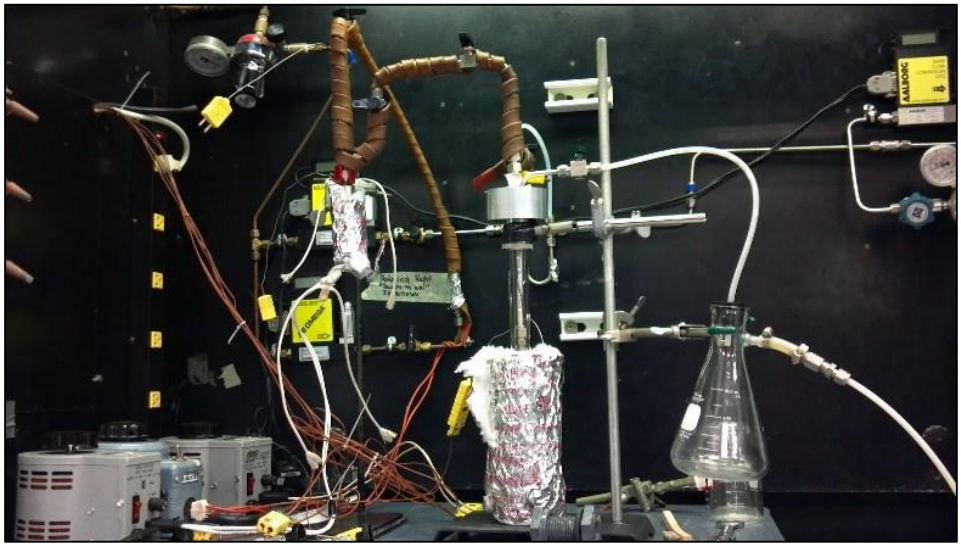

Figure 3-2. Experiment assembly used for the preliminary experiment series.

The precursor carrier argon gas entered through the top of the bubbler, shown in Figure 3-3, through a 0.32 cm (0.125 in.) stainless steel tube. The Ar flow interacted with the TDMAZ vapor at the bottom of the sample cylinder. The mixed gas flow then exited the top of the sample cylinder and was transported to the reaction vessel through the right branch of the tee.

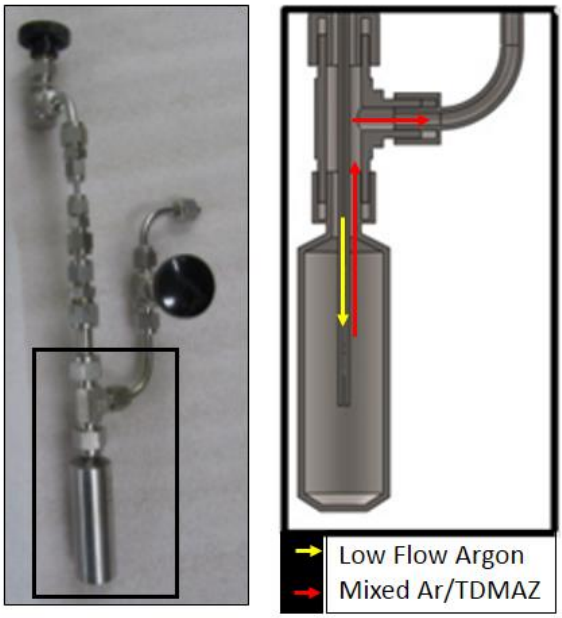

Figure 3-3. Image of the precursor bubbler (left) and schematic of gas flow paths (right) used in the preliminary experiment series.

The precursor flow then entered the top of the reaction vessel, pictured in Figure 3-4, and was transported through the aluminum housing in a 0.32 cm (0.125 in.) stainless steel tube inside of a 0.95 cm (0.375 in.) tube containing the fluidization flow argon. The two streams mixed near the bottom of the reaction vessel and exited at the bottom of the reaction vessel through a 0.32 cm (0.125 in.) tube. The flow then interacted with the particle bed at the bottom of the glass tube to fluidize and coat the particles. The reaction byproducts and excess precursor were then exhausted through the top of the aluminum housing to the particle trap.

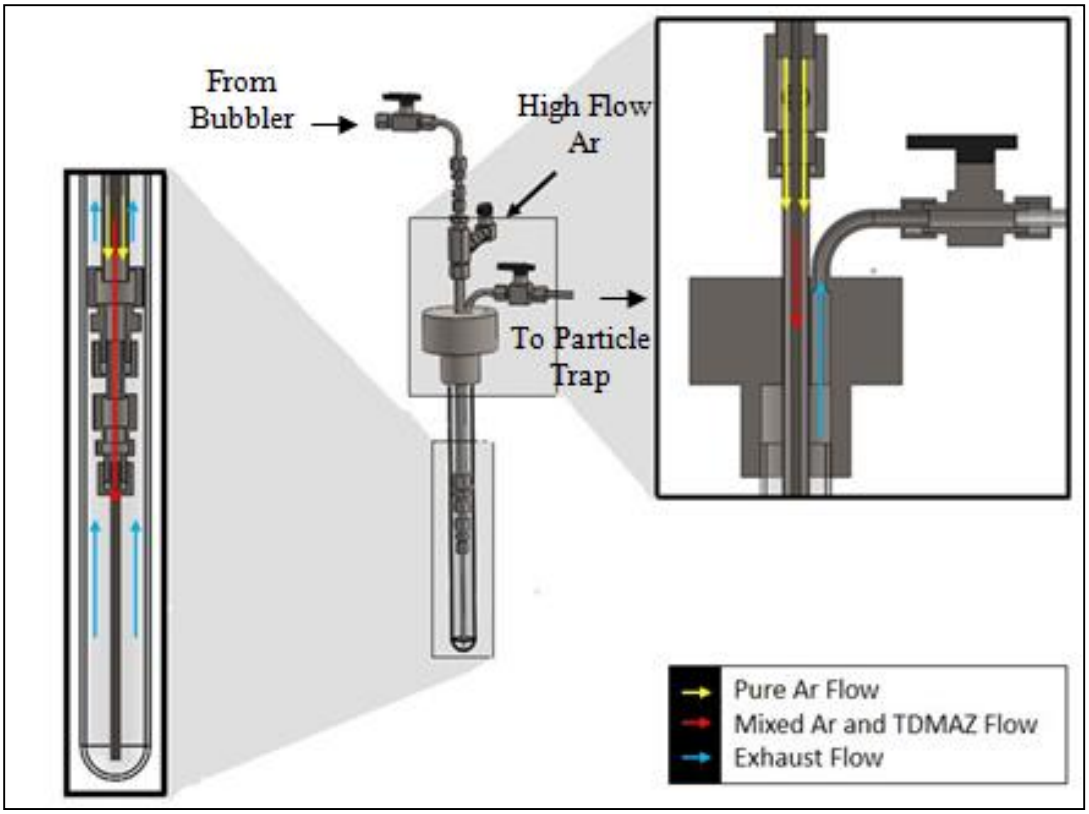

Figure 3-4. Schematic of gas flow paths through the reaction vessel used in the preliminary experiment series.

The varied conditions for experiments in this series, Experiments 1-6, are shown in Table 3-1. The minimum fluidization flow rate was determined by incrementally increasing the flow rate until complete fluidization of the particle bed was achieved. Complete fluidization was assumed based on visual observation of the behavior of the particle bed. For experiments 2 and 3, ammonia was introduced into the CVD system in order to remove carbon impurities that may have deposited on the substrate due to incomplete decomposition of the precursor [17]. However, Arrieta found that the use of the precursor and ammonia simultaneously interfered with coating deposition. Therefore, the use of ammonia was implemented by alternating the gas flow with the precursor in order to prevent the two from reacting. This was performed by isolating the bubbler and opening the ammonia flow every 8 hours for 30 minutes. The reaction vessel was purged for 10 minutes each time the gas flow was changed.

Table 3-1. Preliminary test experiments.

Condition	**EXP 1**	**EXP 2**	**EXP 3**	**EXP 4**	**EXP 5**	**EXP 6**
Substrate	ZrO_2-SiO_2	ZrO_2-SiO_2	U-7Mo	U-7Mo	U-7Mo	U-7Mo
Ammonia Flow	None	Alternating	Alternating	None	None	None
Fluidization Flow Rate (L/min)	0.9	0.9	1.5	2.7	1.6	0.9-3.1
Run Time (h)	30	48	90	23	94	96
Amount of Precursor (g)	0.6	1.85	1.96	2.26	4.5	4.15

To start each experiment, the bubbler and reaction vessel were loaded into the glovebox using the U-7Mo and TDMAZ source materials described in Section 3.1. The TDMAZ and U-7Mo were loaded into the bubbler and reaction vessel, respectively, in the glovebox. Once filled, the reaction vessel and bubbler were sealed and removed from the glovebox. Immediately following removal, the reaction vessel was connected to the fluidization gas flow line and particle trap, and placed under vacuum. Meanwhile, the bubbler was connected to the precursor carrier gas flow line and the vessel while remaining isolated. The fluidization flow argon was opened and the flow rate was set by increasing the value until complete fluidization of the particle bed was visually observed. The vessel was placed inside the furnace, heated to 280 ± 5 ºC, and purged for 2 hours with UHP Ar. The bubbler and connecting tubes were heated to 51 ± 2 ºC, 75 ± 5 ºC, respectively. Fluctuations in the temperature were regularly observed due changes in the ambient temperature caused by unrelated activities. The effect of the ambient temperature was greater for the uninsulated regions of the connecting tubes. Response to these fluctuations required manual interference by adjusting the power applied from the variable transformers, introducing a source of error in the applied temperature during periods in which the experiment was not monitored.

Once the desired temperatures were reached, the precursor carrier flow rate was set at 95 mL/min. To start the CVD phase, the bubbler was opened starting with the valve immediately following the precursor carrier gas flow controller and continuing in the

direction of flow. The temperatures were continuously monitored and recorded throughout the experiment. The flow rates were monitored periodically.

At the end of the experiment, the bubbler was isolated and the reaction vessel remained open to Ar flow and vacuum. The power was turned off to allow the reaction vessel to cool before removing the sealed vessel from the system. Once cooled, the fluidization flow was turned off. The vessel was sealed under vacuum and transferred to the glovebox chamber. The microspheres were placed in a vial to store inside the glovebox until analysis, and the vessel was removed for cleaning.

3.3 System Improvements Created Over Multiple Development Tests

After the preliminary tests described in Section 4.1 using the setup in Section 3.2, a series of system modifications were developed to improve the performance of the FB-CVD coating process. Particular improvements were sought for precursor transport and oxygen control within the system.

3.3.1 Component Configurations

The bubbler presented in Section 3.1 and shown in Figure 3-3 was modified to decrease oxygen contamination in the process. The new configuration of the modified bubbler is shown in Figure 3-5. The number of joints on the entering line was reduced by using more direct mechanical connections. The series of connections between the bubbler and reaction vessel was modified to reduce the gas travel distance between the bubbler and vessel isolation valves.

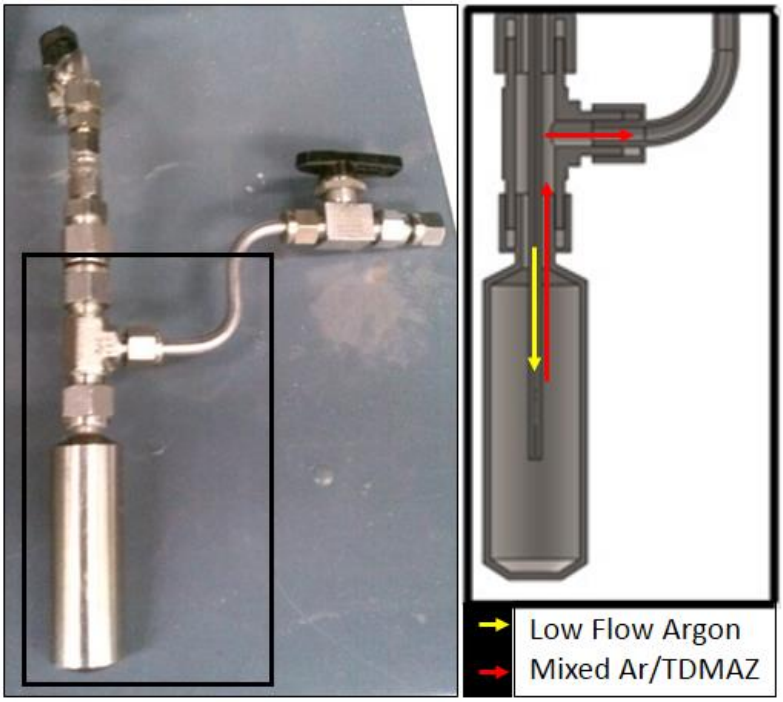

Figure 3-5. Precursor bubbler configuration (left) and flow path schematic (right) used for the series of system modification experiments.

The reaction vessel and process tubing were tested for leaks using mass spectrometry to detect a helium source introduced externally around the mechanical connections. Significant leaks were discovered around cracks in the sealants surrounding the tubes as they enter the reaction vessel through the aluminum block. In order to create a more durable seal, the aluminum block was designed using NPT vacuum fittings, as shown in Figure 3-6. The diameter of the glass tube limited the space for the fittings. This was overcome by placing the exhaust line at a location and angle such that the inlet tube can run through the block to the bottom of the reaction vessel. The exhaust line was also adapted with a tee and O-ring vacuum fitting to allow the thermocouple to enter the vessel through the exhaust fitting. The modified reaction vessel was tested using the same mass spectrometry system. The oxygen leak was still present although significantly reduced. The system was also observed to hold a higher vacuum, which was predicted to aid in precursor transport.

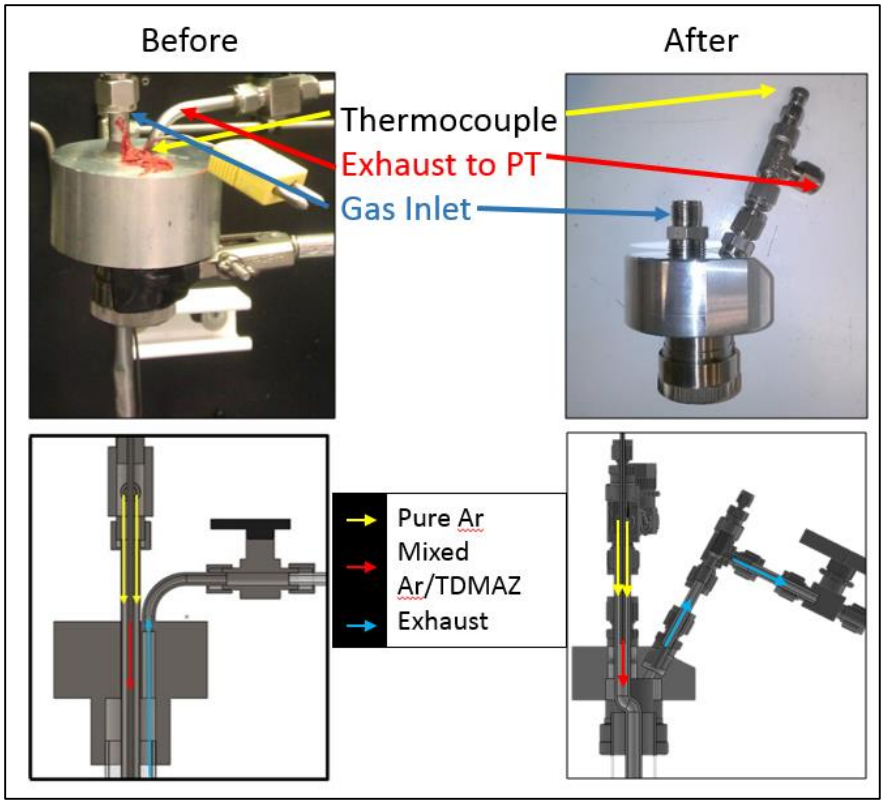

Figure 3-6. Images and schematic of the reaction vessel inlet and outlet before (left) and after (right) modification.

Due to the modifications of the system, a series of experiments was performed to test the behavior of the process. Additional modifications were required to the internal tubing of the reaction vessel between each experiment in response to the development of flow restrictions, discussed in more detail in Section 4.2. The fluidization flow rates and total operation time for each experiment is shown in Table 3-2. The fluidization flow rates were set by incrementally increasing the flow rate until complete fluidization of the particle bed was visually observed.

Table 3-2. Conditions for the series of experiments to test system modifications.

Condition	EXP 7	EXP 8	EXP 9	EXP 10	EXP 11	EXP 12
Fluidization Flow Rate (L/min)	1.2	0.75	1.0	1.25	1.5	1.0
Run Time (hours)	48	1	24	24	96	96

This system utilized two mass flow controllers the control the precursor carrier flow rate (Omega model FMA5508) and fluidization flow rate (Sierra SmartTrak C50L-AL-DD-2-PV2-V1-F5). The latter replaced the previous mass flow controller for this series of experiments to enable easier and more precise control over the fluidization flow rate. Use of the Sierra mass flow controller also enabled remote control and recording of the flow rate via computer. A schematic of the system components and flow directions is shown in Figure 3-7 and the system assembly is shown in Figure 3-8.

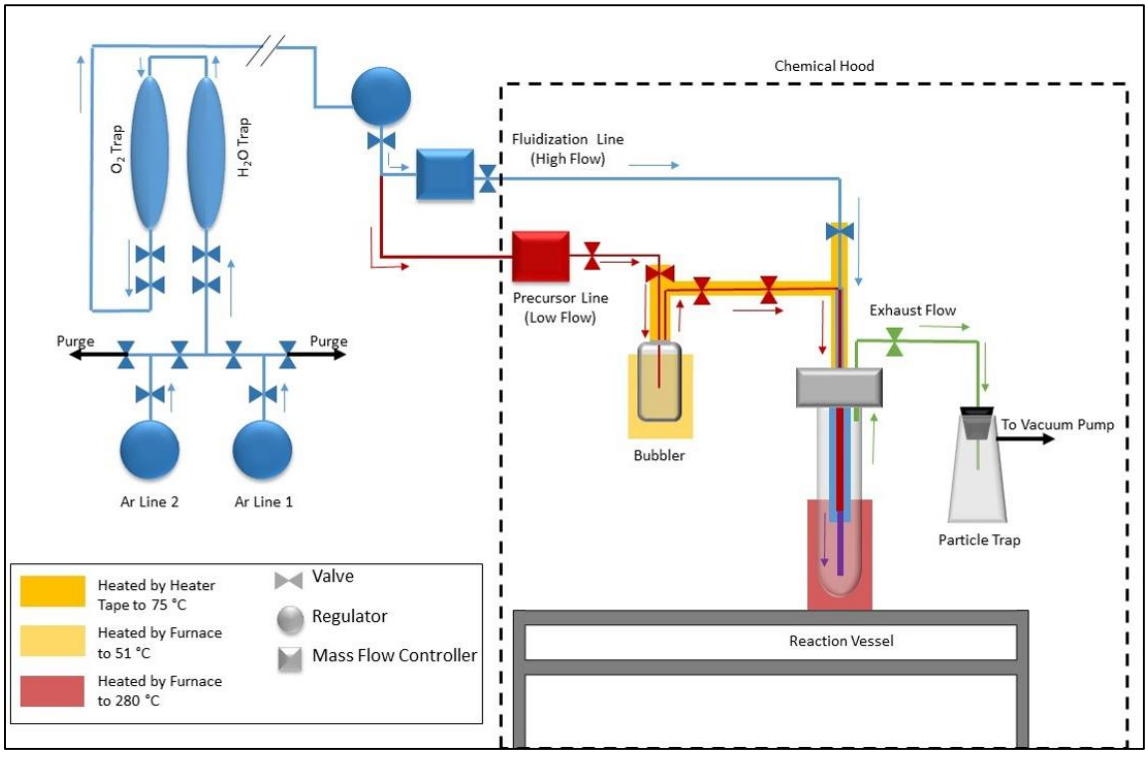

Figure 3-7. Schematic of experiment setup and gas flow patterns used for series of experiments to test system modifications.

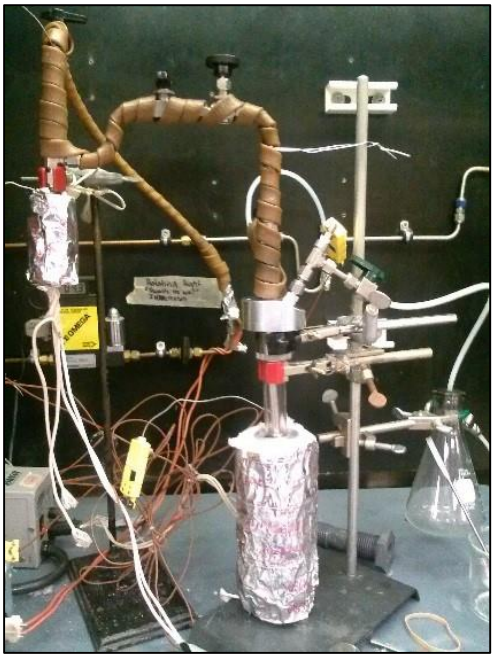

Figure 3-8. Image of the component assembly used to test system modifications.

3.3.2 Procedures

Due to the improved seal on the reaction vessel, the externally applied vacuum (e.g., as the sealed vessel was passed into the glovebox through a vacuum airlock) actually caused a new failure mode as the process vessel was pushed out of its fitting due to the pressure differential from internal gas pressure. This caused the glass to break in repeated tests inside the glovebox airlock. Following these events, the reaction vessel was loaded in the chemical hood, outside of the glovebox, and purged with UHP Ar for an additional 2 hours before heating. Purging was accomplished by first opening the reaction to the particle trap to place under vacuum, then opening the fluidization flow line to the vessel. After 2 hours, the vessel was placed inside the furnace and heated to 280 ± 5 ºC under UHP Ar flow for another 2 hours. While the vessel was purging, the bubbler was loaded and connected to the system as in previous tests. The bubbler remained sealed until the desired temperature in the various components was reached.

To start the CVD process, the precursor carrier flow rate was set at 95 mL/min and the bubbler was opened starting with the valve immediately following the precursor carrier gas flow controller and proceeding in the direction of flow. The temperatures were continuously monitored and recorded throughout the experiment. The flow rates were monitored periodically.

At the end of the experiment, the bubbler was isolated and the reaction vessel remained open to Ar flow and vacuum. The heaters were turned off, and the reaction vessel remained under Ar flow for 2 days. The vessel was then opened in the chemical hood, where the microspheres were placed in a vial. The microspheres were then transferred to the glovebox to store until analysis.

3.4 Final System Configuration and Parametric Study of Process Variables

The final system configuration was established with flow patterns according to the schematic shown Figure 3-9. The oxygen and moisture traps were replaced with a single oxygen/moisture trap (Supelpure-O, 750cc). Two mass flow controllers were used to control the precursor carrier (Sierra SmartTrak C50L-AL-DD-2-PV2-V1-F3) and fluidization flow rates (Sierra SmartTrak C50L-AL-DD-2-PV2-V1-F5) as shown in Figure 3-10a. The gas flow lines enter the chemical hood via 0.64 cm (0.25 in.) copper tubes and connect to the bubbler, pictures in Figure 3-10b, and reaction vessel, pictured in Figure 3-10c through 0.64 cm (0.25 in.) coiled copper tubing, pictured in Figure 3-10d. The concentric 0.32 cm (0.125 in.) and 0.95 (0.375 in.) SS tubes entering the reaction vessel were replaced with a single 0.64 cm (0.25 in.) SS tube to resolve clogging issues caused by heated reducing joints. As a result, the fluidization and precursor flow mix prior to entering the reaction vessel rather than inside. The reaction vessel also utilized a glass tube with the bottom 10.2 cm (4 in.) tapered to a shallow rounded bottom as shown in Figure 3-11. Flow rates in the system were monitored by continuously recording the flow controller voltage with National Instruments voltage DAQ (NI USB-6002) in Labview Signal Express.

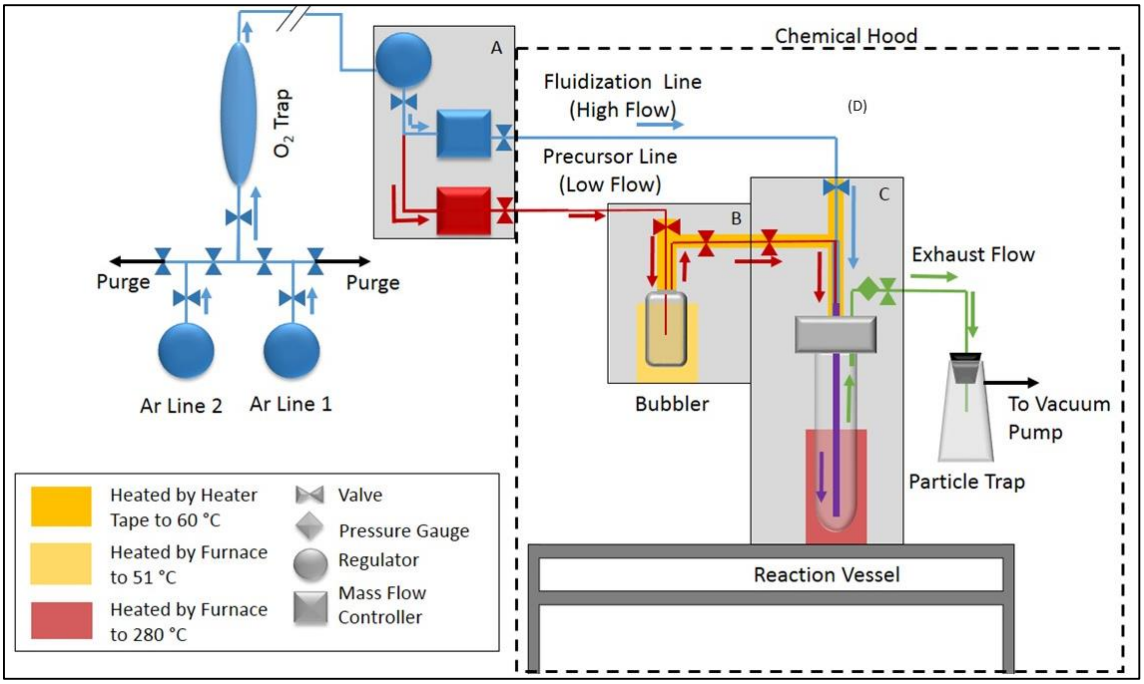

Figure 3-9. Schematic of experiment setup and gas flow patterns used for series of parametric studies.

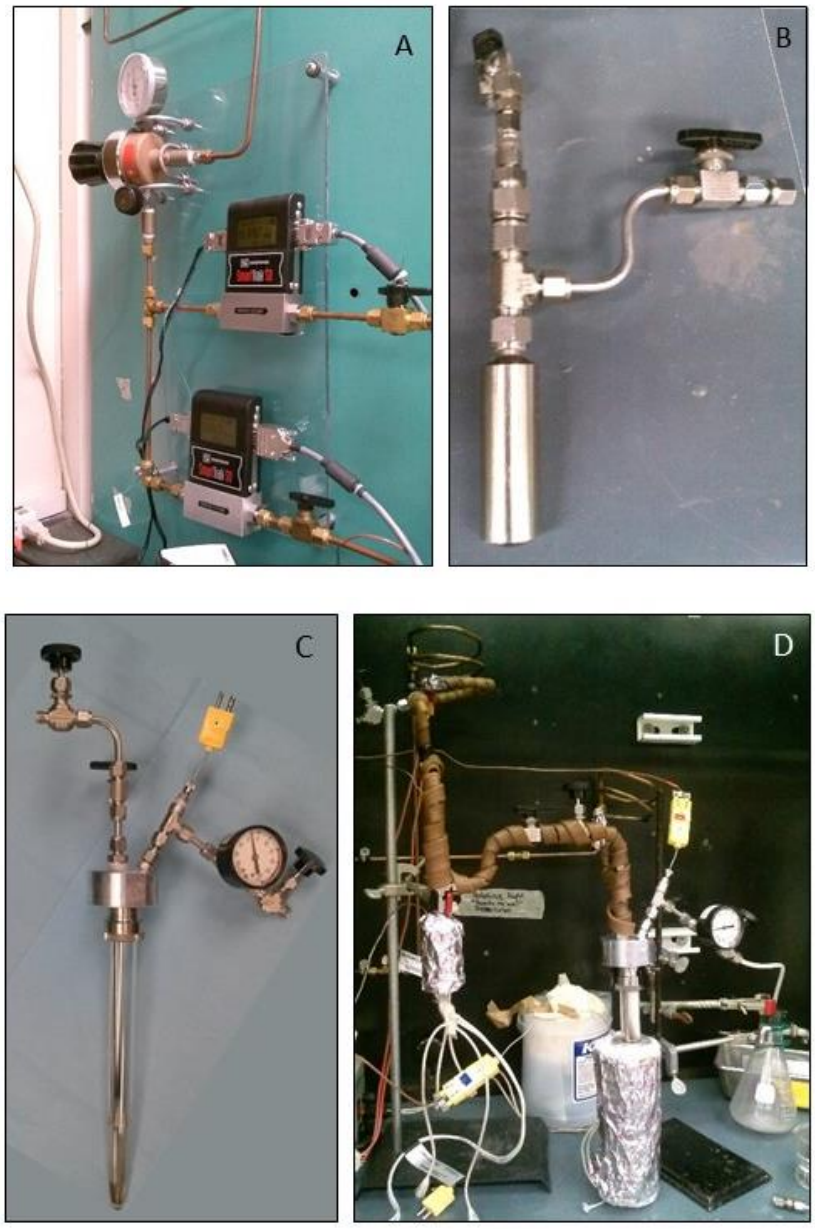

Figure 3-10. Images of system components used for the parametric studies: a) Sierra mass flow controllers, b) precursor bubbler, c) reaction vessel, and d) component assembly in the chemical hood.

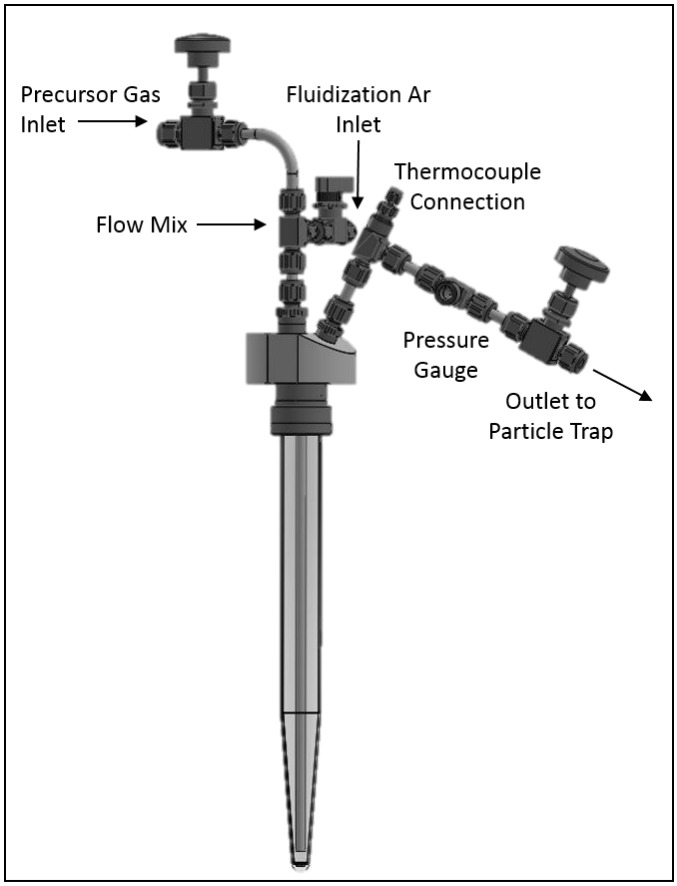

Figure 3-11. Schematic of tapered reaction vessel design.

3.4.1 Baseline Experiment Conditions and Procedure

The following list provides a step-by-step procedure for the startup and disassembly of the baseline experiments. Unless otherwise noted in Sections 3.4.2 and 3.4.3, the methods described were used for each experiment and the sets of parametric studies.

1) The reaction vessel was loaded with U-8Mo (10 g) inside the glovebox.
2) Once filled, the vessel was sealed and removed from the glovebox. The failure mode inside the airlock discussed in Section 3.3.2 was addressed by placing rubber clamps at the base of the glass tube. These clamps were attached to aluminum wires connected at the top of the aluminum block to hold the glass tube in place.

3) Inside the chemical hood, the annulus furnace was placed around the glass tube. The vessel was held in place by two clamps attached to a test tube stand. One clamp was placed at the vacuum fitting allowing the aluminum block to rest on top of the clamp. The other clamp was placed around an unheated area the glass tube such that the furnace could be raised to view the bottom of the vessel.
4) Immediately following removal from the glovebox and transfer the chemical hood, the vessel was connected to the fluidization flow line and particle trap and placed under vacuum.
5) The fluidization Ar flow was then slowly opened at a flow rate of 0.3 L/min and ramped up until fluidization was observed at 0.5 L/min.
6) Power was applied to the vessel furnace to begin heating to 280 ± 10 ºC. During heat up, the system continued purging with UHP Ar for 1-2 hours.
7) During the reaction vessel purge, the bubbler was loaded with TDMAZ inside the glovebox. The sealed bottle of TDMAZ (5 g) was removed from the refrigerator and placed inside the glovebox with the bubbler.
8) Once filled, the bubbler was sealed and removed from the glovebox. The bubbler was connected to the precursor carrier gas flow line and the reaction vessel, but remained isolated.
9) The bubbler and connecting tubes were wrapped with heater tape and heated to 51 ± 2ºC, 65 ± 5ºC, respectively.
10) The precursor carrier flow line was purged using a needle valve prior to bubbler inlet with 1200 mL/min for approximately 3 minutes. After purging, the precursor carrier gas flow was set to zero.
11) The CVD process was started by opening the bubbler, starting with the valve immediately following the flow controller and continuing in the direction of flow. The needle valve in between the bubbler and vessel was opened last to slowly allow gas inside the tubes to be evacuated. The precursor carrier flow rate was then incrementally ramped up to 100 mL/min. These steps are performed in

this order to avoid over-fluidization of the particles due to pressure buildup in the bubbler.

12) The CVD process proceeded over 48 hours.
13) The Ar source gas was replenished periodically throughout the experiment. Empty source gas tanks were replaced using the two-tank system described in Section 3.1 to avoid disrupting the gas flow during the experiment.
14) At the end of the experiment, the bubbler was isolated, and the reaction vessel remained open to fluidization flow and vacuum. The heaters were turned off.
15) If an Ar/H_2 post-treatment of the particles was performed, the gas line was switched to Ar/H_2 for about 1.5 hours, then purged with UHP Ar for a minimum of 10 minutes.
16) Once cooled, the fluidization gas flow was turned off. The vessel was sealed under vacuum and transferred to the glovebox chamber along with the bubbler.
17) The airlock was purged with UHP Ar at approximately 20 to 27 kPa (150 to 200 torr) vacuum pressure for 30 minutes to avoid pulling full vacuum on the vessel glass.
18) The remaining reaction vessel and bubbler contents were weighed inside the glovebox. The microspheres were placed in a vial to store inside the glovebox, and the vessel and bubbler were removed for cleaning.

3.4.2 Description of Experiments for Time-Varying Studies

A set of experiments was designed to determine the effects of deposition time on the particle coating thickness. For these experiments, the fluidization and precursor carrier flow rates were held constant at 0.5 L/min and 100 mL/min, respectively. The duration of each of the experiments was varied as described in Table 3-3. A run time of two days was used as a baseline comparison as discussed in Section 3.4.1. The duration of the CVD process was extended in the following experiments. The following experiment, labeled T8, was allowed to run for 8 days in attempt to produce a thicker coating and analyze the development of the coating structure. The TDMAZ loading in the precursor was doubled

to 10 g to address concerns of precursor depletion. Based on observations made by Arrieta, the precursor was suspected to have started decomposing after an extended period at elevated temperatures in the bubbler. In order to determine if this possible decomposition of the precursor affected the coating production, fresh precursor was reloaded in the bubbler after 4 days of deposition in experiment T6. Initially, 5 g of TDMAZ was loaded into the bubbler using the procedure described in Section 3.4.1. The following steps were used to clean the bubbler and refill the precursor. The reaction vessel remained unchanged during this process.

1) After 4 days, the bubbler was isolated from the system, and transferred to the glovebox to weigh the remaining precursor. The bubbler was removed from the glovebox to clean out the remaining precursor.
2) The inside of the tubing and connections were rinsed with water and ethanol and dried using pressurized air flow.
3) The precursor remaining in the sample cylinder was decomposed by slowly introducing drops of water to the sample cylinder until the vapor exhaust was no longer observed.
4) The sample cylinder was then rinsed with ethanol to remove the remaining residue.
5) The sample cylinder was wrapped with aluminum foil and placed in a furnace at about 100 °C for about 30 minutes to dry the cylinder and decompose any remaining precursor.
6) The bubbler was allowed to cool to room temperature and was transferred to the glovebox.
7) The bubbler was reloaded with 5 g of TDMAZ and reconnected to the CVD system using the same method used at the beginning of the experiment.
8) The CVD process was allowed to continue for another 2 days. This shorter period allowed the apparent precursor transport over different time intervals to be examined from the same experiment. The total run time for the CVD process was 6 days.

Table 3-3. Duration and precursor loadings used for the experiment in the time-varying study.

	Baseline	T6	T8
Run Time (days)	2	6	8
Initial Precursor Loading (g)	5	5	10
Total Precursor Loading (g)	5	10	10

3.4.3 Description of Experiments for Flow Rate-Varying Studies

A set of experiments was performed to show the effects of precursor carrier flow rates on transport of the precursor and corresponding coating thickness. The following set of tests was performed with the deposition time of 2 days to compare the results to those of the baseline experiment described in Section 3.4.1. The total flow rate of the gas stream interacting with the particles was held constant throughout the experiments to avoid disruptions to the fluidization of the bed. The precursor carrier gas flow rate was increased by 100 mL/min increments in each experiment with the goal of increasing the rate of transport of the precursor. The fluidization flow rate was adjusted accordingly to maintain a total of 600 mL/min combined flow rate. The individual flow rates for each experiment are described Table 3-4.

Table 3-4. Conditions for precursor flow rate study.

	Baseline	F200	F300
Fluidization Flow Rate (mL/min)	500	400	600
Precursor Carrier Flow Rate (mL/min)	100	200	300

3.5 Sample Preparation and Characterization

Samples from each experiment were collected and stored inside the glovebox. The samples were removed from the glovebox and prepared for analysis. The particles were ultrasonically washed in ethanol for 10 minutes and dried in an open air chemical hood using filter paper and a filtering flask. The samples were prepared according to the type of analysis discussed in the following sections. Analysis of the samples was performed at the Electron Microprobe Laboratory at the Texas A&M Department of Geology and Geophysics[9].

3.5.1 Electron Microprobe Equipment and Details

When particles were segregated for examination from coated and uncoated sources, approximately 0.5 g of the particles were mounted on small carbon tape stubs to analyze the sphere surfaces. Another subset from the powder source (also ~0.5g) was set in epoxy resin to analyze a polished cross section. The epoxy samples were polished by hand using 600-grit SiC paper with ethanol to reach near the midsection of the microspheres. This was verified using a Hirox optical microscope. The samples were then polished using a Buehler Mini-Met polisher with 800 grit and 1200 grit SiC paper. Final hand polishing was then performed using 3 µm oil-based diamond suspension on nylon paper, followed by 1 µm and 0.25 µm diamond suspension. Polished samples were ultrasonically cleaned with ethanol and dried with lens paper. Both sample types were carbon coated before placement in the Electron Probe Micro-Analyzer (EPMA, Cameca Model SX50).

Samples were qualitatively characterized by backscatter electron imaging (BSE), energy dispersive X-ray spectroscopy (EDS), wavelength dispersive X-ray spectroscopy (WDS), and X-ray distribution mapping with the EPMA equipped with a PGT energy dispersive system and a dedicated Sun workstation using a 15 kV electron beam. These methods allow the characterization of the surface of a sample up to a depth specific to the

[9] A special thanks to Dr. Ray Guillemette in his assistance with EPMA operations and expertise in interpreting the results.

type of analysis [40]. Specifically for EDS and WDS analyses, the characteristic X-rays are generated in the tear-drop shaped region up to a depth of about 1.5 μm

BSE imaging was performed to examine coating textures of the sphere surfaces and surface layers of the polished samples, and EDS analysis was performed on the surface of the particles to examine the composition of the surface layer of various particles. Both analyses used beam current of 3 nA. WDS was performed on the coated sphere surfaces with a 50 nA current to detect nitrogen, oxygen, and zirconium presence. Four additive scans were performed about wavelengths corresponding to the O Kα, N Kα, and Zr Lα characteristic X-rays.

Two contacting particles of similar size in the polished sample were selected in order to analyze a surface near the mid-plane of the sphere. The corresponding coatings were assumed to be representative of the true thickness. This selection also reduced the surface rounding effects of the polishing process. X-ray maps of the suspected elements present (U, Mo, Zr, N, and O) were collected at polished sphere edges using a beam current of 50 nA to determine the elements present in the surface layers. Lastly, WDS stage scans were performed on selected samples using a beam current of 20 nA. This analysis was performed by detecting the characteristic X-rays of the suspected elements at 1 μm increments progressing linearly across the boundary of a sphere.

3.5.2 X-Ray Diffraction Equipment and Details

Selected samples were analyzed by powder X-ray diffraction (XRD). Samples were prepared by placing the microspheres (~0.5 g) on a glass slide. A solution of acetone (5 mL) and DuCo cement (4 drops) was added to adhere the particles to the slide. The particles and glue were spread to cover a 1 cm^2 area. The analysis was performed by scanning the sample at 1 °/min from 10-80 °2Θ.

4. RESULTS

All experiments performed and major conditions completed for this project are listed in Table 4-1. Experiments which failed due to a system malfunction are noted below. Experiments that did not produce a coating on the reaction vessel were considered failures, and the particles were not analyzed. The relevant sections in which the results of each experiment are discussed are listed in the last column of the table.

Table 4-1. Summary of experiments.

Project Phase	Experiment Label	Fluidization Flow Rate (L/min)	Precursor Carrier Flow Rate (mL/min)	Deposition Time (hours)	Coating Produced (Y/N)	System Failure	Section
Preliminary Tests	E1	0.9	95	30	Y		4.1
	E2	0.9	95	48	N		4.1
	E3	1.5	95	90	N		4.1.2
	E4	2.7	95	23	Y		4.1
	E5	1.6	95	94	Y		4.1.3
	E6	0.9-3.1	95	96	n/a	X	4.1
System Modifications	E7	1.2	95	48	n/a	X	4.2
	E8	0.8	95	1	n/a	X	4.2
	E9	1.0	95	24	Y	X	4.2
	E10	1.3	95	24	n/a	X	4.2
	E11	1.5	95	96	Y	X	4.2.1
	E12	1.0	95	96	Y		4.2.2
Parametric Studies	B1	0.8	100	87	Y	X	n/a
	B2	0.5	100	96	Y	X	n/a
	B3	0.5	100	36	Y		4.3.2
	B4	0.5	100	96	Y		n/a
	B5	0.5	100	47	Y		4.3.2
	T6	0.5	100	153	Y		4.3.3
	T8	0.5	100	192	Y		4.3.3
	F200	0.4	200	45	Y		4.3.4
	F300	0.3	300	42	Y		4.3.4

4.1 Preliminary Experiment Series

Experiments E1 to E6 were performed to repeat results from the previous study by Arrieta [17] and to explore coating samples under a variety of parameters. Table 4-2 presents additional information detailing the experiment conditions. In the work by Arrieta, the use of ammonia, intended to reduce carbon contamination, produced a yellow powder observed in the outlet traps [17]. This suggested that the ammonia and TDMAZ reacted prior to exiting the reactor chamber. Therefore, experiments E2 and E3 were performed by introducing ammonia at a low flow rate in alternation with precursor flow. The results of experiment E3, discussed in Section 4.1.2, suggested that this presence of ammonia in the system interfered with the particle coating, and the use of ammonia was discontinued. In experiment E4, it was observed that most of the precursor had evaporated after 2 days but had not yet produced a coating. The precursor loading and deposition time was increased for experiment E5, and the desired coating was achieved with a significant nitrogen presence, discussed in detail in Section 4.1.3. This experiment was especially important for understanding the system and setting the course for future tests. In experiment E6, a flow controller malfunction resulted in highly varied flow rates. Based on the light vessel coating, the particle coatings were assumed to be negligible and were not further analyzed.

Table 4-2. Preliminary test experiment summary.

Experiment	E1	E2	E3	E4	E5	E6
Substrate	ZrO_2-SiO_2	ZrO_2-SiO_2	U-7Mo	U-7Mo	U-7Mo	U-7Mo
Ammonia Flow	None	Alternating	Alternating	None	None	None
Fluidization Flow Rate (L/min)	0.9	0.9	1.5	2.7	1.6	0.9-3.1
Run Time (hours)	30	48	90	23	94	96
Amount of Precursor (g)	0.6	1.85	1.96	2.26	4.5	4.15
RV Coating	n/a	None	None	Dark	Dark	Light
Particle Coating	Y	n/a	N	Y	Y	n/a

4.1.1 Characterization of Uncoated U-7Mo Microspheres

The starting material used in the first phases of this research was analyzed to better evaluate the coatings produced. The U-7Mo particles were observed using optical microscopy, as shown in Figure 4-1, and backscattered electron microscopy (BSE), as shown in Figure 4-2. These examinations documents the smooth texture of the uncoated sphere surfaces. However, the spheres consistently exhibited significant surface artifacts that may affect the texture of the coatings. The EDS spectrum shown in Figure 4-3 did not indicate significant oxygen content near the surface of the microsphere. This suggests that any preexisting oxidation is limited to a thin (less than 1 µm) surface layer.

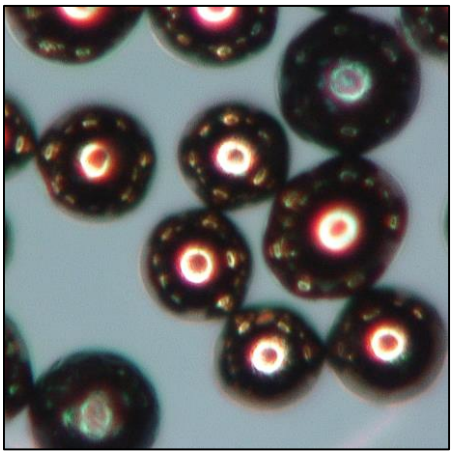

Figure 4-1. Optical images of U-7Mo particles.

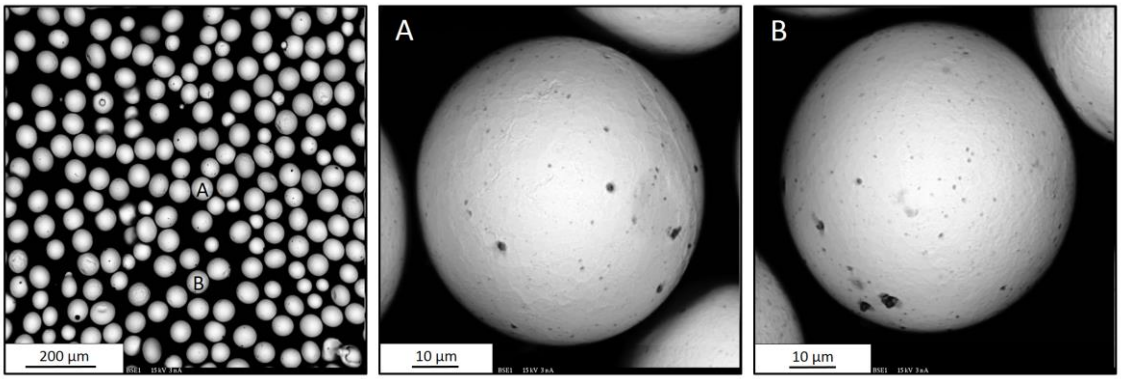

Figure 4-2. Backscattered electron images of uncoated U-7Mo spheres.

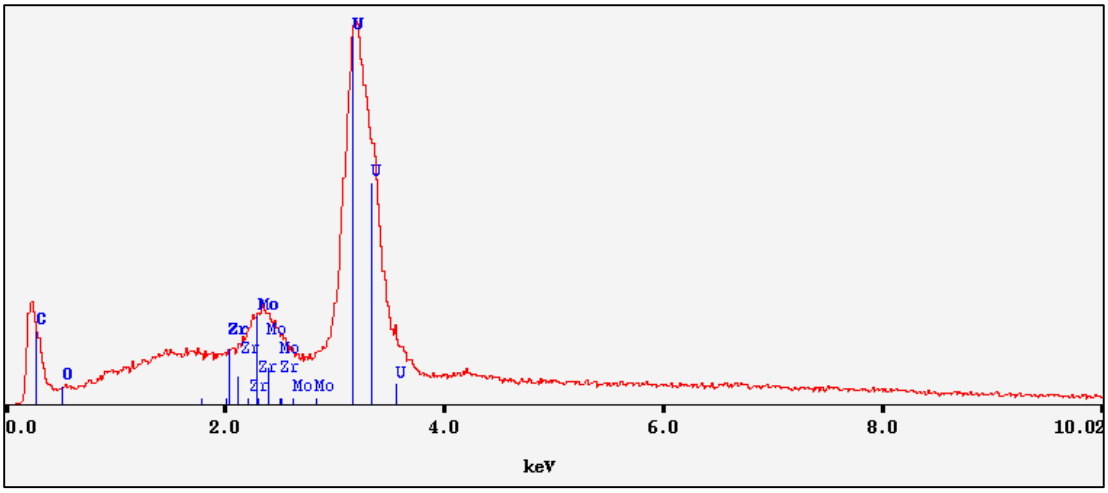

Figure 4-3. Energy dispersive X-ray spectroscopy data from uncoated U-7Mo sphere surface.

The BSE images of the polished sphere cross-sections are presented in Figure 4-4 and reveal a rough and cracked surface, with the most notable region indicated by the red arrows. This was partially due to effects of polishing and epoxy hardening. A preexisting oxide layer was not distinctly observed in these images, but thin layer may be obscured by rough surface texture and the low resolution of the imaging equipment.

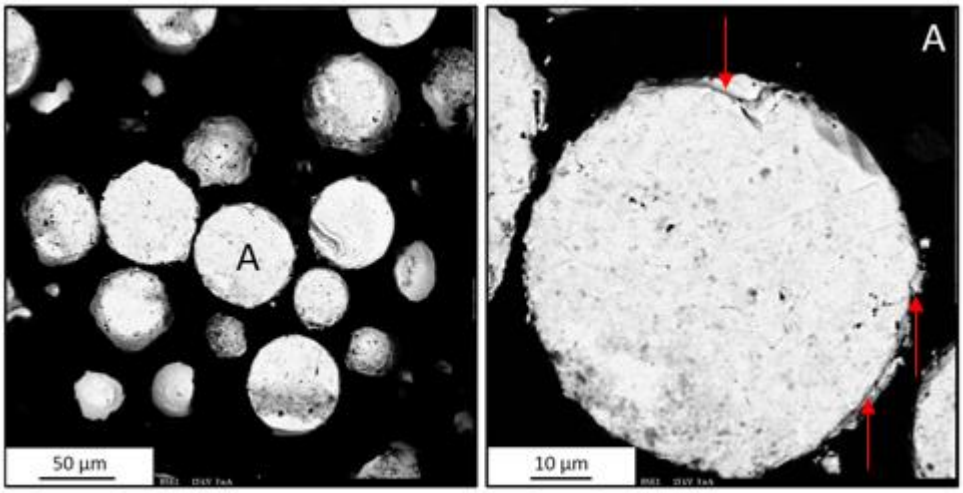

Figure 4-4. Backscattered electron image of uncoated U-7Mo sphere cross-section.

The microspheres were also analyzed by XRD to further identify the extent of oxidation of the sphere surface. The peaks in the resulting spectrum are described in Table 4-3. The major U-7Mo peaks were the dominant feature of the spectrum. However, small peaks corresponding to the major UO_2 peaks were observed [41]. The low intensity relative to that of the major U-7Mo peak hints at the existence of a thin oxidation layer on the surface.

Table 4-3. X-ray diffraction peak identification of uncoated U-7Mo.

°2Θ	d (Å)	Relative Intensity (%)	Compound
28.1	3.18	5.4	UO_2
37.1	2.42	100	U-7Mo
47.0	1.93	2.3	UO_2
53.4	1.72	47.4	U-7Mo
66.8	1.40	55.5	U-7Mo
78.9	1.21	15.3	U-7Mo

4.1.2 Characterization of the Results from E3

The results from Experiment E3 are presented here to illustrate the impact of utilizing alternation ammonia and precursor flow. Figure 4-5 shows images of the coated particles (left) taken with an optical microscope. The reaction vessel following the experiment is shown in Figure 4-5 (right). The discoloration at the bottom of the glass suggests that precursor transport occurred. However, the coating appears much lighter than expected for effective particle coating to have occurred.

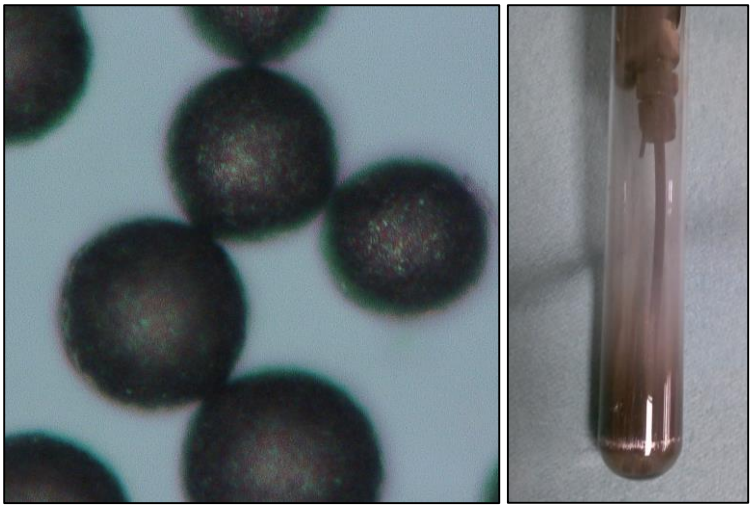

Figure 4-5. Optical images of experiment 3 particles (left) and reaction vessel (right).

The particles were analyzed at the Electron Microprobe Laboratory, and BSE images were taken of the coated sphere and the polished sample, shown in Figure 4-6. The BSE image of the sphere shows a rough surface, either a result of an uneven coating or the thick oxide layer, which may also produce the dark ring around the particles on the surface of the spheres. The lack of zirconium peak and large uranium and molybdenum peaks in the corresponding EDS spectrum, shown in Figure 4-7, suggests a negligible coating.

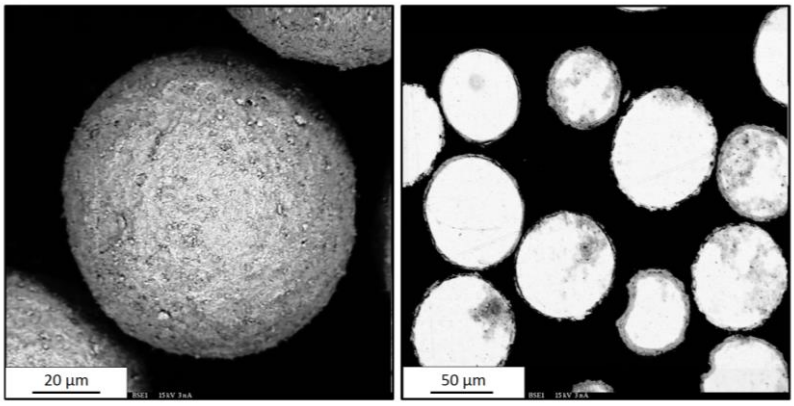

Figure 4-6. Backscattered electron images of E3 particle surface (left) and cross-sections (right).

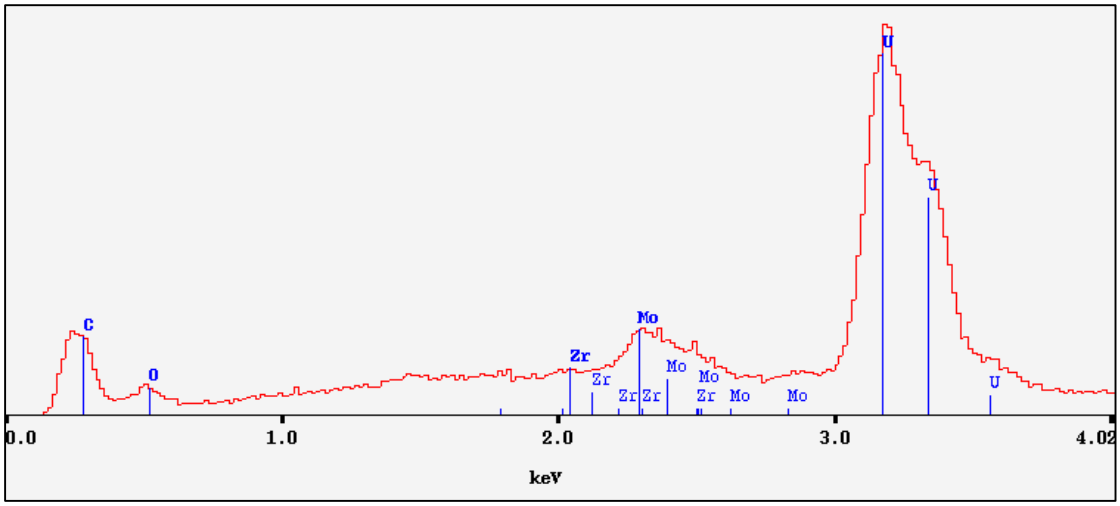

Figure 4-7. Energy dispersive X-ray spectroscopy data from E3 particle surface.

X-ray maps of the edge of the surface of the polished sample were taken to determine if a layer of ZrN is present. Figure 4-8 shows the maps for N, Mo, O, U, and Zr. Since the particles were carbon-coated before placement in the EPMA, the presence of carbon impurities in the coating was not investigated. The images show a thick U/Mo oxide layer on the surface of the spheres. The apparent thickness of this layer compared to that in the starting material could provide evidence of the growth of an oxide layer within the system. The nitrogen map was inconclusive due to high background counts from the dense sphere and oxide layer. However, there is also a distinct presence of zirconium at the outer edge of the sphere, shown more clearly against the background in the dense material in Figure 4-9. The nitrogen, molybdenum, and oxygen maps were overlaid for better viewing of the relative locations of the layers. The zirconium layer is on the surface of the oxide layer, however the apparent thickness of the zirconium layer is not true to the actual thickness. The resolution of the BSE is about 1 µm, so a layer less than 1 µm thick will appear thicker due to the scattering of the electrons. The coating was too thin to determine the thickness of the ZrN nitride layer and the ratio of zirconium and nitrogen in the layer. General Motors Research (GMR) thin film software was used to estimate the thickness of the coating based on the counts from WDS. This software compared the WDS data from the sample to that of a zirconium metal standard to estimate

the weight percent of zirconium in the sample. The thickness was then estimated to be 1-2 nm assuming a coating density consistent with that of ZrN (7.09 g/cm^3) with no oxygen present, but this estimate is not based on measurable data.

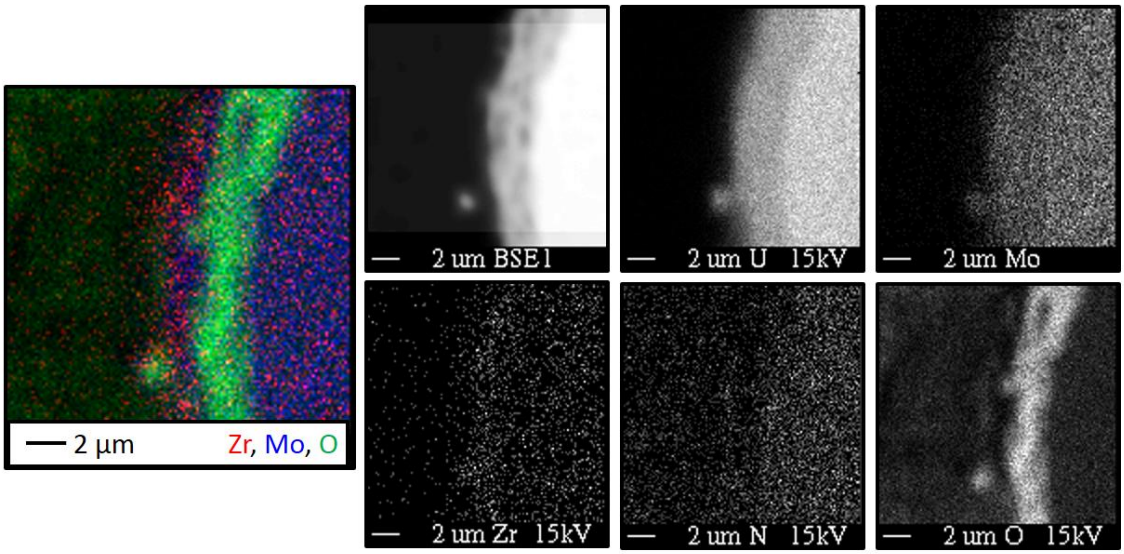

Figure 4-8. X-ray map of E3 particle cross-section.

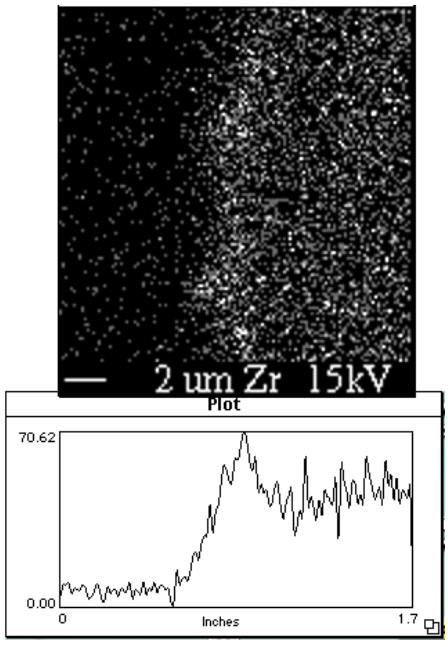

Figure 4-9. Zirconium signal of E3 along the particle edge.

4.1.3 Characterization of Results from E5

The coatings produced in experiment E5 were observed using a Hirox optical microscope, shown in Figure 4-10. The dark coating visually observed on the reaction vessel glass, also shown in Figure 4-10, revealed that to the entire heated zone had been coated. This discoloration suggested effective precursor transport and coating.

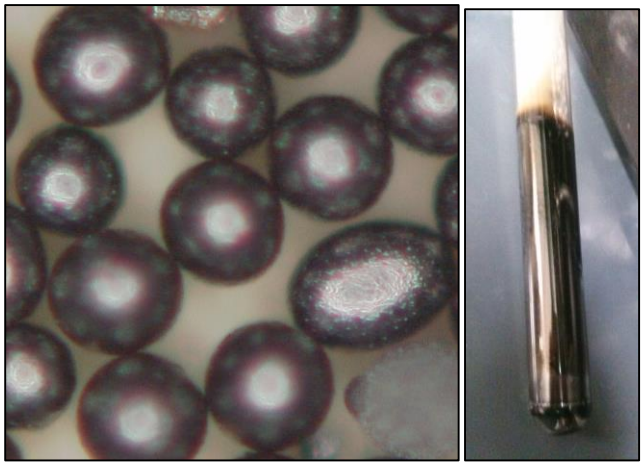

Figure 4-10. Optical images of E5 coated particles (left) and reaction vessel (right).

The particles from E5 were analyzed at the Electron Microprobe Laboratory. The coated spheres and polished sample were carbon coated prior to analysis. BSE images were taken of the coated sphere surfaces, as shown in Figure 4-11. The EDS spectrum, also shown in Figure 4-11, shows a strong zirconium presence on the surface. The negligible detection of uranium and molybdenum peaks suggests that the coating is thick enough to prevent detection of the bulk particle and the oxide layer, i.e. at least 1 μm thick.

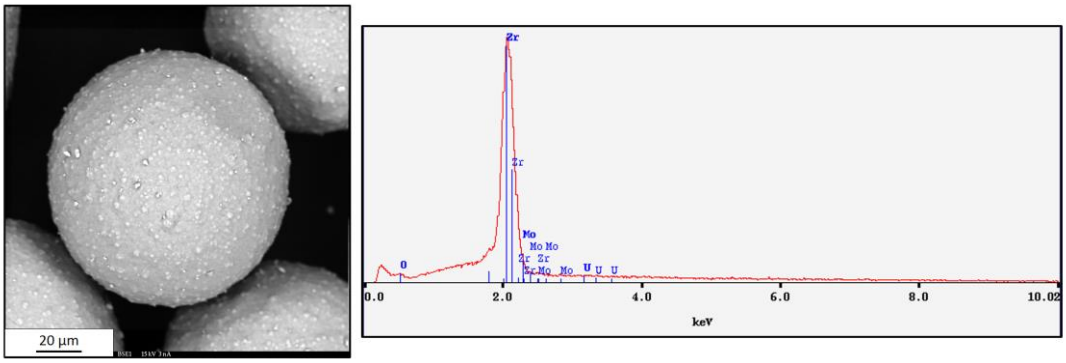

Figure 4-11. Backscattered electron image (left) and energy dispersive X-ray spectroscopy data (right) of E5 coated particle surface.

A WDS scan was performed across the edge of a polished particle by collecting WDS data at the characteristic peak energies in 1 µm increments. The results, shown in Figure 4-12, show a drop in uranium and molybdenum corresponding to a rise in zirconium and nitrogen showing an approximately 2 µm coating. The oxygen signal begins to increase at µm 6 where U-Mo starts to drop off but before the zirconium signal begins to rise. This suggests the presence of a U-Mo oxide layer. Since the zirconium-based coating appears to have been deposited on top of this layer, the oxide layer was likely present at the start of the CVD process. The high oxygen signal continues past the apparent oxide layer into the coating, but decreases as the measurements are taken further from the bulk material. Therefore, the oxygen concentration in the coating seems to be higher nearer to the bulk material.

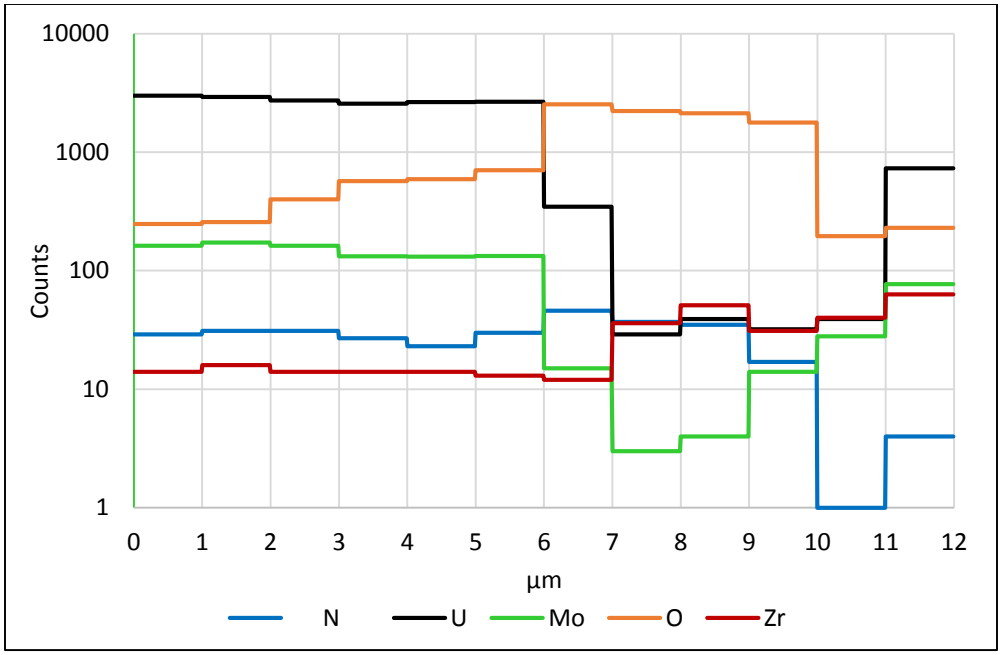

Figure 4-12. Wavelength dispersive X-ray spectroscopy scan across the E5 cross-sectioned particle edge.

X-ray maps of the edge of the surface of the polished sample were taken to determine if a layer of ZrN is present. Figure 4-13 shows the X-ray maps for nitrogen, molybdenum, oxygen, uranium, and zirconium at 5000x for a polished sphere edge and the interface between two spheres. Since the particles were carbon-coated before placement in the EPMA, the presence of carbon impurities in the coating was not investigated. The images show an oxide layer covered by thick, mostly even coating consisting of zirconium and oxygen. The apparent thickness of the oxide layer relative to that observed in the starting material provides evidence that the oxide layer grew within the system. There also appears to be nitrogen present in the coating, but the high background signal in the high density material makes this difficult to see. In previous experiments, the oxygen signal was attributed to the oxide layer and a thin or partial coating. In this case, however, the coating is thick enough to distinguish from the oxide layer underneath, showing that oxygen does appear present within the coating.

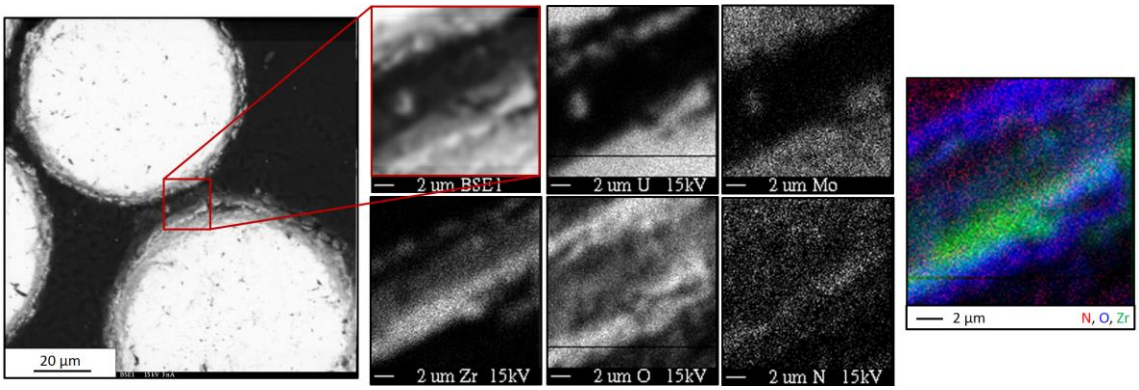

Figure 4-13. X-ray distribution maps of E5 particle cross-sections.

The coatings were also analyzed by X-ray diffraction (XRD). The resulting peaks, described in Table 4-4, were compared to those of known UO_2, U-7Mo, zirconium oxide, and zirconium nitride spectra. The dominant features in the spectrum were strong UO_2 peaks. The increase in intensity of these peaks compared to the starting material was not only attributed to the growth of the oxide layer, but also to a reduced penetration of the X-rays through the oxide layer to the bulk material caused by a thick coating. Traces of U-7Mo were still observed, but had significantly reduced in intensity due to growth of the surface layers. Significant zirconium oxide peaks were also observed, although the primary ZrO_2 peak was likely mixed with the major UO_2 peak. The major ZrN peak was not observed, however it may exist at low intensity and be hidden by an overlapping zirconium oxide peak.

Table 4-4. X-ray diffraction peak identification of E5 coatings.

°2Θ	**d (Å)**	**Relative Intensity (%)**	**Compound**
28.3	3.16	100	UO_2, ZrO_2
30.0	2.98	20.8	ZrO_2
31.7	2.82	22.4	ZrO_2
32.8	2.73	53.5	UO_2
34.5	2.60	12.3	ZrO_2, ZrN
36.9	2.44	14.4	U-7Mo
47.0	1.93	59.5	UO_2
55.8	1.65	52.8	UO_2, U-7Mo

A quantitative analysis was performed by WDS using UO_2, Mo, Zr, and BN standards. Data points were collected using a 5 x 5 grid with 5 µm spacing on the surface of the two spheres. The average values of the atom percentages are shown in Table 4-5. Negligible amounts of uranium and molybdenum were detected. The amount of zirconium and nitrogen atoms present in the coating were similar. Oxygen was observed at a slightly higher percentage. The values were similar between the two spheres, suggesting consistent coating across the particle surfaces. The source of high oxygen content in the coating is unknown, but may be attributable either to high oxygen content in the Ar line, leaks in the system, or oxygen from the U/Mo oxide layer interacting with the coating atoms.

Table 4-5. Quantitative analysis of the E5 coating content.

Element	**Sphere A**	**Sphere B**
Uranium (a%)	0.036 ± 0.027	0.027 ± 0.022
Molybdenum (a%)	0.014 ± 0.009	0.011 ± 0.011
Zirconium (a%)	30.34 ± 4.85	32.04 ± 6.71
Oxygen (a%)	37.41 ± 3.31	36.89 ± 4.59
Nitrogen (a%)	32.2 ± 3.05	31.04 ± 7.71

Particles coated during Exp. 5 were polished and sent to Idaho National Laboratory for further analysis using higher resolution equipment. Secondary electron (SE) imaging was performed at the interface of two particles, shown in Figure 4-14. Three distinct layers were observed on the surfaces of the bulk material. Energy-dispersive spectroscopy was performed to determine the composition of each layer. The innermost layer was identified as uranium oxide, and the intermediate porous layer was identified as primarily zirconium oxide. The outermost layer consisted of zirconium nitride, and did not appear to contain pores or columnar grains. The apparent thickness of the U/Mo oxide layer provided further evidence of the growth of an oxide layer within the system prior to coating. The appearance of distinct zirconium oxide and nitride dominant layers during the coating process. These results also provide evidence of the formation of multiple layers during the

coating process. This is supported by WDS data previously discussed and shown in Figure 4-12, showing the oxygen content decreasing in the coating further from the surface of the bulk material.

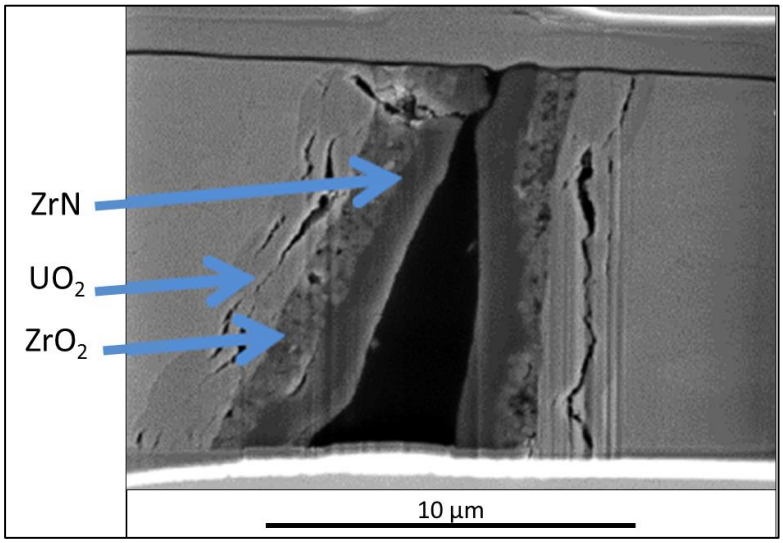

Figure 4-14. Secondary electron imaging of experiment 5 coating layers [42].

4.1.4 Characterization of Coatings by Wavelength Dispersive Spectroscopy

The WDS zirconium signal from each of the experiments analyzed is shown in Figure 4-15. In this set of experiments, since only E5 produced a coating at least 1 µm thick, the increase in intensity of the zirconium peaks relates to the increase in thickness of the coatings. The signal from E3, in which small amounts of ammonia were introduced in alternation with precursor flow, was insignificant compared to those that did not utilize ammonia in the system. The increase in coating thickness from E4 to E5 is likely caused by the extended deposition time and initial precursor loading.

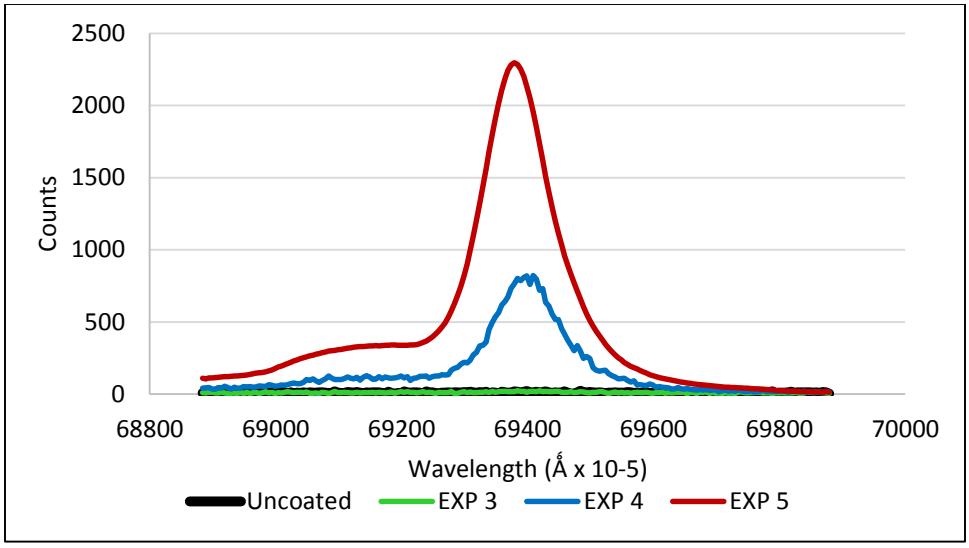

Figure 4-15. Wavelength dispersive X-ray spectroscopy data comparing the zirconium content in E3, E4, and E5 coatings.

The nitrogen signal from these experiments is shown in Figure 4-16. Although a slight nitrogen signal was seen in the uncoated material, attributed to high background and noise from the dense bulk material, a measurable increase was observed with increase in coating thickness, similar to the trend observed with zirconium. The oxygen signal, although distinctly present in the uncoated material, is significantly stronger in the coated material. This may largely be due to the characteristic X-rays being produced mostly in the region below the thin oxide layer in the starting material caused by the tear-drop shaped effect of the electron beam described in Section 3.5.1. However, the peak intensity does not change significantly between experiments 4 and 5. Since the observed coating thickness was much larger for those from E5, it was assumed that the oxygen content does not increase with coating thickness. Rather, due to the multi-layer structure of the coating shown in Figure 4-14, the analysis was largely detecting the U/Mo oxide layer and the zirconium oxide layers. Therefore, oxygen is likely present in similar concentrations in the U-Mo oxide layer and within the zirconium-based coating. The relatively low intensity of the nitrogen peaks compared to zirconium and oxygen is not indicative of elemental ratios.

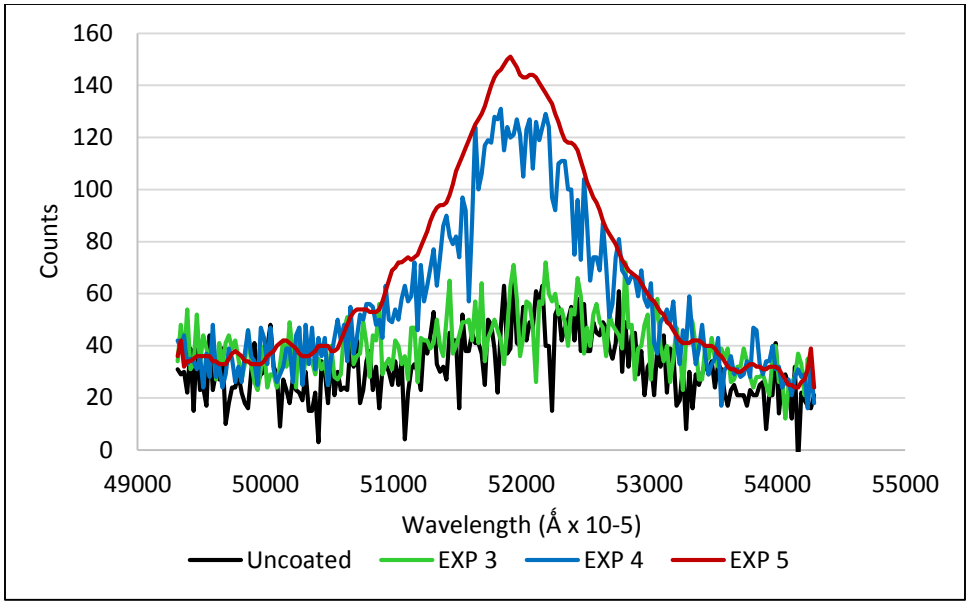

Figure 4-16. Wavelength dispersive X-ray spectroscopy data comparing the nitrogen content in E3, E4, and E5 coatings.

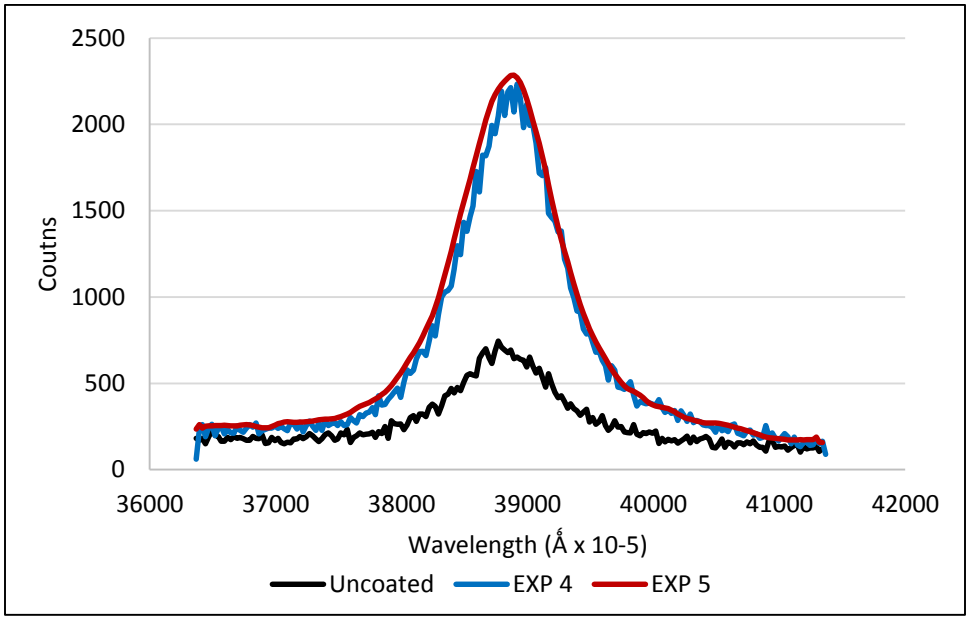

Figure 4-17. Wavelength dispersive X-ray spectroscopy data comparing the oxygen content in E4 and E5 coatings

4.2 System Modification Test Series

Experiments 7 to 12 were performed to test system modifications and develop repeatable procedures and to overcome gas flow and coating issues that were encountered in the first six test. Table 4-6 summarizes the test conditions of each experiment, and Figure 4-18 describes the major changes made in the reaction vessel for each experiment.

Table 4-6. Summary of experiments performed in the system modifications series.

Condition	EXP 7	EXP 8	EXP 9	EXP 10	EXP 11	EXP 12
Fluidization Flow Rate (L/min)	1.2	0.75	1.0	1.25	1.5	1.0
Run Time (hours)	48	1	24	24	96	96
RV Coating	No	No	Yes	Yes	Yes	Yes
Particle Coating	n/a	n/a	~1 µm	n/a	< 2 µm	2-3 µm

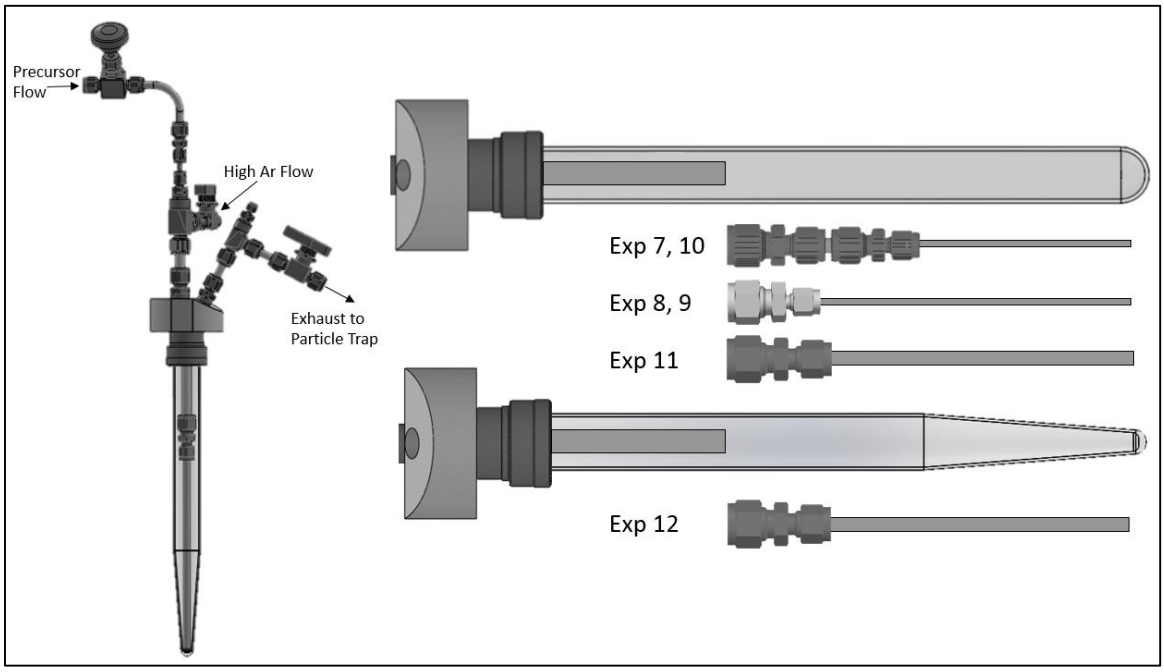

Figure 4-18. Reaction vessel configurations for system modification tests.

Experiment 7 was the first test of the new reaction vessel design. There was not a coating observed on the reaction vessel glass after 48 hours, so it was assumed that the precursor was not transporting to the vessel effectively and the experiment was shut down. In experiment 8, the end of 0.32 cm (0.125 in.) tube in the reaction vessel was immediately clogged by a solid piece of TDMAZ. The end of the tube was re-cut and cleaned out to produce a wider opening.

A gradual and immediate reduction from 0.95 cm (0.375 in.) to a 0.32 (0.125 in.) tube inside the reaction vessel was tested in experiments 9 and 10, but both experiments clogged at the heated reducing joints. The 0.32 (0.125 in.) tube was replaced with a 0.64 cm (0.25 in.) tube to reduce flow restrictions. Experiment 11 experienced fluidization issues with the flow exiting the 0.64 cm (0.25 in.) tube. After ~ 8 hours, the vacuum pump experienced a malfunction and the system exhausted to air at the particle trap. The fluidization flow rate was increased to 1.75 L/min to accommodate the lack of vacuum.

The reaction vessel glass was designed with a tapered end to address fluidization issues with the 0.64 cm (0.25 in.) tube [43]. Experiment 12 experienced issues with various flow restrictions after ~40 hours. The flow varied for the next 24 hours before the system was shut down. The experiment was restarted by storing the vessel in the glovebox and replacing the 0.64 cm (0.25 in.) tube. The bubbler was cleaned and reloaded with ~5 g of fresh TDMAZ. About 8.5 g of U-7Mo was recovered and reused. After ~43 hours, the precursor carrier gas flow rate had drastically reduced while the fluidization flow rate was unaffected. The temperature in the tube was reduced from 75°C to 60°C, and the flow rate began to increase to the set value. The experiment ran without issue for the next 53 hours.

4.2.1 Characterization of the Results from Experiment 11

The dark coating visually observed on the reaction vessel glass and outer surface of the transport tube, shown in Figure 4-19, corresponds to the entire heated zone. Based

on observations from previous experiments, this discoloration suggests a substantial particle coating.

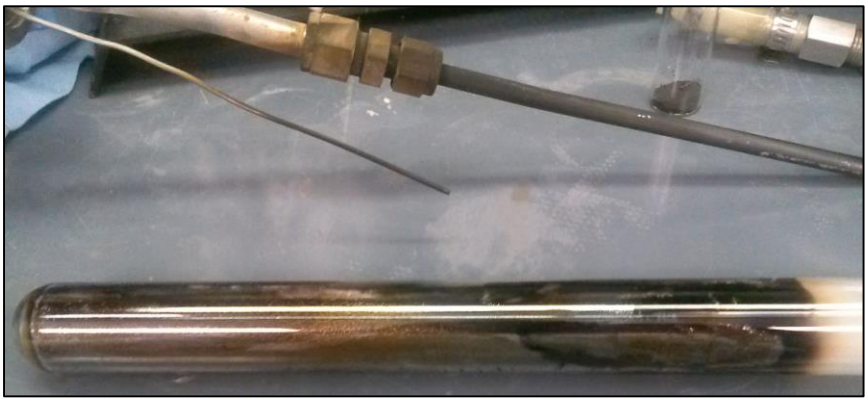

Figure 4-19. Experiment 11 coated reaction vessel.

The BSE image of a sample of particles from Exp 11, shown in Figure 4-20 showed inconsistency among the particles. SE imaging showed this was partially due to spheres that were not fully carbon coated and in contact with the carbon tape. However, EDS analysis confirmed the particle coatings were inconsistent as shown in Figure 4-21 through Figure 4-23. Particles A, B, and C represent partially coated, fully coated, and uncoated particles, respectively. It was suspected the particle bed was not fully fluidized after the vacuum pump was removed during the experiment.

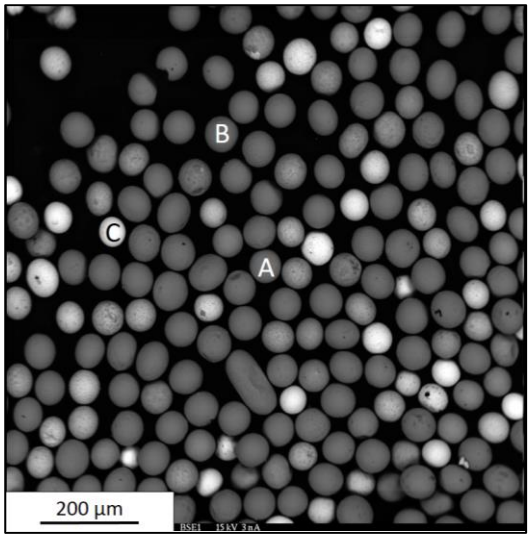

Figure 4-20. Backscattered electron image of experiment 11 particle surfaces.

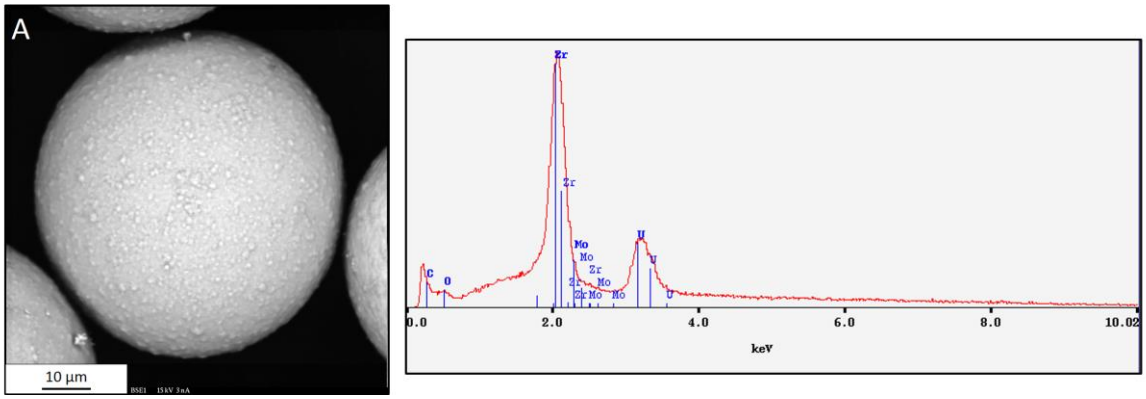

Figure 4-21. Backscattered electron image and energy dispersive X-ray spectroscopy data from particle A.

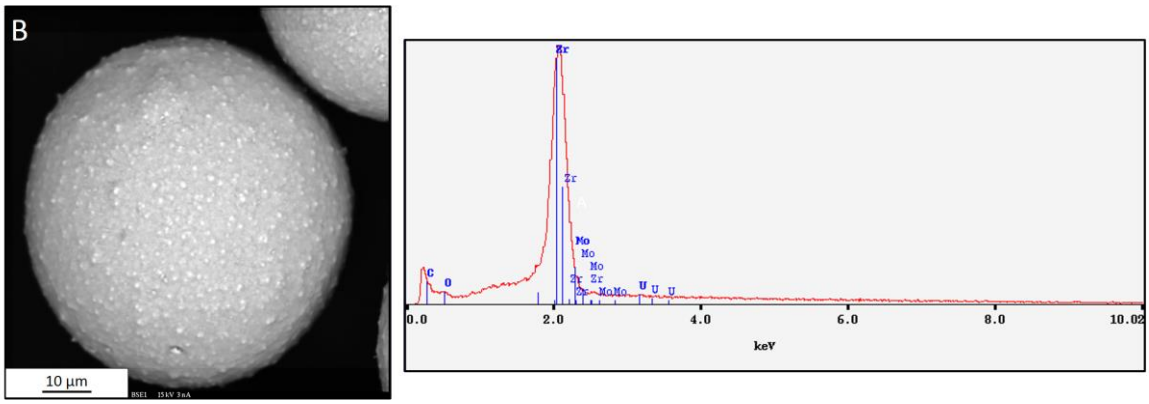

Figure 4-22. Backscattered electron image and energy dispersive X-ray spectroscopy data from particle B.

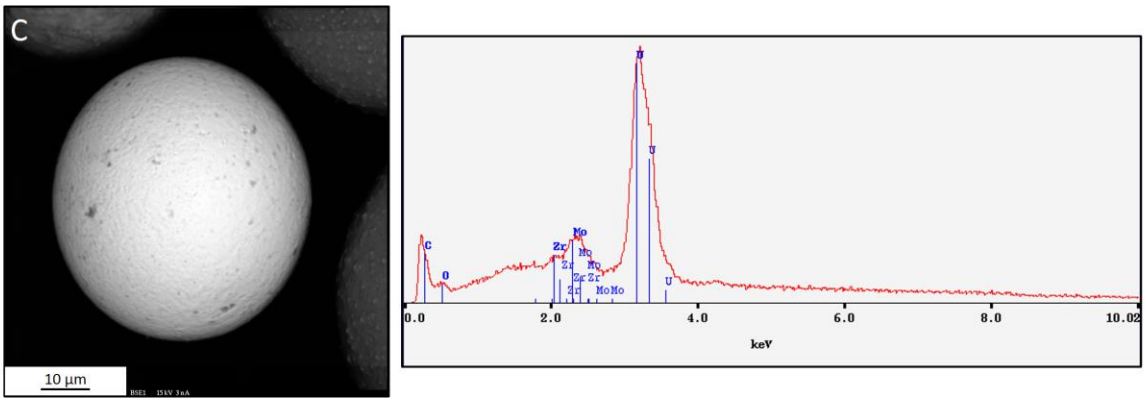

Figure 4-23. Backscattered electron image and energy dispersive X-ray spectroscopy data from particle C.

One polished particle was analyzed for this intermediate experiments. The particle was chosen based on the quality of its polish and small apparent rounding effects of the polish. The area marked in the BSE image shown in Figure 4-24 was selected to analyze the coating characteristics using X-ray mapping. The X-ray maps on the edge of the polished sphere, shown in Figure 4-25 show U-Mo bulk with an oxide layer extending into the zirconium coating. A distinct nitrogen layer also corresponds with zirconium presence. The imaging technique cannot resolve less than 1 µm so the layers cannot be distinguished.

.

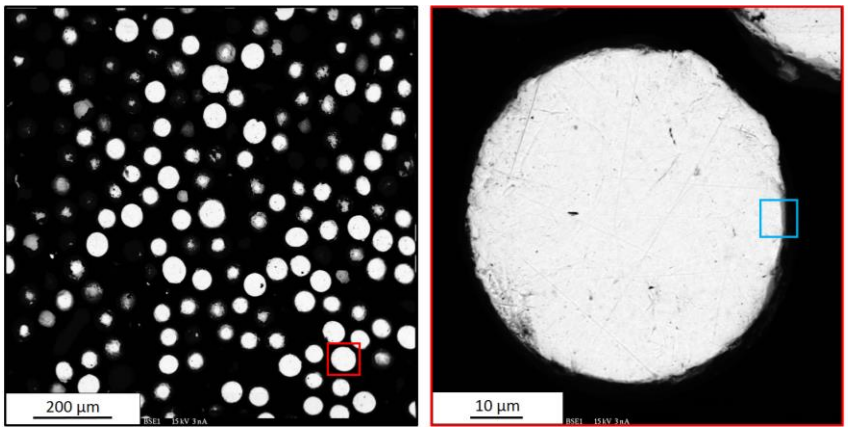

Figure 4-24. Backscattered electron image of experiment 11 particle cross-section.

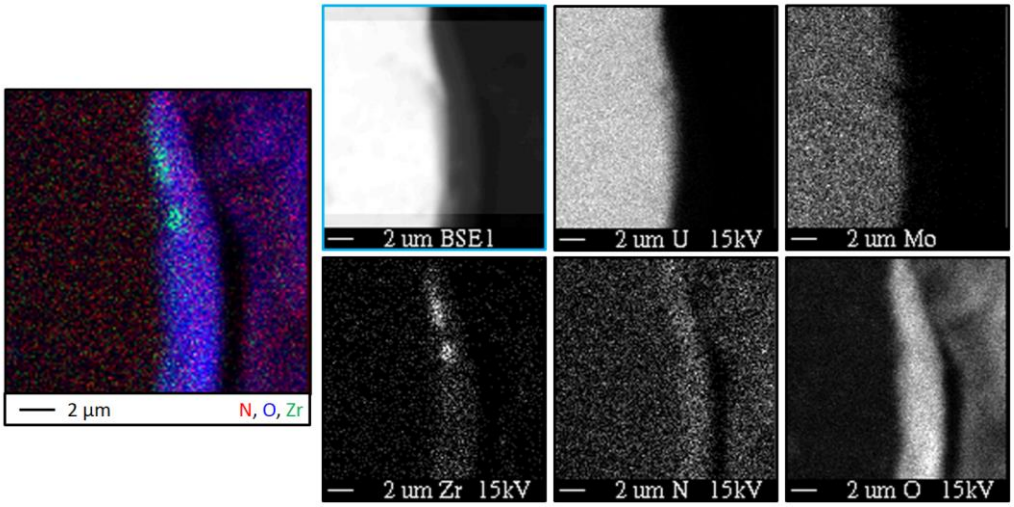

Figure 4-25. X-ray maps of experiment 11 particle cross-section.

A WDS analysis, shown in Figure 4-26 was performed with 1 µm increments across the sphere edge, with the 0 point taken within the bulk particle and the 12 um point within in the epoxy. There is a rise in zirconium, nitrogen, and oxygen content that corresponds to a drop on U-Mo between 6 and 8 µm. This suggest a coating of less than 2 µm, but resolution prevents accurate estimation of the coating thickness.

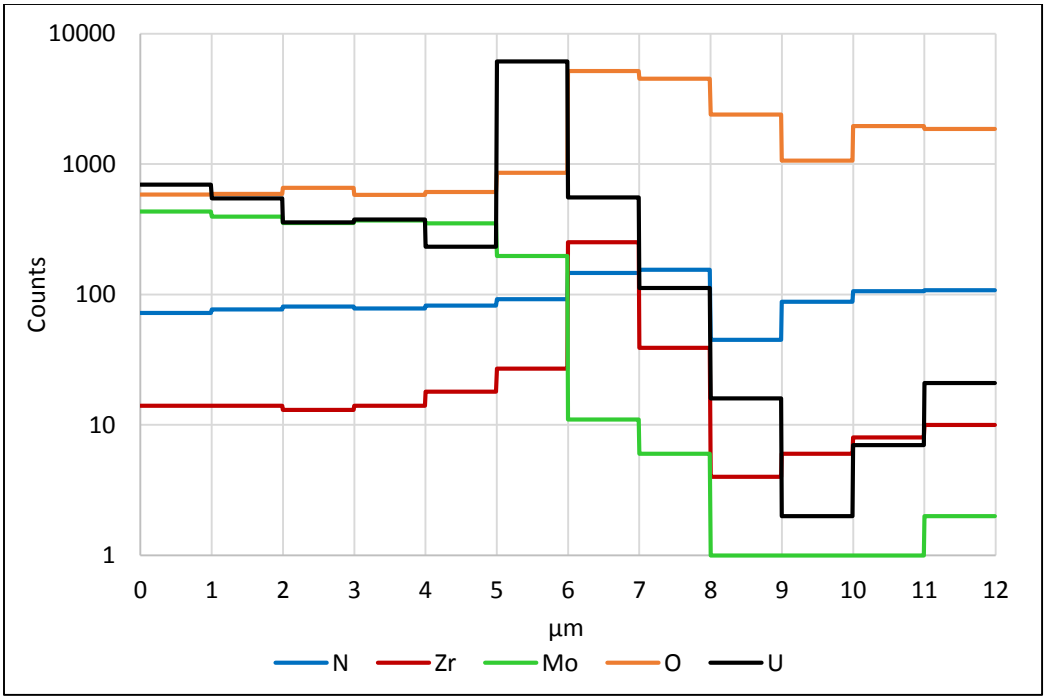

Figure 4-26. Wavelength dispersive X-ray spectroscopy scan across the experiment 11 cross-sectioned particle edge.

4.2.2 Characterization of the Results from Experiment 12

The dark coating visually observed on the reaction vessel glass, shown in Figure 4-27, corresponds to the entire heated zone. Based on observations from previous experiments, this discoloration suggested that substantial particle coating was achieved.

Figure 4-27. Experiment 12 reaction vessel coating.

BSE images, shown in Figure 4-28, reveal coatings with varying surface textures. Four particles of different sizes and textures were selected for EDS analysis. All of which showed strong zirconium peaks and absent uranium and molybdenum peaks, shown in

Figure 4-29, suggesting consistently thick coatings. Unlike those seen in previous experiments, the BSE images do not show a variety in the brightness of the spheres. This suggests the tapered vessel enabled the particle bed to fully fluidize and evenly coat the population. The particles with a rougher texture had larger oxygen peaks in the EDS spectrum, presumably due to holes in the rough coating allowing the beam to penetrate into the coating.

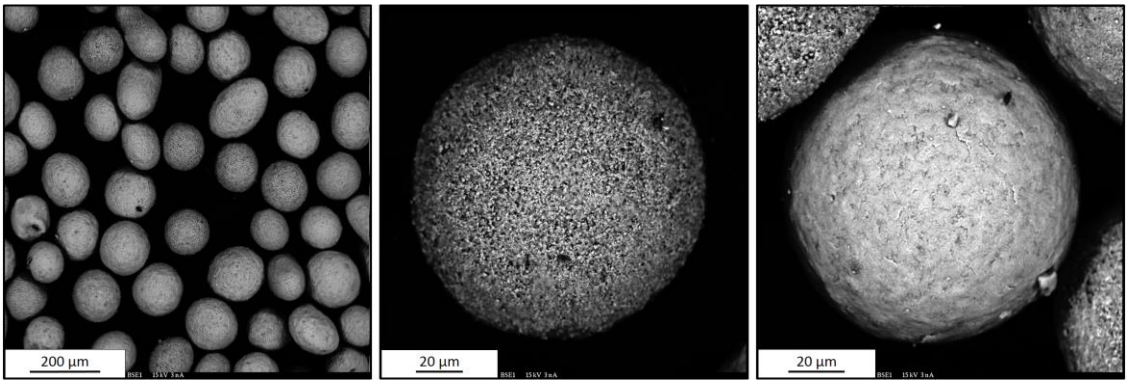

Figure 4-28. Backscattered electron images of experiment 12 particle surfaces.

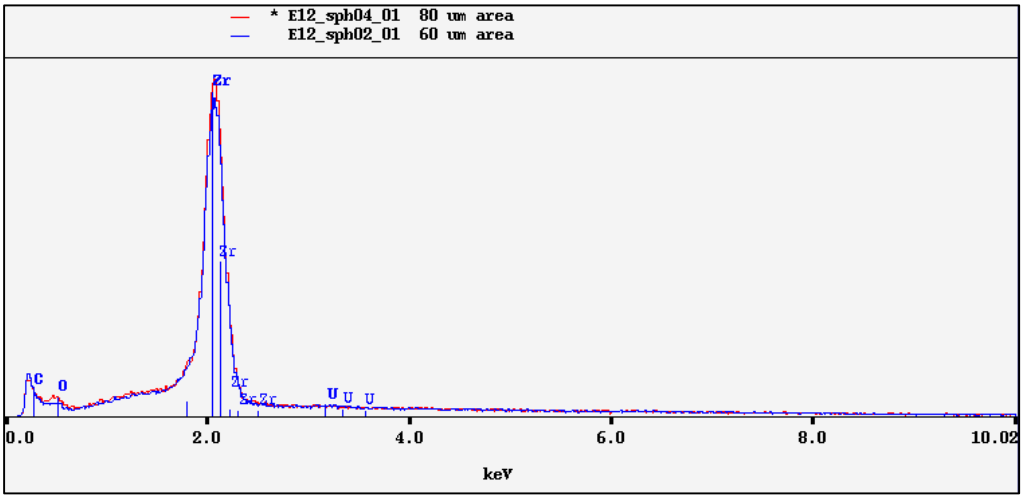

Figure 4-29. Energy dispersive X-ray spectroscopy data from experiment 12 particle surfaces.

BSE images of the polished sample, shown in Figure 4-30, revealed coating thicknesses greater than 2 µm. The appearance of very thick coatings (greater than 5 µm) on some particles, such as particle A, may not be representative of the actual coating thickness due to the location of the polished surface with respect to the midplane of the particle. X-Ray maps were taken of the edge of sphere B as noted in Figure 4-30, showing a thick layer of zirconium with oxygen-rich regions, described in Figure 4-31. Small amounts of nitrogen were detected within the coating, but it was less than the nitrogen content in the epoxy and noise from the dense U-Mo material.

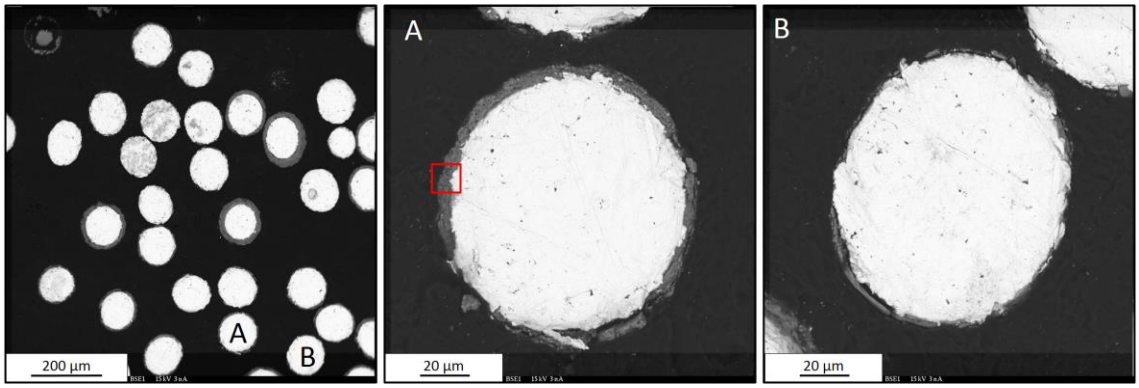

Figure 4-30. Backscattered electron images of Experiment 12 particle cross-sections.

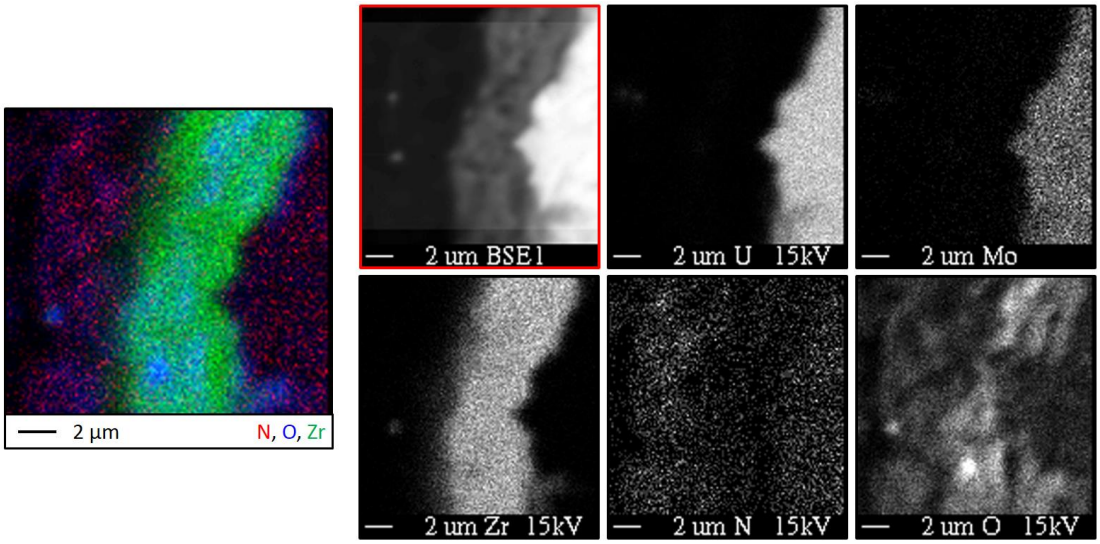

Figure 4-31. X-ray maps of experiment 12 particle edge cross-section.

4.2.3 Characterization of Coatings by Wavelength Dispersive Spectroscopy

In this set of experiments, since each experiment analyzed produced an estimated coating thickness greater than or equal to the beam penetration depth of 1 µm, it was not expected to observe similar trends relating to coating thickness as apparent in the previous set of experiments. Instead, a significant change in the signal between coatings of different thicknesses would represent a gradient in the zirconium concentration throughout the coating. Therefore, the similar zirconium peak intensities shown in Figure 4-32 is considered to represent similar zirconium concentrations in each of the coatings.

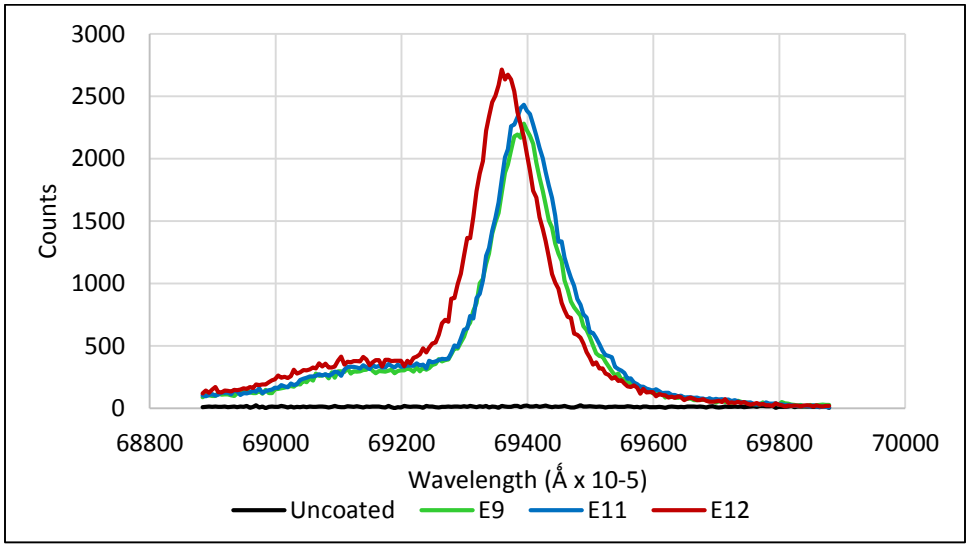

Figure 4-32. Wavelength dispersive X-ray spectroscopy data comparing the zirconium content in experiments 9, 11, and 12.

The nitrogen signal from each of the experiments is shown in Figure 4-33. A background nitrogen signal was observed in the uncoated material, but a distinctly higher signal was observed in the coated particles. The oxygen content, although present in the uncoated material, once again experienced a strong increase in the coated material, as shown in Figure 4-34. An inverse relation was observed between the oxygen and nitrogen signals, suggesting that oxygen and nitrogen deposition are competing processes. The reduction in oxygen intensity in later experiments may signify a reduction in leaks in the

system as a result of system modifications or may correspond to the development of a nitrogen rich layer over an oxygen rich layer in thicker coatings as suspected from the high resolution secondary electron image produced at Idaho National Laboratory (Figure 4-14).

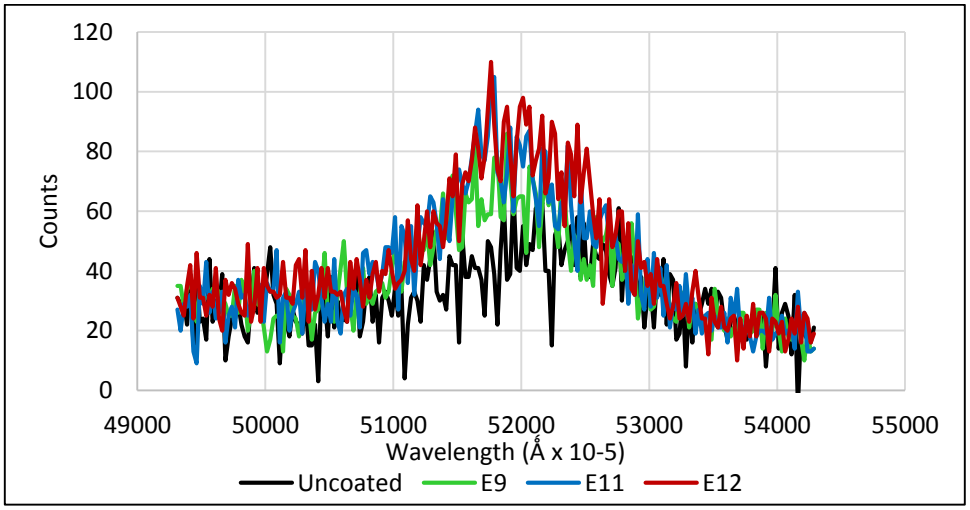

Figure 4-33. Wavelength dispersive X-ray spectroscopy data comparing the nitrogen content in experiments 9, 11, and 12.

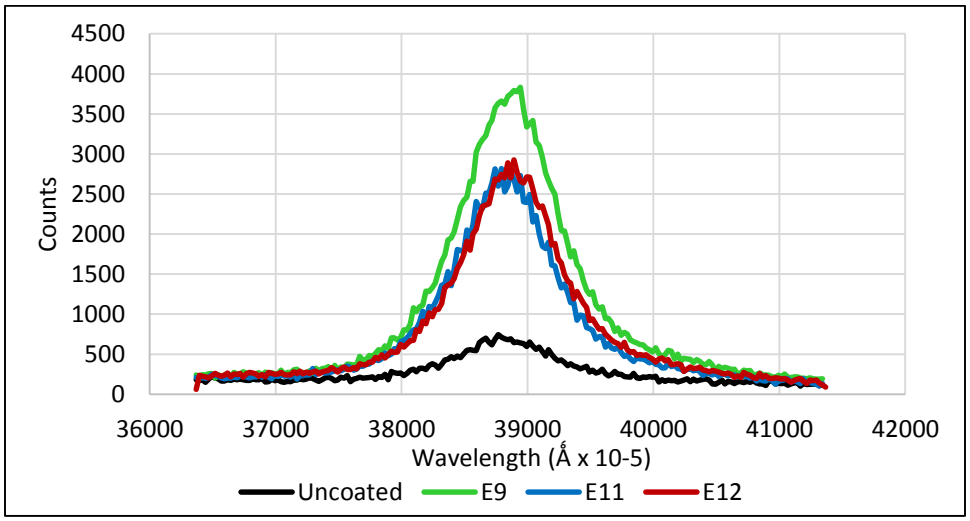

Figure 4-34. Wavelength dispersive X-ray spectroscopy data comparing the oxygen content in experiments 9, 11, and 12.

4.3 Parametric Study of Process Variables

The final phase of this research examined the effects of certain parameters on the coating production. A matrix of experiments was designed to study conditions including time allotted for coating deposition, precursor flow rate, and air exposure following the deposition reaction. The results of these experiments are summarized in the following sections.

4.3.1 Characterization of Uncoated U-8Mo Microspheres

The experiments discussed in Section 4.3 utilize U-8Mo microspheres produced at INL as the deposition substrate. The particles were sieved and partitioned according to diameter and stored inside a glovebox until use. Analyses was performed to determine the condition of the particle surfaces.

The BSE images revealed a variety of surface textures, shown in Figure 4-35, as well as particles shapes and surface defects. The EDS spectrum of the two spheres in Figure 4-36 confirmed a surface with minimal pre-existing oxidation. The BSE image of the polished sphere cross-sections in Figure 4-37 did not show a distinct oxide layer. However, surface fracturing was once again observed, assumed to be caused by epoxy shrinking as it hardens.

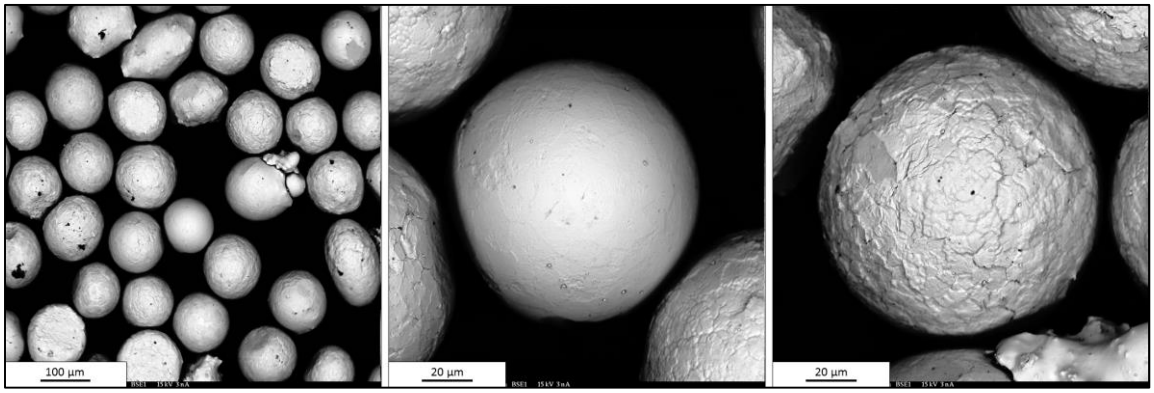

Figure 4-35. Backscattered electron images of uncoated U-8Mo sphere surfaces.

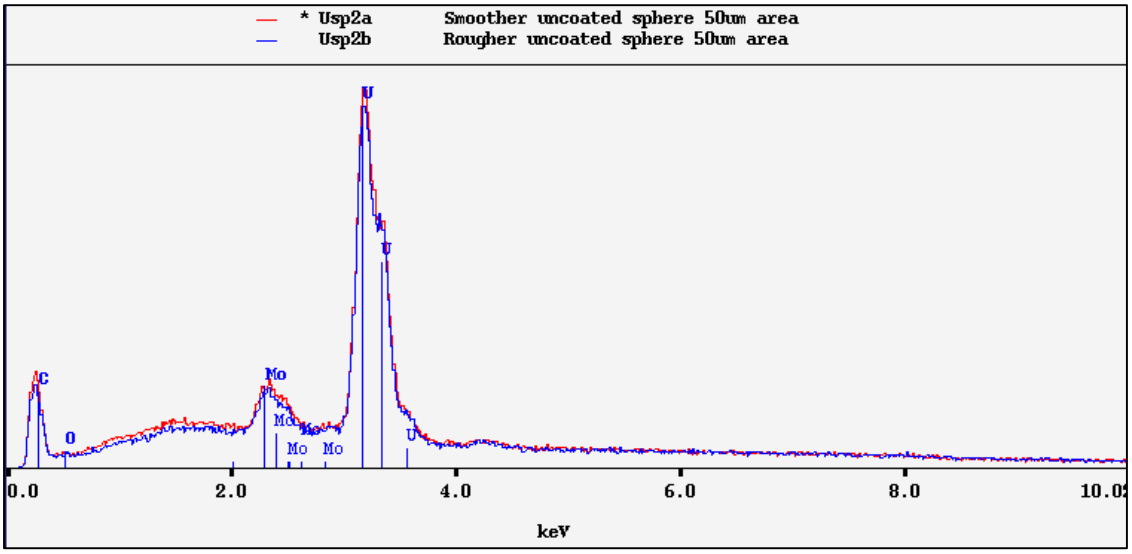

Figure 4-36. Energy dispersive X-ray spectroscopy data from uncoated U-8Mo surfaces.

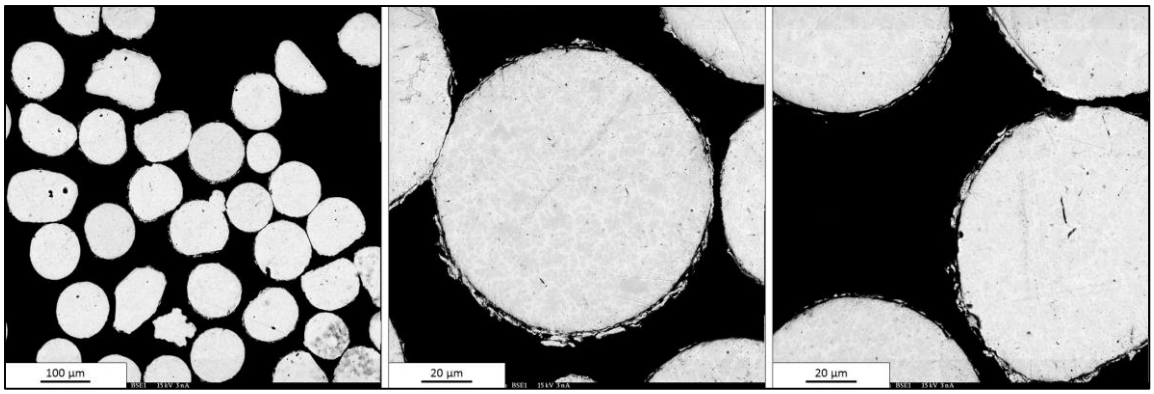

Figure 4-37. Backscattered electron images of uncoated U-8Mo sphere cross-sections.

4.3.2 Description of Results from Baseline Experiments

Baseline experiments were originally planned to operate for 4 days. After the first two attempts were unsuccessful due to flow restrictions and oxidation issues during operation, the operation time was decreased. Baseline experiments 3 (B3) and 5 (B5) were terminated after 1.5 and 2 days, respectively. Both experiments began to experience flow restrictions immediately prior to shut down, but yielded observable particle coatings.

4.3.2.1 Characterization of the Results from Baseline Experiment 3

The surface of the spheres coated in baseline experiment 3 are shown in the BSE images in Figure 4-38. The spheres appeared fully coated demonstrated by similar degrees of brightness across the surface. The surface texture was consistent among most of the population, indicating complete fluidization of the particle bed. The coating content was also consistent, observed by the almost identical EDS spectra of different particles in Figure 4-39.

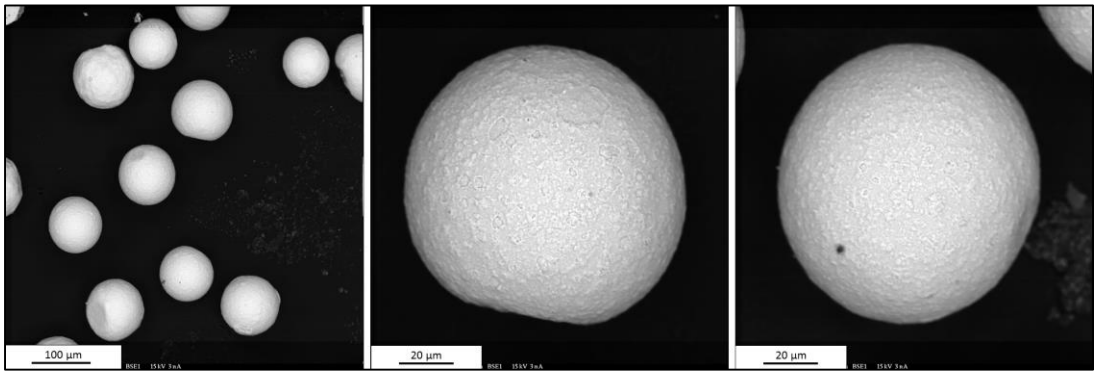

Figure 4-38. Backscattered electron images of sphere surface from Baseline 3 coatings.

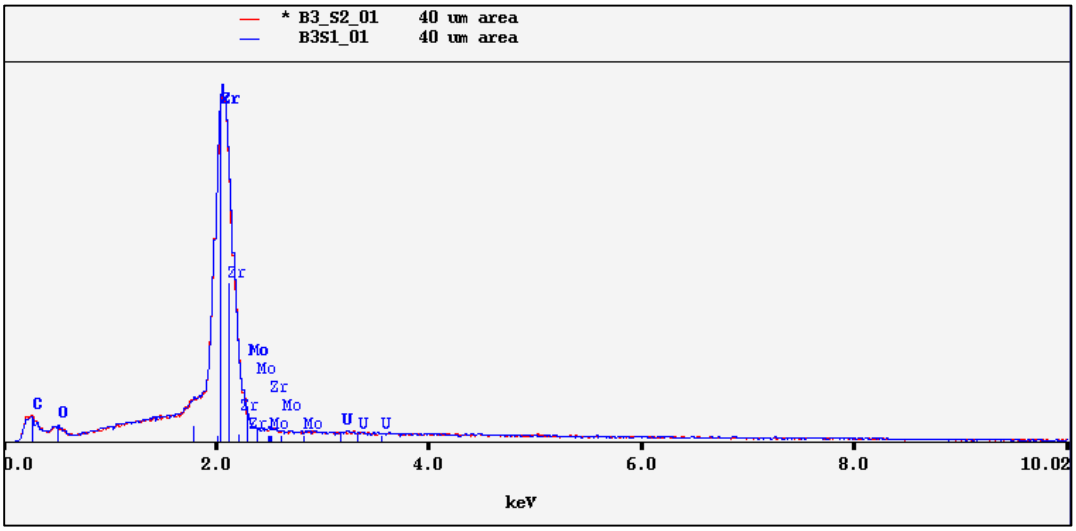

Figure 4-39. Energy dispersive X-ray spectroscopy data from B3 coatings.

The polished cross-sections of the particles are shown in Figure 4-40. The surface appears relatively smooth with some surface artifacts. A magnified image of the interface between two spheres, shown in Figure 4-41, revealed an apparent coating on the surface of the bulk material. X-ray maps of expected elements confirmed that this layer was a zirconium-based coating rather than rounding effects of polishing. Nitrogen was still not observed in the coating using this technique, but a low concentration may be hidden by high noise from the dense bulk material. Oxygen was present throughout the coating. However, the oxide layer appeared thicker than the zirconium coating, suggesting the development of a U-Mo oxide layer prior to coating deposition.

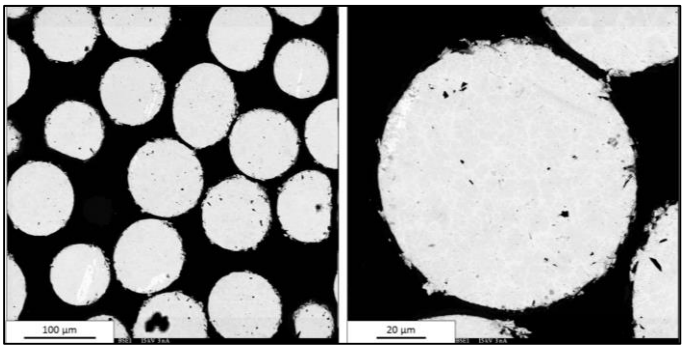

Figure 4-40. Backscattered electron images of polished cross-sections of B3 particles.

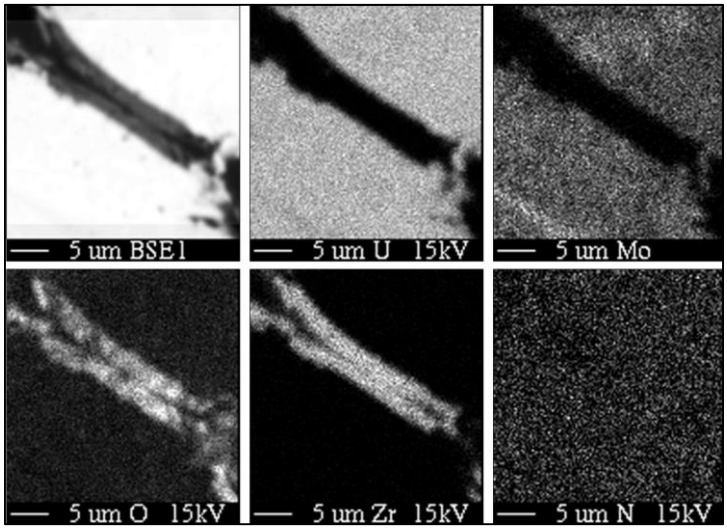

Figure 4-41. X-ray distribution maps of B3 coating.

The thickness of the coating was estimated using two techniques. First, the thickness of the coating was measured using the zirconium X-ray map shown in Figure 4-41 and comparing to the length of the shown scale bar. The thickness of the zirconium layer was measured at fifteen points across the surfaces of both spheres, resulting in an average thickness measurement of 2.1 ± 0.5 µm. A second technique used to confirm the estimated thickness from the X-ray map. A WDS scan for known elements, including nitrogen, zirconium, and uranium, was performed over 1 µm increments between the bulk material of two particles, crossing the sphere interface. The results, shown in Figure 4-42, reveal a zirconium rich region that corresponds to a uranium poor region. An intermediate region appears to exist, but due to the resolution of the technique, an accurate measurement was difficult to obtain. Therefore, the particle coating was estimated to be between 1.5 to 2 µm.

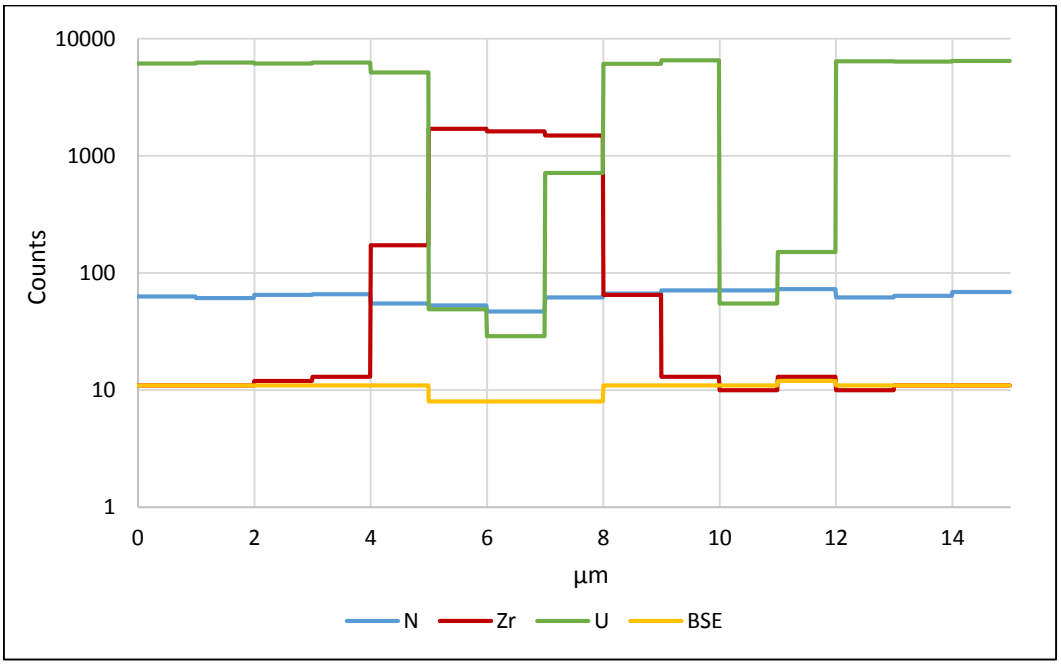

Figure 4-42. Wavelength dispersive X-ray spectroscopy scan across the interface between B3 spheres.

4.3.2.2 Characterization of the Results from Baseline Experiment 5

The coated reaction vessel is shown in Figure 4-43. The dark coloration that corresponded to the entire heated region was an indication that a coating of measurable thickness was produced. The coated sphere textures were observed through BSE images in Figure 4-44. The coating was consistent between particles, but the appearance of brighter particles suggests that there was a small stagnant region in the particle bed. This was suspected from visual observation at the beginning of the experiment caused by improper alignment and spacing between the bottom of the tube and glass. The coatings appeared to consist of regions with different compositions, indicated by the varied brightness across the surface. On average, the coating composition was consistent between particles, shown by the similar EDS spectra of different particles shown in Figure 4-45.

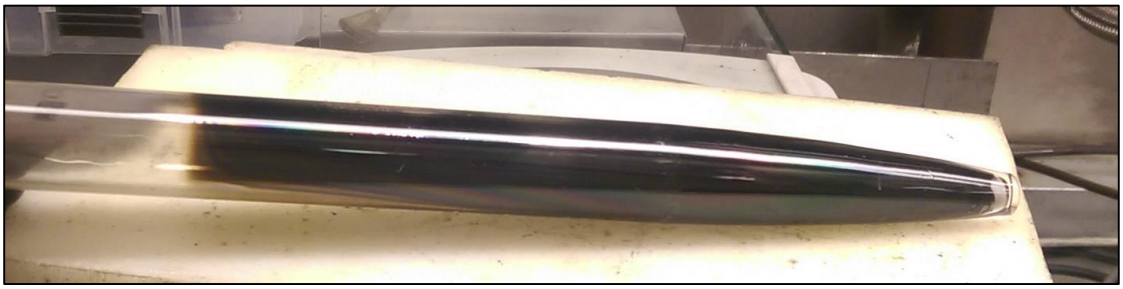

Figure 4-43. B5 coated reaction vessel.

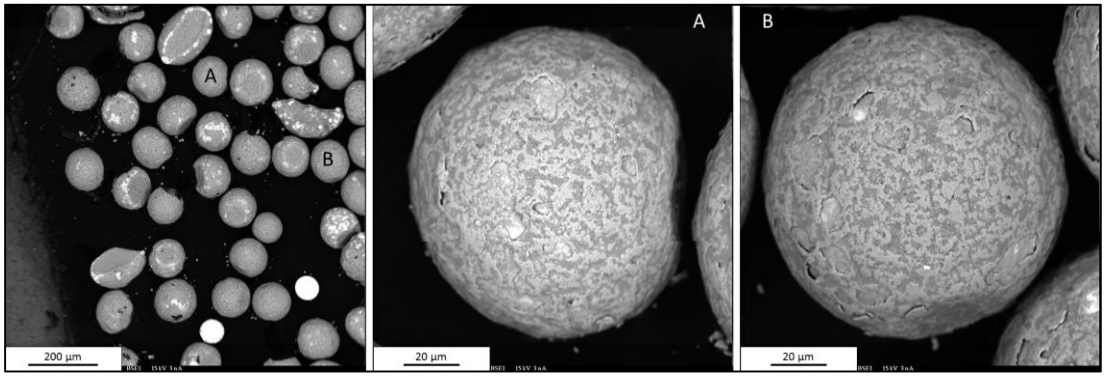

Figure 4-44. Backscattered electron images of B5 coated sphere surfaces.

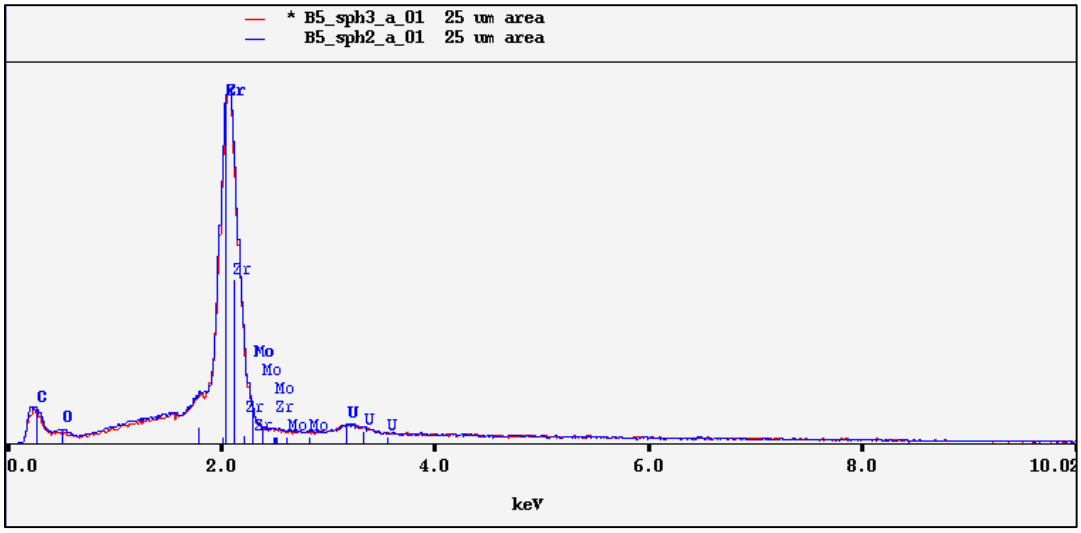

Figure 4-45. Energy dispersive X-ray spectroscopy data from B5 coated sphere surfaces.

Small uranium and oxygen peaks were observed from the EDS spectrum of the surface. It was suspected that this was related to the regions observed in the BSE images. EDS spectra were collected from smaller areas corresponding to the lighter and darker regions to more closely inspect the variations. The spectra in Figure 4-46 confirmed that the brighter region consisted of more uranium and oxygen near or on the surface than the darker region. The lighter region still showed a significant zirconium peak, but it was smaller than the darker region. This suggests that the lighter regions were more thinly coated as the beam was still able to penetrate to the bulk material to detect uranium. Since the oxygen peak was also higher in the thinner coatings, this could suggest that the oxygen content decreases in the coating further from the bulk material. However, the peak differences could be caused by the detection U-Mo oxide layer beneath the coating with a higher concentration of oxygen than the coating.

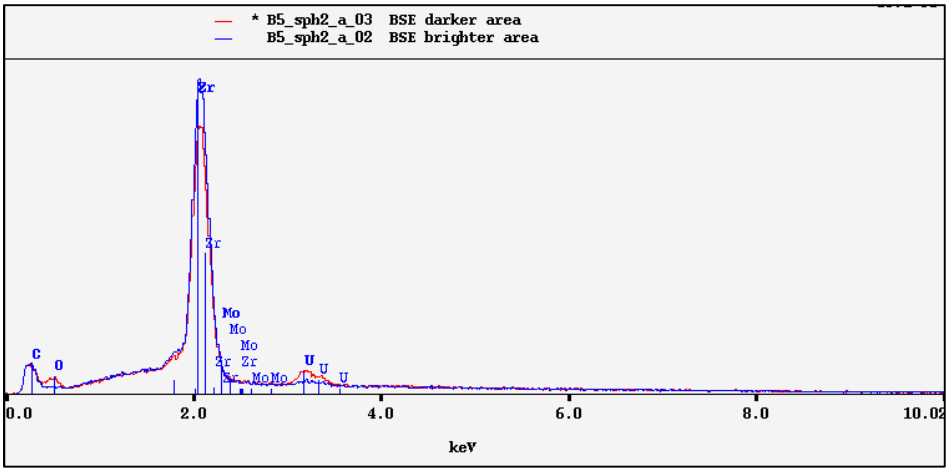

Figure 4-46. Energy dispersive X-ray spectroscopy data from B5 coating composition regions.

The interface of the polished cross-section of two coated spheres shown in Figure 4-47 was chosen for analysis because the observed coatings were suspected to be representative of the true thickness. This assumption was made because the touching particles were similar sizes, indicating that the cross-sections shown are likely near the middle of the spheres. A thin, dark region was observed around the edge of the spheres, suggesting the presence of a coating. The composition was analyzed using X-ray maps for suspected elements, shown in Figure 4-48.

The zirconium map confirmed that the layer corresponded to a zirconium-based coating. Oxygen was present throughout the coating. The oxygen rich layer appeared to be thicker than the zirconium layer and to overlap with the bulk material, once again indicating the growth of a U-Mo oxide layer prior to zirconium deposition. Oxygen also appears at a higher concentration, shown by the brighter layer, near the surface of the bulk material. The appearance of a brighter oxygen layer on one of the particle edges was most likely caused by rounding effects of polishing tilting the edge of the sphere toward the oxygen spectrometer and enhancing the signal.

The same phenomenon was observed in the nitrogen map, however it enabled a layer containing nitrogen corresponding to the zirconium layer to be distinguished from noise in the dense bulk material. The thickness of the coatings was measured using the

zirconium X-ray map and comparing it to the shown scale bar. Measurements were made across the length of fifteen normal lines corresponding to the thickness of the zirconium layers on the two particles. The resulting average thickness was determined to be 1.5 ± 0.3 µm.

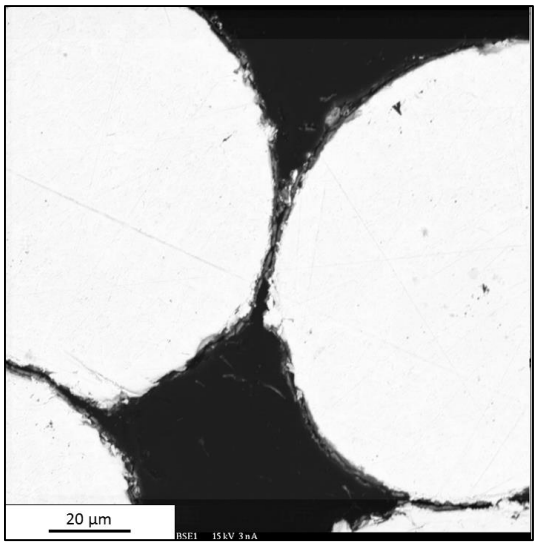

Figure 4-47. Backscattered electron image of B5 coated sphere cross-section.

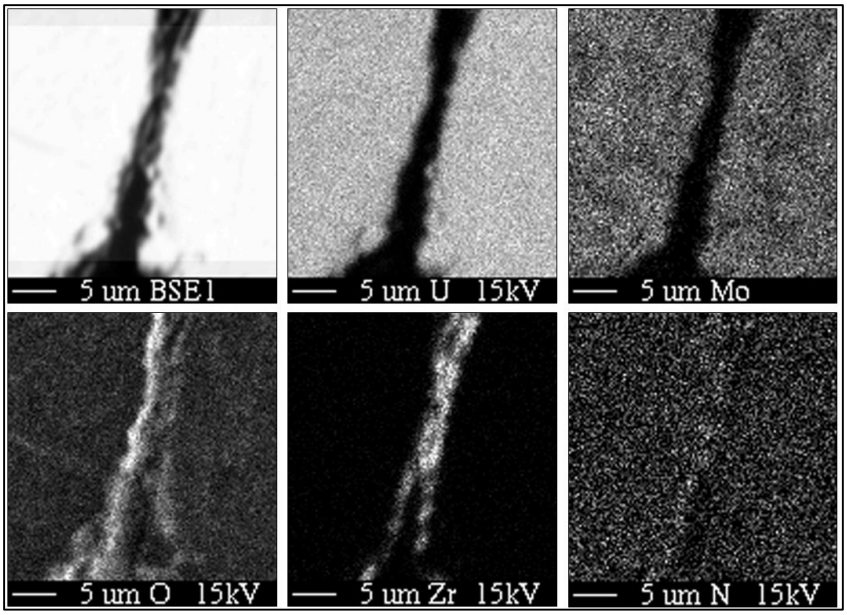

Figure 4-48. X-ray maps of B5 polished spheres interface.

4.3.3 Description of Results from Time-Varying Experiments

The following experiments were performed to study the effects of the duration of substrate exposure to the flowing gas precursor. Results from deposition times of 6 days (T6) and 8 days (T8) will be described in the following sections.

4.3.3.1 Characterization of Results from Experiment T6.

In experiment T6, the precursor was reloaded following 4 days of operation. Two days following reloading, a clog developed at the needle valve between the bubbler and reaction vessel and consequently shut down on Day 6. Following the experiment, the reaction vessel had a dark coating, shown in Figure 4-49, corresponding to the entire heated region of the reaction vessel. Unlike those seen in previous experiments, gold colored flakes appeared to have deposited in the coating.

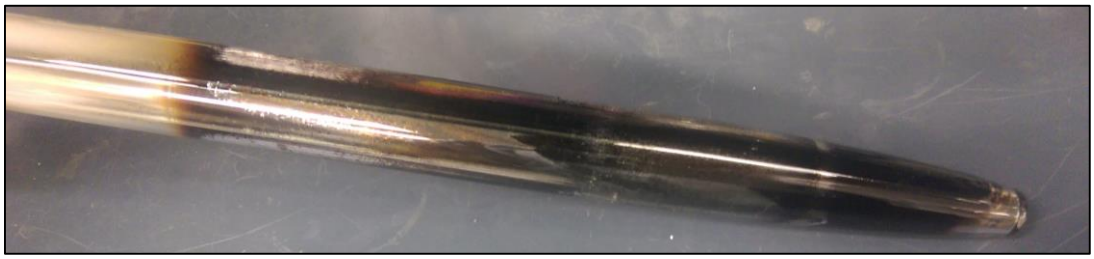

Figure 4-49. Experiment T6 coated reaction vessel.

The coated sphere surfaces were examined by BSE as shown in Figure 4-50. The images show a small portion of uncoated spheres, observed by the brighter surfaces. This was likely caused by a small stagnant region at the bottom of the reaction vessel as previously discussed. The rest of the spheres have similar surface textures, as observed by BSE imaging. The spheres exhibit a rough surface texture dissimilar to those observed in the baseline experiments. The EDS spectra of different particles in Figure 4-51 show consistency of the coating between particles. A small uranium peak was observed. The detection of this signal is likely related to the rough surface texture as the beam may be more able to penetrate through the coating to the bulk material.

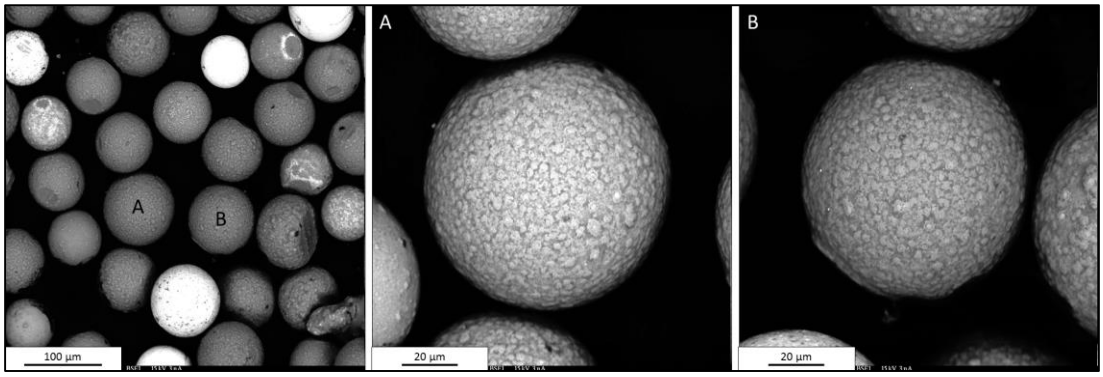

Figure 4-50. Backscattered electron images of T6 coated sphere surfaces.

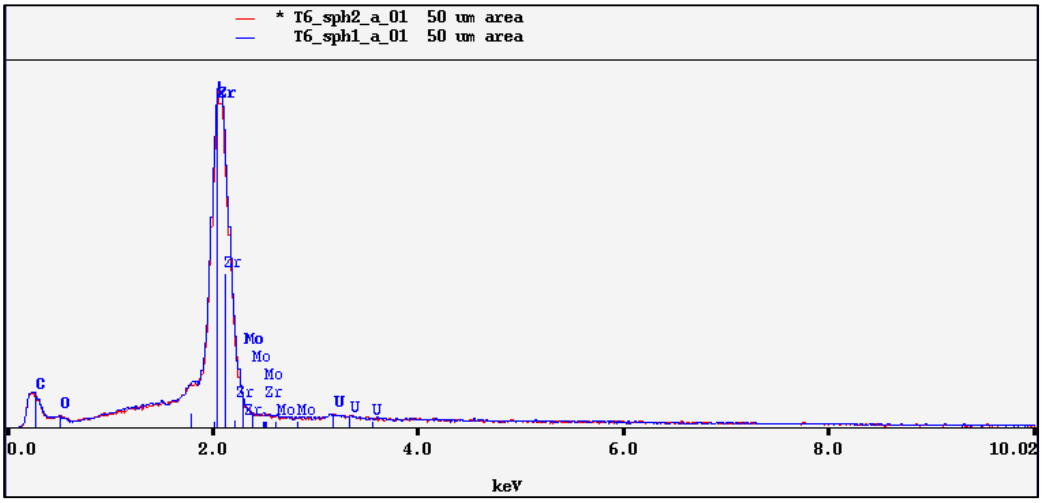

Figure 4-51. Energy dispersive X-ray spectroscopy data from T6 coated sphere surfaces.

The polished sphere cross-sections are shown in Figure 4-52. A dark layer of consistent thickness was observed around the surfaces of most of the population. The particles shown were selected for further analysis because they were suspected to be closely representative of the true coating thickness. The X-ray maps of one of the interfaces are shown in Figure 4-53. The polishing of the sample likely rounded the edges of spheres, causing some of the edges to tilt towards or away from a certain spectrometer. This caused the disparity in the intensity of the signal observed from opposing edges despite similar compositions. The thickness of the coating was estimated by measuring

the width zirconium layer in the X-ray map and comparing to the length of the shown scale bar. The thickness of the zirconium layer was measured at fifteen points across the surfaces of the spheres, resulting in an average thickness measurement of 2.4 ± 0.4 µm.

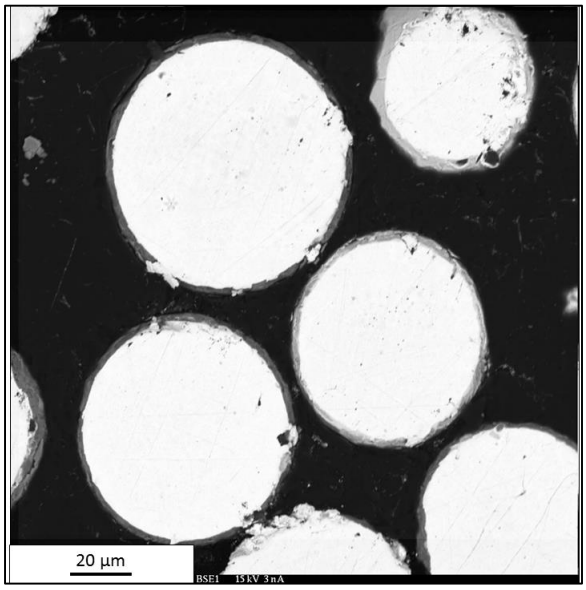

Figure 4-52. Backscattered electron image of T6 polished sphere cross-sections.

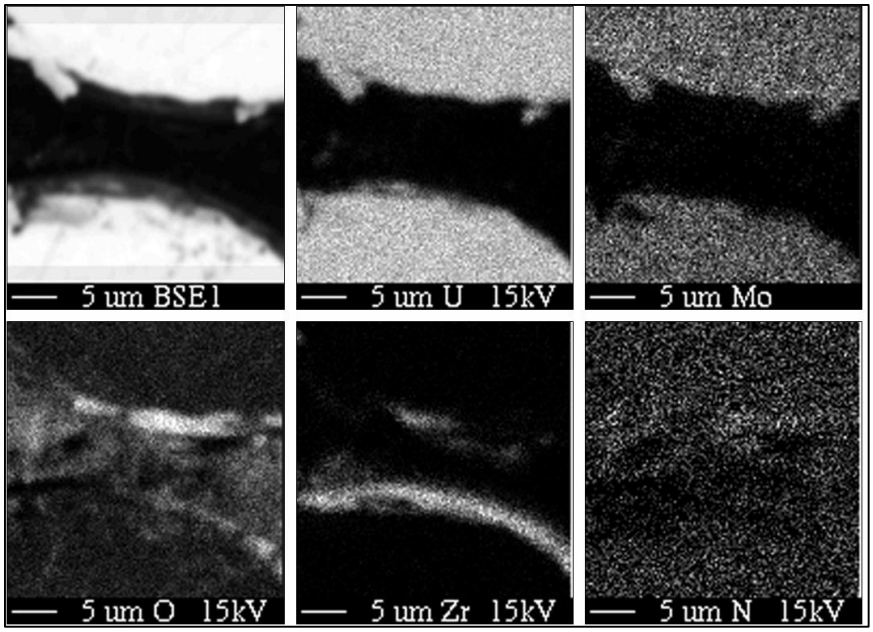

Figure 4-53. X-ray maps of T6 polished sphere interface.

4.3.3.2 Characterization of Results from Experiment T8

Experiment T8 was performed over 8 days with 10 g of TDMAZ loaded into the bubbler at the beginning of the experiment. The development of flow restrictions was not observed during operation. The reaction vessel is shown in Figure 4-54 with a dark, non-transparent coating.

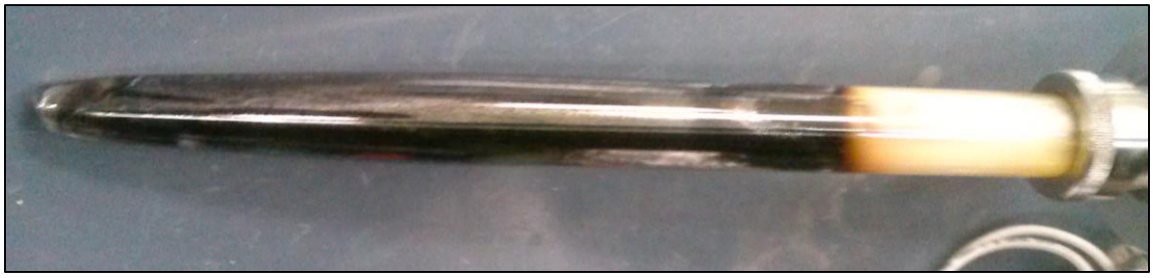

Figure 4-54. Experiment T8 coated reaction vessel.

The coated particle surfaces were observed using BSE imaging. The surfaces, shown in Figure 4-55, of the entire population exhibit a smooth texture and appear to be of similar composition. This was confirmed in the EDS spectra of multiple particles, shown in Figure 4-56, that show similar strong zirconium and oxygen peaks. Negligible uranium peaks were observed, suggesting that a full, even coating was produced.

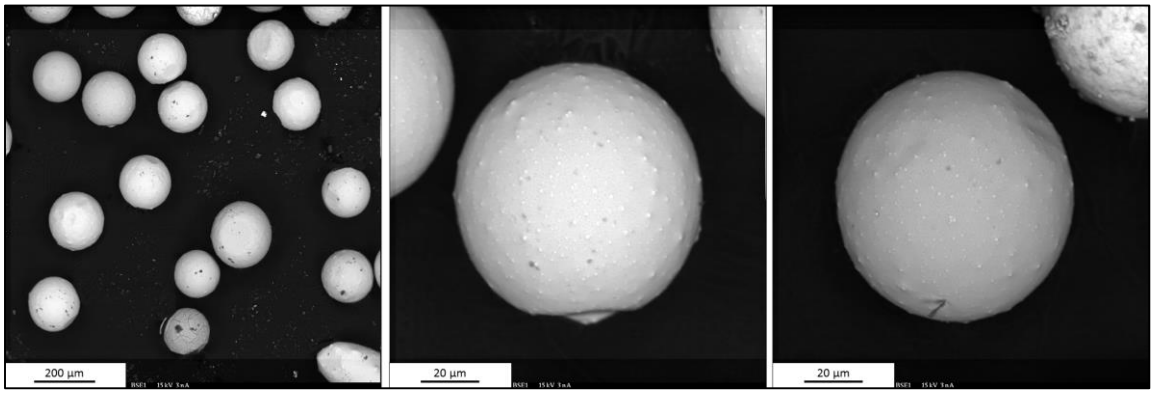

Figure 4-55. Backscattered electron images of T8 coated sphere surfaces.

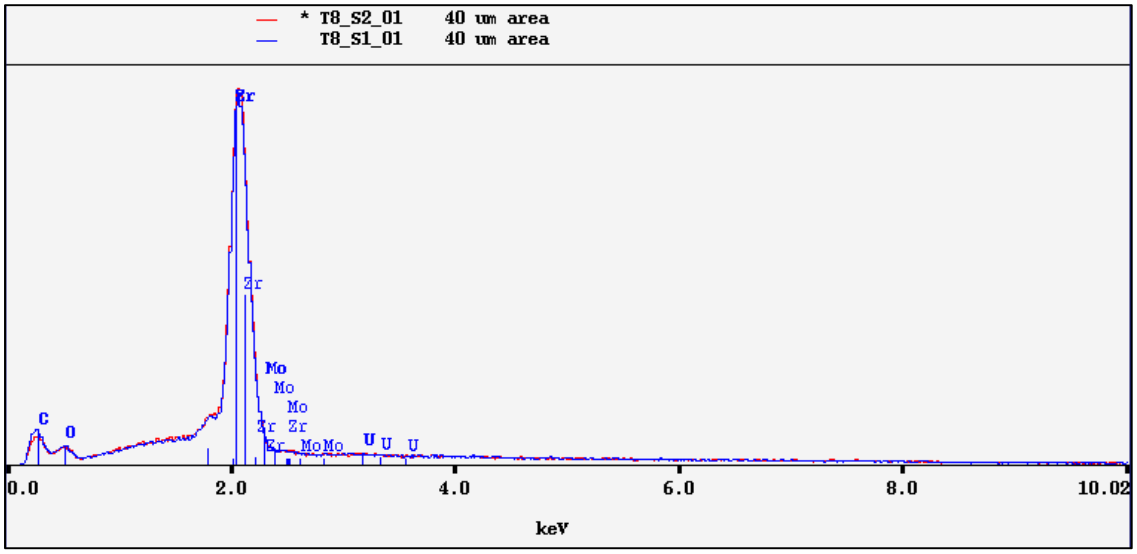

Figure 4-56. Energy dispersive X-ray spectroscopy data from T8 coated sphere surfaces.

The polished coated particles are shown in Figure 4-57. Two spheres of similar sizes in contact were found so that the analyzed cross-section would be near the mid-plane of the particle and representative of the true coating thickness. The interface shown was therefore selected for further analysis. The dark ring around the surface of the sphere was suspected to be the zirconium based coating, which was confirmed using X-ray mapping of the interface, shown in Figure 4-58. There was slight rounding of the particle edges observed by enhanced oxygen and nitrogen signal on one edge, but the contact of the spheres reduced the effects. This enabled a nitrogen rich layer to be distinguished from noise. The thickness of the oxygen rich layer appeared at the same thickness and location of the zirconium layer, suggesting that a U-Mo oxide layer was not grown during the process. The thickness of the coating was estimated by measuring the width of the zirconium layer shown in the X-ray map across fifteen sections and comparing it to the length corresponding scale bar. Assuming the coatings span the entire measured region as the image suggests, the average coating thickness was determined to be 2.4 ± 0.4 μm thick.

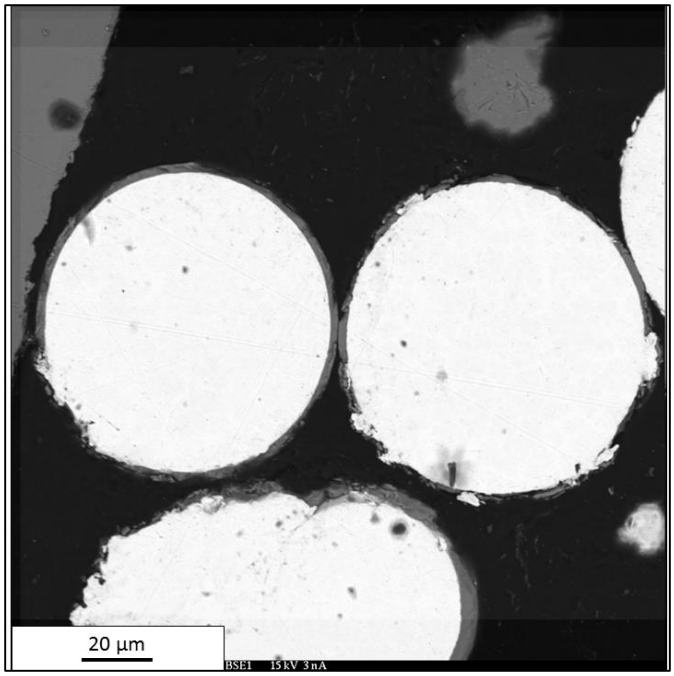

Figure 4-57. Backscattered electron image of T8 polished sphere interface.

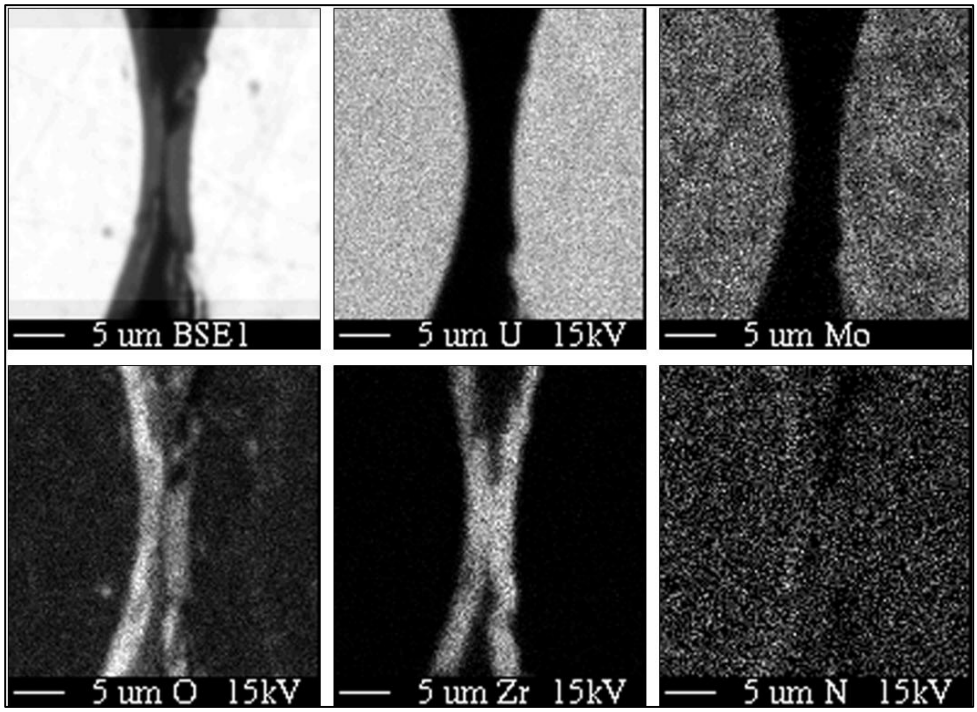

Figure 4-58. X-ray maps of T8 polished sphere interface.

A WDS stage scan for known elements, including nitrogen, zirconium, and uranium was performed to support the estimations made from the X-ray maps. Measurements were taken at 1 µm increments between the bulk material of two particles, crossing the sphere interface. Figure 4-59 shows results of the scan at the respective location. A zirconium rich region in between the bulk material of the two particles was present. The oxygen signal was observed to increase corresponding to the zirconium rich region but was level throughout regions containing uranium. Therefore the particles do not appear to have a distinct U-Mo oxide layer present, unlike those observed in previous experiments. A small rise in the nitrogen signal was also observed throughout the same region. This region spanning from points 6 to 10 consisted of the coatings of the two particles. Therefore, each particle had about a 2 µm thick coating of zirconium, oxygen, and nitrogen.

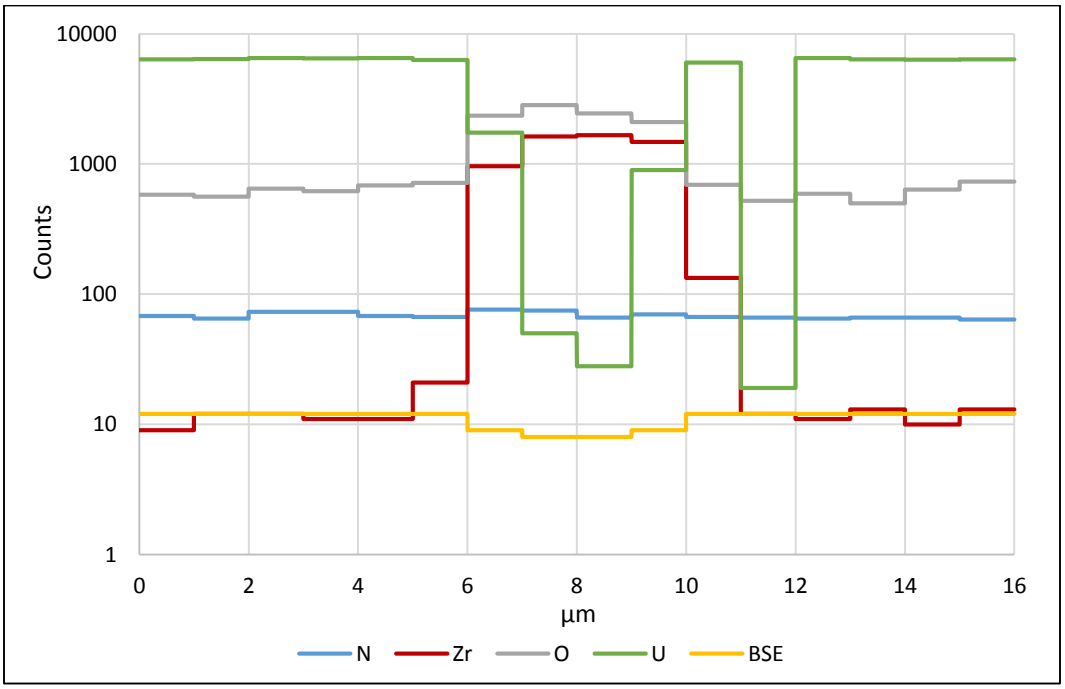

Figure 4-59. Wavelength dispersive spectroscopy scan of across the T8 coated sphere interface.

4.3.3.3 Characterization of Coatings by Wavelength Dispersive Spectroscopy

The WDS zirconium signal was similar for each experiment, as shown in Figure 4-60. This was expected since each coating analyzed consisted of thickness greater than the beam penetration depth of 1 µm. This does show that the zirconium concentration was not dependent on coating thickness and was consistent throughout the set of experiments.

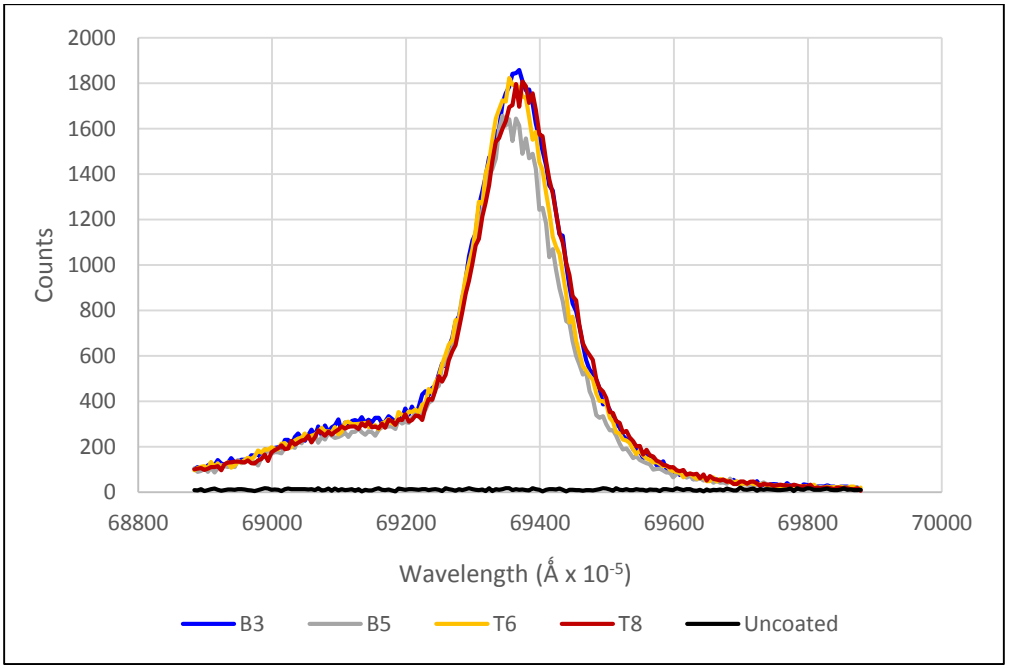

Figure 4-60. Wavelength dispersive X-ray spectroscopy data comparing the zirconium content in coatings produced for the deposition time study.

The nitrogen and oxygen signals from each of the experiments is shown in Figure 4-61 and Figure 4-62, respectively. Both experienced a distinct increase from uncoated material showing that both are present in the coating, but the ratios of elements cannot be determined from this qualitative analysis. Similar trends in the relationship between nitrogen and oxygen content were observed as noted in previous experiments as they again appear to be competitive deposition processes. A trend in coating thickness was not observed. Although the thickest coating yielded the highest nitrogen signal, the extent of oxidation seemed to vary randomly between the experiments.

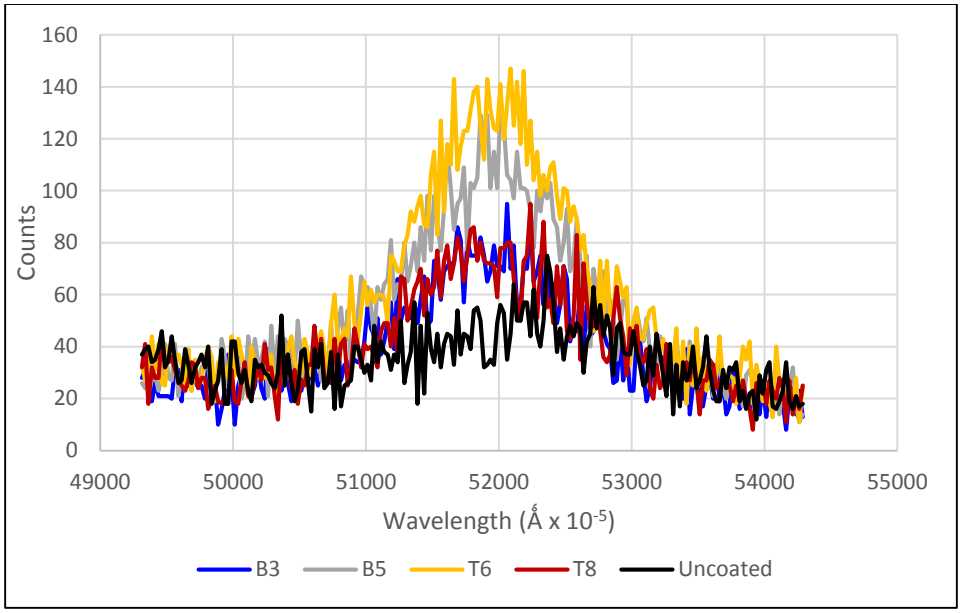

Figure 4-61. Wavelength dispersive X-ray spectroscopy data comparing the nitrogen content in coatings produced for the deposition time study.

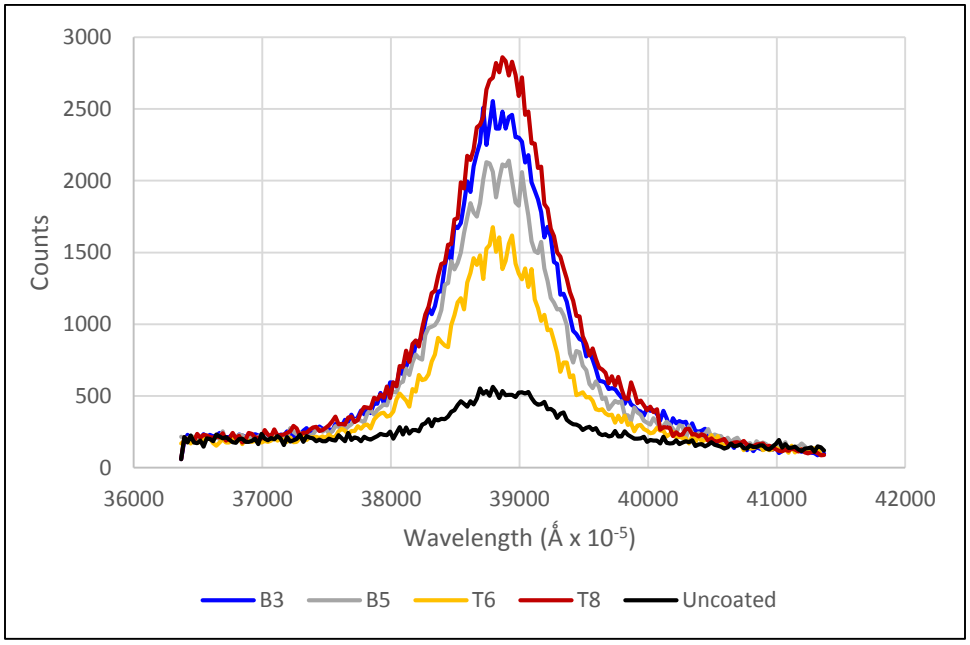

Figure 4-62. Wavelength dispersive X-ray spectroscopy data comparing the oxygen content in coatings produced for the deposition time study.

4.3.4 Description of Results from Flow Rate-Varying Experiments

The following experiments were analyzed to discuss the effects of the precursor carrier gas flow rate on the deposited coating thickness. Results from experiments utilizing a precursor carrier gas flow rate of 200 mL/min (F200) and 300 mL/min (F300) will be discussed along with comparisons to the baseline experiments will be discussed in the following sections.

4.3.4.1 Characterization of Results from Experiment F200

The experiment utilizing a precursor carrier gas flow rate of 200 mL/min produced a dark coating on the reaction vessel glass, shown in Figure 4-63 similar to that seen in previous experiments. The coated microsphere surfaces, shown in Figure 4-64, appear consistent across the population with an exception of some uncoated particles that resulted from a stagnant zone in the reaction vessel. There was some 3D texture observed on the surfaces, but did not seem to correspond to partially coated areas since a uranium signal was not detected and observed in the EDS spectra of the sphere surfaces in Figure 4-65.

Figure 4-63. Reaction vessel coated in experiment F200.

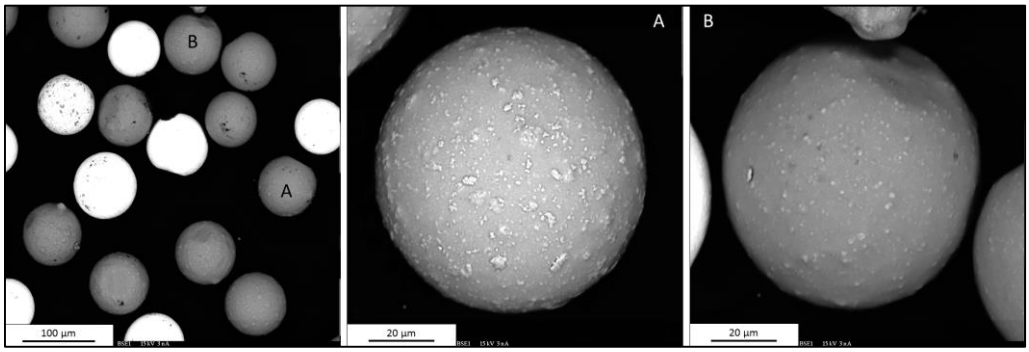

Figure 4-64. Backscattered electron images of F200 particle surfaces.

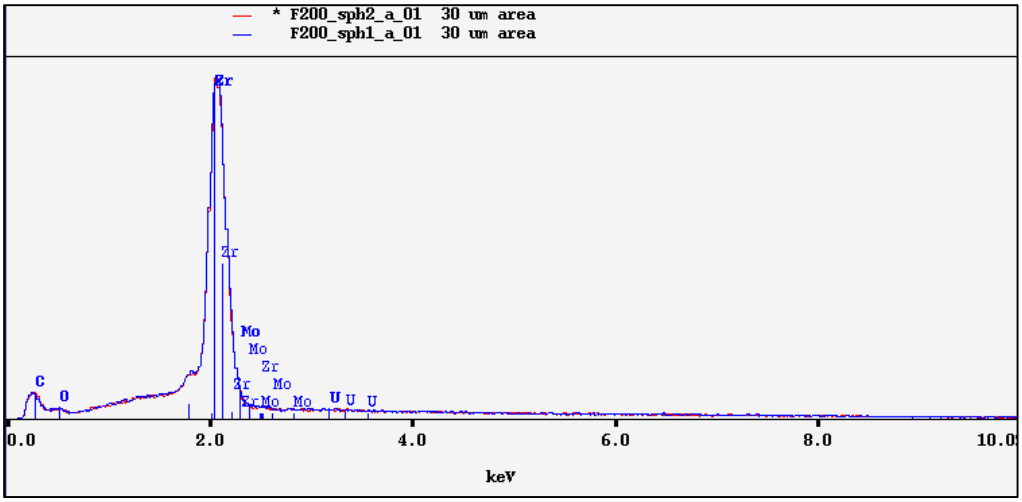

Figure 4-65. Energy dispersive X-ray spectroscopy data from F200 coated particle surfaces.

The polished sphere cross-sections revealed coatings with smooth surfaces and little break away of the surface from the bulk particle. The dark layer, usually corresponding to the particle coating, is observed in Figure 4-66 with consistent thickness throughout the sample. The particles shown were selected for further analysis based on the similar sizes of the spheres in contact. The X-ray maps of one of the contacting interface are shown in Figure 4-67.

The edge exhibits little rounding from polishing as the intensity of the signals from both edges are similar. Nitrogen was observable in the coatings on both particle surfaces. The thickness of the oxygen rich layer appeared at the same thickness and location of the zirconium layer, suggesting that a U-Mo oxide layer was not grown during the process. The thickness of the coatings was estimated using the scale of the X-ray map. Measurements were made across the length of fifteen normal lines corresponding to the thickness of the zirconium layers on the two particles. The resulting average thickness was determined to be 2.2 ± 0.3 µm.

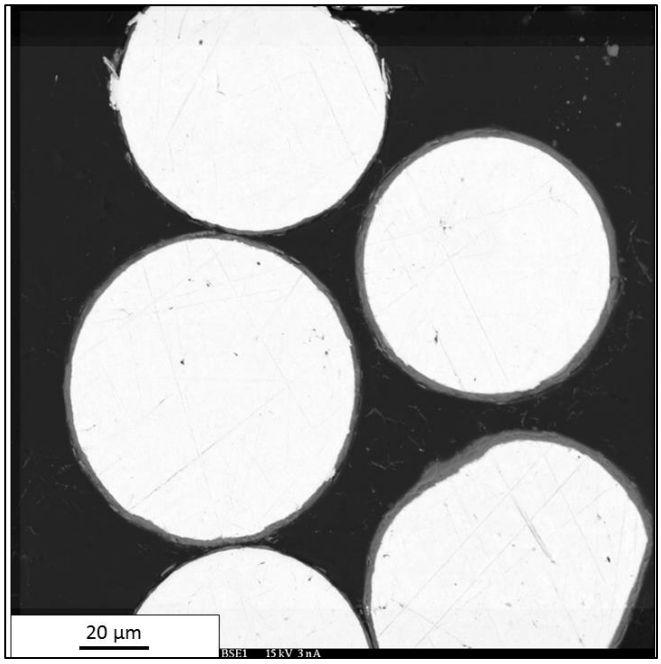

Figure 4-66. Backscattered electron image of F200 polished sphere cross-sections.

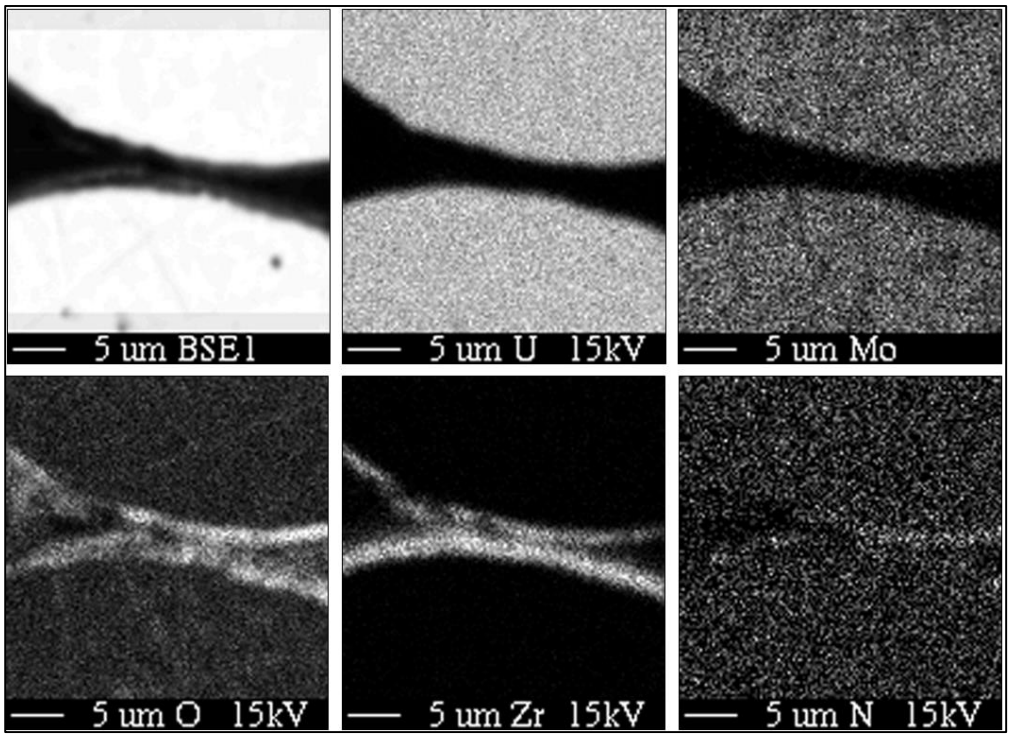

Figure 4-67. X-ray maps of F200 polished sphere interface.

4.3.4.2 Characterization of Results from Experiment F300

The experiment utilizing a precursor carrier gas flow rate of 300 mL/min produced a dark coating on the reaction vessel glass, shown in Figure 4-68. Gold flakes were visually observed throughout the coating. Unlike previous experiments, the coating did not appear along the entire length of the heated wall.

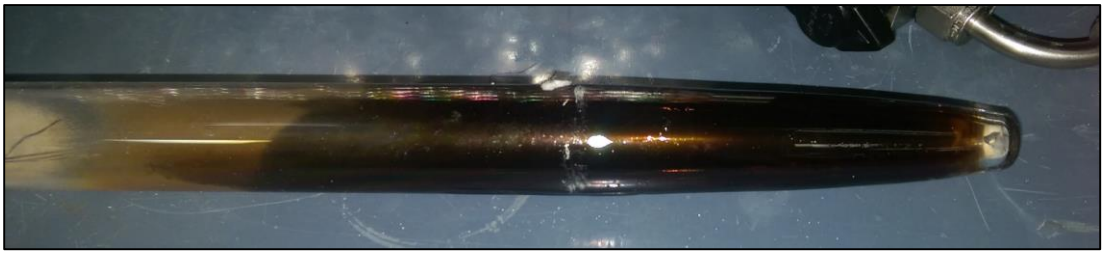

Figure 4-68. Reaction vessel coated in experiment F300.

The BSE images of the coated sphere surfaces once again provided evidence of a stagnant zone in the reaction vessel. The variety of surfaces textures were observed as shown in Figure 4-69. However, the different textures do not appear to correspond with different coating structure as evident by the similar EDS spectra of the two particles shown in Figure 4-70. Both surface textures yielded significant uranium peaks, suggesting a thin partial, or porous coating.

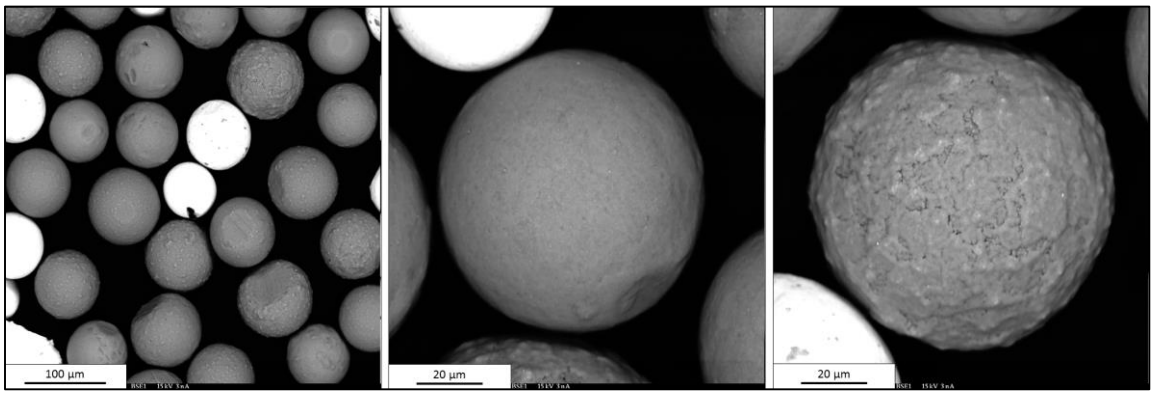

Figure 4-69. Backscattered electron images of F300 coated sphere surfaces.

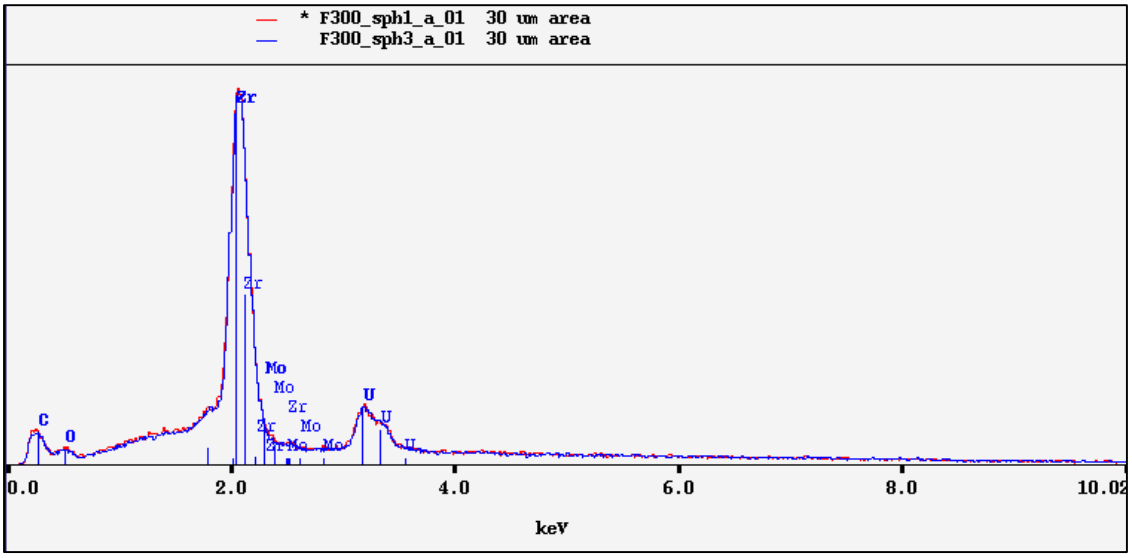

Figure 4-70. Energy dispersive X-ray spectroscopy data from F300 coated sphere surfaces.

The cross-sections appeared rough and cracked in the BSE images as shown in Figure 4-71. The darker coating layer may be observed at the surface of the sphere, but does not appear to cover the entire surface. X-ray maps, shown in Figure 4-72, were collected at the sphere interface where the coating appears even. The region corresponding to the suspected coating once again contained zirconium, oxygen, and nitrogen. Rounding effects of polishing were observed in the X-ray maps by the enhanced signals on edges tilting towards a corresponding spectrometer. The thickness of the coatings was estimated using the scale of the X-ray map. Measurements were made across the length of fifteen normal lines corresponding to the thickness of the zirconium layers on the particles. Assuming that this layer corresponds to the thickness of the coating, the average thickness was determined to be 2.1 ± 0.4 µm.

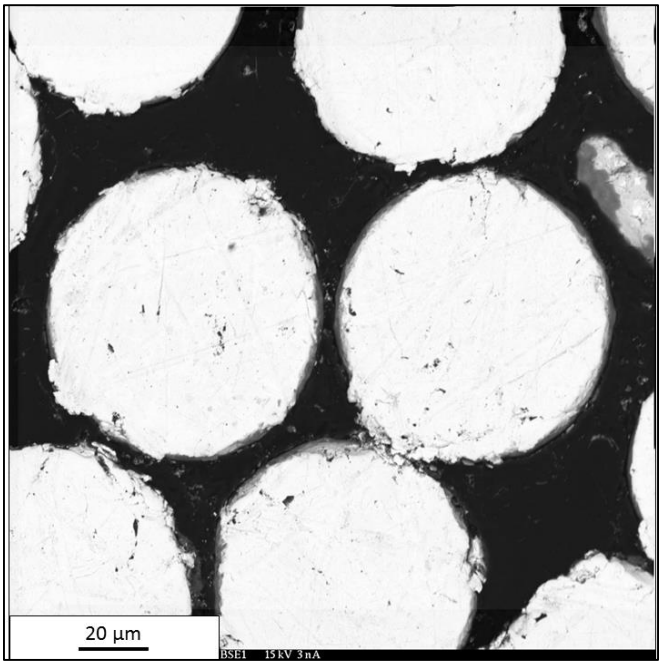

Figure 4-71. Backscattered electron image of F300 polished sphere cross-sections.

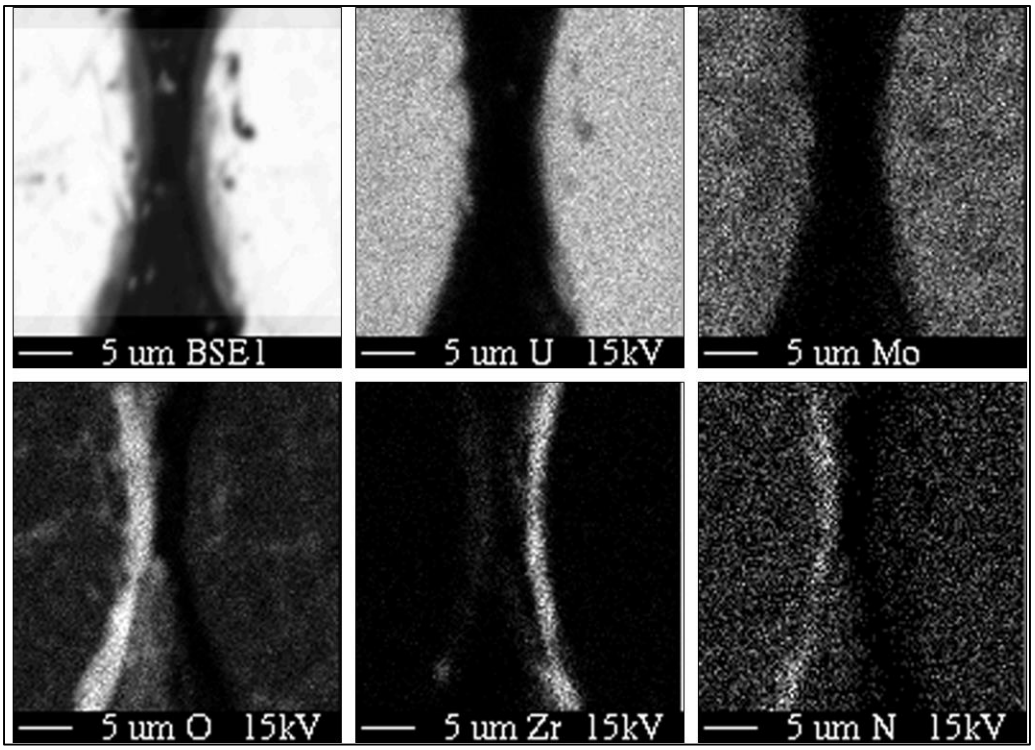

Figure 4-72. X-ray maps of F300 polished sphere edges.

4.3.4.3 Characterization of Coatings by Wavelength Dispersive Spectroscopy

The zirconium signal was similar for the majority of the experiments, as shown in Figure 4-73. However, the zirconium signal intensity for experiment F300 was less than other experiments, supporting the previous evidence of an incomplete coating. The nitrogen and oxygen signals from each of the experiments is shown in Figure 4-74 and Figure 4-75, respectively. The nitrogen and oxygen content again appear to be indirectly related. Experiment F300 was again observed as an outlier as both large oxygen and nitrogen peaks were observed. This could be caused by the partial coating causing larger amounts of oxygen to be detected from an underlying oxide layer.

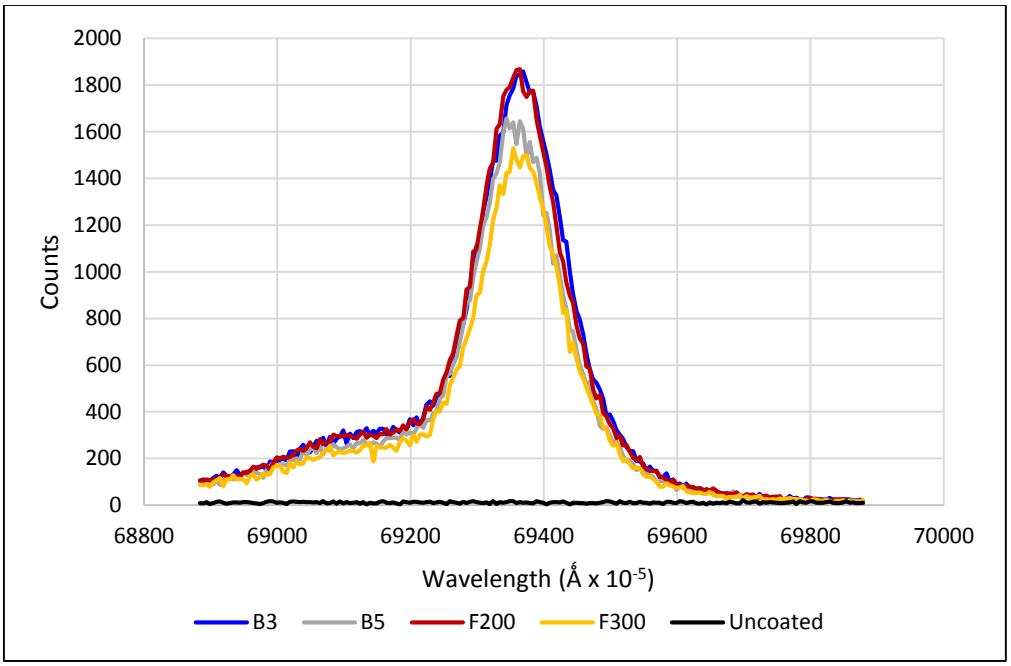

Figure 4-73. Wavelength dispersive X-ray spectroscopy data comparing the zirconium content in coatings produced for the flow rate study.

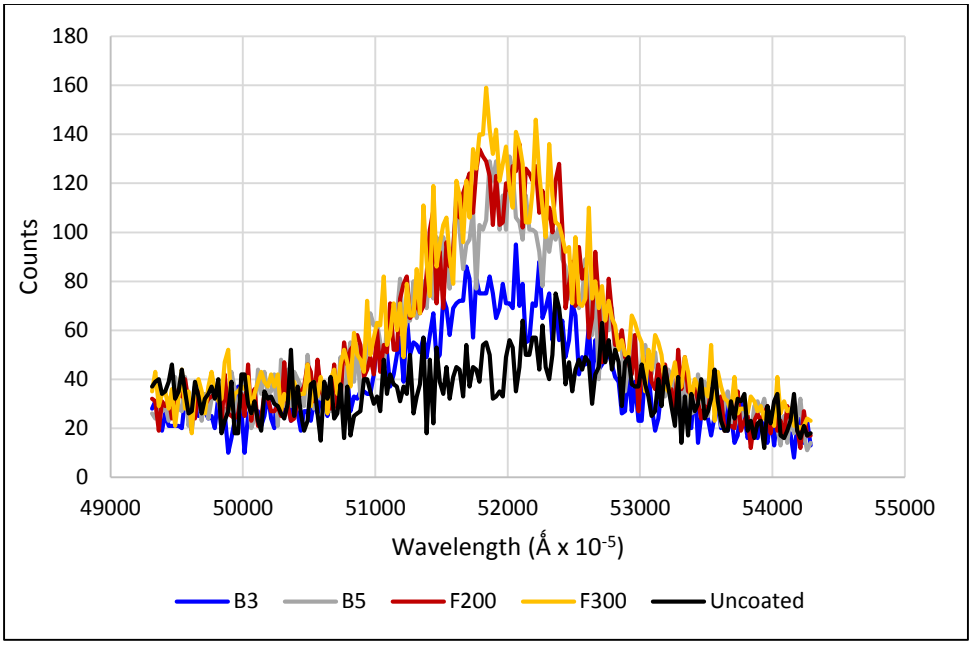

Figure 4-74. Wavelength dispersive X-ray spectroscopy data comparing the nitrogen content in coatings produced for the flow rate study.

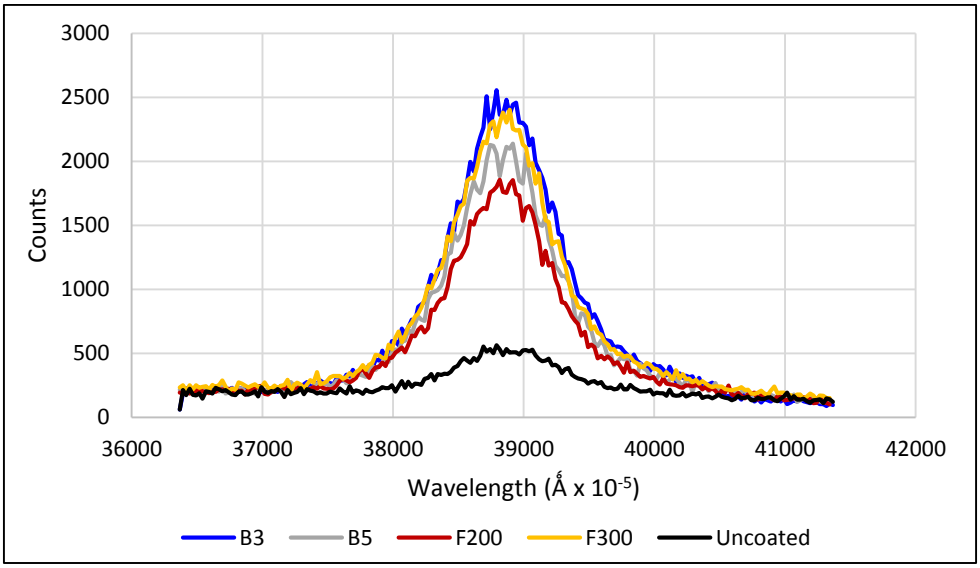

Figure 4-75. Wavelength dispersive X-ray spectroscopy data comparing the oxygen content in coatings produced for the flow rate study.

4.3.5 Observation of Coating Oxidation

Samples from experiments B5, T6, F200, and F300 were prepared for surface analysis to examine the oxidation of the coating post deposition after extended storage in a glovebox. The first set of samples were prepared as described in Section 3, involving exposing the particles to air during sample preparation and transfer. The second set was prepared by mounting the loose spheres on the carbon tape stubs inside the glovebox. Since this sample preparation was performed inside the glovebox, the particles were not exposed to air until immediately transferred to the microprobe lab and carbon coated, limiting the air exposure.

The principal difference in the surface analysis of the sets of samples was the WDS oxygen signal. The oxygen peaks are shown in Figure 4-76, in which each experiment is represented by a different color and the darker of each corresponding to the samples prepared inside the glovebox (g). This graph shows that for each of the experiments analyzed, the oxygen peak was significantly lower for samples prepared inside the glovebox. The extent to which the samples were oxidized during sample preparation was observed by calculating the difference in the peak intensities from each experiment. Upon further inspection, the increase in the oxygen signal for samples prepared in air versus those prepared in the inert atmosphere, described in Table 4-7, was similar for three out of the four experiments analyzed. There was a much larger change in samples from experiment B5. This is likely due to the presence of thinner particle. Overall, these results show that the particle surfaces will oxidize to some degree when exposed to air even after coating and storage in an inert atmosphere.

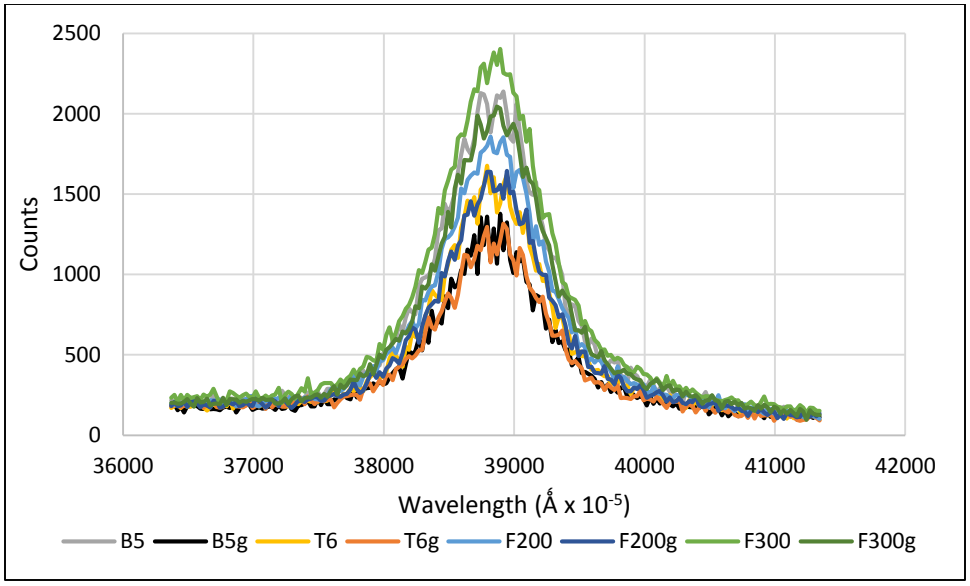

Figure 4-76. Oxygen content comparison for different sample preparation method using wavelength dispersive X-ray spectroscopy. Samples prepared inside the glovebox are denoted with a g in the experiment label.

Table 4-7. Estimated changes in oxygen peak intensity and coating thicknesss.

Experiment	Δ Peak Intensity	Estimated Coating Thickness (µm)
F200	213	2.0
F300	300	2.5
B5	761	1.5
T6	360	3.2

5. DISCUSSION OF RESULTS

This chapter discusses the experimental results described in Chapter 4. The following sections discuss the improvements made to the system design (Section 5.1) as well as the comparison of the data collected from the series of parametric studies (Section 5.2). Section 5.3 discusses the observations made relating to the characteristics of the coatings produced using the FB-CVD system and conclusions that were drawn from the experimental results.

5.1 Discussion of System and Process Design Improvements

As described in Section 4.2, various modifications to the lab-scale FB-CVD system were made during this project. The redesign of the reaction vessel head using NPT and O-ring fittings improved the vacuum seal, which resulted in more effective precursor transport. The improved precursor transport resulted in the development of flow restrictions (i.e. clogging), especially at needle valves and heated reduction joints. Mixing the two flow paths prior to entering the reaction vessel eliminated the need for the heated reduction joints and helped to open the flow paths.

Tapering the bottom of the reaction vessel improved fluidization of the particle bed, especially after increasing the diameter of the inlet tubes. The tapered bottom increased the expansion of the particle bed, even at lower flow rates. Experiments with a tapered vessel showed consistent coatings on the powder. The expanded particle bed was believed to minimize intermediate zones that produced thinner coatings that were observed in early experiments. This design was susceptible to a small stagnant region at the bottom of the vessel, and a further redesign is recommended if the design is pursued in the future. In some cases, the bottom of the reaction vessel was too narrow for the inlet tube to extend far enough to fluidize particles at the bottom of the bed. A wider round bottom decreased this effect, but misalignment of the inlet tube and the glass tube causing contact of the walls distorted the expansion of the bottom of the particle bed.

Over-fluidization was an obstacle in system startup regardless of the shape of the reaction vessel. Significant material was lost upon opening the flow between the bubbler and reaction vessel. Slowly ramping up the precursor carrier gas flow rate did not appear to have an effect. Including a needle valve between the bubbler and reaction vessel to restrict the gas flow while slowly opening the flow path reduced the material loss, but did not eliminate the issue. Elimination of the reducing joints along the inlet tube also reduced material loss as over-fluidized particles in the reaction vessel were able to return to the particle bed rather than settling on the joints.

5.2 Comparison of Data from Parametric Studies

The data collected from the sets of experiments performed by varying the duration of substrate exposure to the chemical precursor (Section 4.3.3) and varying the gas flow rates through the system (Section 4.3.4) were compared to the baseline results (Section 4.3.2) and the characteristics of the uncoated material (Section 4.3.1). These comparisons and observed effects are discussed for the time-varying studies in Section 5.2.1, and the flow rate-varying studies are discussed in Section 5.2.2.

5.2.1 Comparison of Data from Time-Varying Studies

The conditions and estimated coating thicknesses for the experiments in the deposition rate study are described in Table 5-1. The table describes the amount of precursor used during the experiment measured by the weight of the bubbler and its contents before and after each loading. The average precursor transport rate was determined from the amount of precursor used and the run time.

Table 5-1. Summary of time-varying experiments.

	Baseline 3	**Baseline 5**	**T6**	**T8**
Run Time (days)	1.5	2	4, 2	8
Precursor Used (g)	3.0	1.2	3.7, 1.8	6.7
Apparent Transport Rate (g/day)	1.5	0.6	0.9, 0.9	0.8
Particle Diameter (μm)	90-106	90-106	63-90	63-90
Estimated Coating Thickness (μm)	2.1 ± 0.5	1.5 ± 0.3	2.4 ± 0.4	2.4 ± 0.4

The deposition time allotted for each experiment did not appear to have a distinct impact on the coating thickness. Although longer operation times may have a small effect on the coating produced, the various run times did not produce significantly different coating thicknesses within the error of the measurement technique. This suggests that the overall deposition time is not the dominant factor affecting coating deposition and corresponding thickness.

It was also observed that experiments B3 and T6 had higher apparent precursor transport rates, described as the total mass loss from the bubbler averaged over the experiment duration, than experiments B5 and T8. There may exist a relation between precursor transport rate and coating thickness, but a direct trend cannot be confirmed in these set of experiments because the variable conditions were not appropriate to examine these effects. It was also possible that the rate of precursor transport was affected later in the experiment by the decomposition of TDMAZ to a non-volatile species within the bubbler after extended exposure to a higher temperature. However, the total mass loss and corresponding apparent transport rate of the precursor did not seem to vary based from the operation time per precursor loading. This was most distinctly observed during experiment T6, in which the apparent precursor transport rate was the same for the loadings in operation over different amounts of time. Therefore, it appears that precursor transport occurred throughout the experiment.

Since the thickness of the coatings were similar in each experiment despite extended duration times, it was suspected that the majority of the coating occurred near

the beginning of the experiment. This was also evident from the development of the dark coating on the reaction vessel that was observed to develop within the first 24 hours of the CVD process. It was suspected that coating deposition was impeded after an extended period of time by decomposition of the precursor. However, experiment T6 did not produce a distinctly thicker coating than experiment T8, despite the reloading of fresh precursor during the experiment. Therefore, the development of the coating in the later stages of the deposition process was not observed to have been affected by possible decomposition of the precursor.

5.2.2 Comparison of Data from Flow Rate-Varying Studies

The conditions and estimated coating thicknesses for the experiments in the flow rate study are re-presented in Table 5-2. The table describes the amount of precursor used during the experiment measured by the weight of the bubbler and its contents before and after each loading. The average precursor transport rate was determined from the amount of precursor used and the run time for each loading.

Based on this set of experiments, the precursor carrier gas flow rate does not appear to have an effect on the precursor transport rate. As a result, the coating thickness was not notably affected by the flow rate. However, the coatings produced in experiment F200 were the most consistent and even across the surface, suggesting that this may be the most favorable combination of flow rates of those examined. Additional tests would be necessary to confirm these results and to identify the optimum flow rates.

Table 5-2. Summary of flow rate-varying experiments.

	Baseline 3	**Baseline 5**	**F200**	**F300**
Fluidization Flow Rate (L/min)	0.5	0.5	0.4	0.3
Precursor Carrier Gas Flow Rate (mL/min)	100	100	200	300
Precursor Used (g)	3.0	1.2	1.2	2.0
Apparent transport rate (g/day)	1.5	0.6	0.6	1.0
Particle Diameter (μm)	90-106	90-106	63-90	63-90
Estimated Coating Thickness (μm)	2.1 ± 0.5	1.5 ± 0.3	2.2 ± 0.3	2.1 ± 0.4

5.3 Discussion of Zr-based Coatings Formed by FB-CVD

The system produced much variability between the coatings produced in each experiment. The reproducibility of the results and performance of the system improved in later experiments with improved techniques and equipment. This section discusses observations relating to the characteristics of the coatings produced.

5.3.1 Coating Thickness

The lab-scale FB-CVD inverted reactor showed the capability to produce coatings of at least 1 μm thick in early experiments, most notably in Exp. 5. However, equipment faults prompted modifications (see Section 4.2 and 5.1) to improve the performance of the system. Following these improvements, coatings of at least 1 μm in thickness were consistently produced. The modified system also enabled a more efficient process, as coatings of 1-2 μm thick were consistently produced within 2 days of deposition. Trends in the coating thickness relating to the duration and deposition and process gas flow rates were not observed.

5.3.2 Coating Composition

The coating was identified in each experiment by the intensity of detected zirconium and was easily observable by EDS, WDS, and X-ray mapping. Oxygen and

nitrogen also appeared present in the coatings. Gold flakes were visually observed in the coatings on the reaction vessels from experiments T6 and F300, which showed the highest nitrogen content. Nitrogen was often challenging to detect due to characteristics of the measurement techniques, and oxygen was observed at higher intensities. However, in the quantitative analysis performed in Exp. 5, nitrogen and oxygen appeared present in similar quantities as measured in atom percent. Although quantitative analysis was not performed on later experiments, nitrogen was often detected via WDS at a similar intensity to that seen in experiment E5.

Since zirconium has a high affinity for oxygen, oxygen impurities were expected in the coating even in a vacuum environment [34]. Higher oxygen intensities were observed in coatings with lower nitrogen content and vice versa. This inverse relationship observed provides evidence that nitrogen and oxygen deposition are competitive processes. From X-ray mapping and WDS analysis of thicker coatings (E5, E12, B5, and F200), oxygen deposition tends to appear more favorable near the bulk material supporting evidence of the formation of the multiple layers observed in the high resolution SE image of experiment E5 coatings (Figure 4-14). This occurrence may be explained by the high oxygen affinity of the refractory metal surface contributing to the chemical potential for oxygen deposition near the surface and decreasing in effect as the coating develops further from the surface of the bulk material. However, the existence of multiple layers was not observed in the coatings produced in every experiment, including T6 and T8. The low resolution of the measurement techniques and variability in oxidation limited the ability study this phenomenon.

The X-ray maps collected for most of the experiments suggested that a significant U-Mo oxide layer was present between the bulk material surface and the zirconium based coating. Since this layer did not appear as distinctly in the uncoated material analyzed, it was concluded that the oxide layer grew during the coating process. The majority of the layer was likely grown prior to coating deposition (i.e. during vessel purging and heating) as the zirconium-based coating was deposited on top of this layer. This suggests that the

source of oxygen observed in the coatings is either the source gas or leaks in the equipment rather than the source material.

The oxygen content within the coatings appeared to vary significantly between experiments in a manner not corresponding to a trend relating to coating thickness. This indicated that either random errors or unpredicted phenomena in the system setup and operation exists in the process that affects the reproducibility of the system and makes it difficult to establish relations. Enabling the withdrawal of samples from various points throughout the experiment would more effectively enable the measurement of characteristics of the deposition process, including the development of layers and changes in deposition rates over different periods of the experiment.

6. SUMMARY AND RECOMMENDATIONS

Under the Reduced Enrichment for Research and Test Reactors program, research reactor fuels have been converted to use low enriched uranium. A uranium-molybdenum (U-Mo) dispersion plate-type fuel is under investigation for the higher performance reactors that require a higher uranium density than can be provided with current fuel technology. Studies of the irradiation behavior of this fuel, described in Section 1.1, showed the development of an interaction layer between U-Mo and the aluminum matrix. A zirconium nitride diffusion barrier was proposed to mitigate the interactions between the fuel particles and dispersion matrix. Fluidized-bed chemical vapor deposition has been studied as a candidate process to create ZrN barrier coatings on U-Mo powders. A lab-scale FB-CVD system was designed by Arrieta to deposit ZrN on U-Mo microspheres using the metalorganic precursor tetrakis(dimethylamino)zirconium [17]. This system was used to develop procedures, study the process variables, and characterize the coatings produced.

The experiments performed in the first phase of this project were performed using constant conditions listed below to reproduce results of the work by Arrieta.

- Reaction temperature = 280 ± 10 °C,
- Precursor temperature = 52 ± 2 °C,
- Transport temperature = 75 ± 5 °C,
- Precursor carrier flow rate = 95 mL/min.

The fluidization flow rate, deposition time, and substrate were adjusted throughout the experiment series, described in Section 3.2 and 4.1, to improve coating and characterization capabilities. The flow of ammonia in alternation with the precursor was tested in the system, but the results showed that the use of ammonia impeded coating deposition (Section 4.1.2). Zirconium-based coatings containing oxygen and nitrogen were produced with a thickness of 1-2 μm after 4 days in experiment 5 (Section 4.1.3). Analysis of polished cross-sections of the particles provided evidence of the formation of

U/Mo oxide, zirconium oxide, and zirconium nitride-dominant surface layers (see Figure 4-14) during the coating process.

A series of mechanical system modifications were made to the system components and tested in the next phase of this project (Section 3.3). The reaction vessel inlet and outlet were adapted with NPT vacuum fittings, and the reaction vessel was designed with a small taper at the bottom of the glass. These modifications were shown to improve precursor transport and fluidization capabilities, resulting in a more consistently coated powder, described in Section 4.2. The consistency of the system performance improved with the modified reaction vessel, and the deposition time required to reach the target thickness was reduced from 4 to 2 days.

The last phase of this project consisted of sets of experiments designed to study process variables including deposition time and precursor carrier gas flow rate. Details of experiment conditions and procedures are described in Section 3.4. The duration of the CVD process was studied by varying the deposition time of the experiments from 2, 6, and 8 days with the mass of precursor loaded as described in Section 3.4.2. The process flow rates were also studied by varying the precursor carrier gas flow rate from 100, 200, and 300 mL/min with the fluidization flow rate adjusted accordingly to maintain a total flow rate of 600 mL/min, described in Section 3.4.3.

Trends corresponding to coating thickness with allotted deposition time and precursor carrier flow rate were not observed from the results presented in Section 4.3 and discussed in Section 5.2. The limited reproducibility of the system made it challenging to identify the factors determining the deposition rate. Coatings of zirconium, nitrogen, and oxygen of 1-2 μm thick coatings of zirconium and nitrogen were consistently produced within 2 days of operation, and did not measurably continue to grow with longer durations. The results continued to show that the zirconium based coatings exhibited higher oxygen content in the inner region of the coating and higher nitrogen content in the outer regions, providing further evidence of the development of oxide- and nitride- dominant layers within the coating. Conditions at which the system performance appeared most effective

are listed below, but these conditions must be further studied to determine the optimum values.

- Reaction temperature = 280 ± 10 °C,
- Precursor temperature = 52 ± 2 °C,
- Transport temperature = 65 ± 5 °C,
- Fluidization flow rate = 400 mL/min,
- Precursor carrier flow rate = 200 mL/min.

The following steps are recommended to improve coating capabilities and better study the deposition process.

1. Install the FB-CVD system inside an inert atmosphere glovebox. This would minimize the oxygen contamination resulting from leaks into the system. It will also eliminate air-exposed powder transfer steps that may result in oxygen exposure in the components when assembling/disassembling the system.

2. Install an additional oxygen getter (zirconium or titanium) prior to inlet of the bubbler and reaction vessel. Since these devices do not require constant replacement, they can be placed at more remote locations within the system and continue to provide supplementary control of oxygen contamination in the case of oxygen trap saturation.

3. Perform analyses using equipment with higher resolution and carbon detection capabilities. This would better identify impurities in the coating and the composition of layers that may develop.

4. Enable partial removal during FB-CVD operation. This would allow samples to be analyzed from different points within a single experiment. Since the reproducibility of the coatings was limited, trends in the deposition process and

causes of differences in the coatings were difficult to ascertain. Analyzing samples from different points throughout the experiment would reduce the test-to-test variations. This would also enable a kinetic study of the coating process, particularly over the first 24 hours in which the majority of the deposition was believed to have occurred, providing a more complete understanding of the deposition process and the development of the coatings.

5. Produce thicker coatings on powders and flat substrates to assess structural properties. If present, multi-layered structures may be more easily observed in thicker coatings. This would enable the characterization of the structure and composition of each of the layers.

REFERENCES

[1] DOE, Highly Enriched Uranium: Striking a Balance, A Historical Report on the United States Highly Enriched Uranium Production, Acquisition, and Utilization Activities from 1945 through September 30, 1996, Washington, DC: U. S. Department of Energy, (2001).

[2] D. M. Wachs, RERTR Fuel Development and Qualification Plan, DE-AC07-05ID14517, Idaho National Laboratory, (2007).

[3] V. P. Sinha, P. V. Hegde, G. J. Prasad, G. K. Dey, and H. S. Kamath, Effect of Molybdenum Addition on Metastability of Cubic γ-Uranium, Journal of Alloys and Compounds, 491, (2010), pp. 753-760.

[4] G. L. Hofman, R. F. Domagala, G. L. Copeland, Irradiation Behavior of Low-Enriched U_6Fe-Al Dispersion Fuel Elements, Journal of Nuclear Materials, 150, (1987), pp. 238-243.

[5] M. K. Meyer, T. C. Weincek, S. L. Hayes, G. L. Hofman, Irradiation Behavior of Low-Enriched U_6Mn-Al Dispersion Fuel Elements, Journal of Nuclear Materials, 278, (2000), pp. 358-363.

[6] M. K. Meyer, G. L. Hofman, S. L. Hayes, C. R. Clark, T. C. Weincek, J. L. Snelgrove, R. V. Strain, K.-H. Kim, Low-Temperature Irradiation Behavior of Uranium-Molybdenum Alloy Dispersion Fuel, Journal of Nuclear Materials, 304, (2002), pp. 221-236.

[7] M. K. Meyer, G. L. Hofman, R. V. Strain, C. R. Clark, J. R. Stuart, Metallographic Analysis of Irradiated RERTR-3 Fuel Test Specimens, Proceedings of the 2000 International Meeting on Reduced Enrichment for Research and Test Reactors, 1-6 October 2000, Las Vegas, Nevada.

[8] G. L. Hofman, M. R. Finlay, Y. S. Kim, Post-Irradiation Analysis of Low Enriched U-Mo/Al Dispersions Fuel Miniplate Tests, RERTR 4 & 5, Proceedings of the 26th International Meeting on Reduced Enrichment for Research and Test Reactors, 7-12 November 2004, Vienna, Austria.

[9] Y. S. Kim, G. L. Hofman, Irradiation Behavior of the Interaction Product of U-Mo Fuel Particle Dispersion in an Al Matrix, Journal of Nuclear Materials, 425, (2012), pp. 181-187.

[10] A. B. Robinson, D. M. Wachs, D. E. Burkes, D. D. Keiser, US RERTR Development Post Irradiation Examination Results, Proceedings of the 2008 International Meeting on Reduced Enrichment for Research and Test Reactors, 5-9 October 2008, Washington, D.C.

[11] F. Huet, V. Marelle, J. Noirot, P. Sacristan, P. Lemoine, Full-Sized Plates Irradiation with High UMo Fuel Loading – Final Results of IRIS 1 Experiment, Proceedings of the 2003 International Meeting on Reduced Enrichment for Research and Test Reactors, 5-10 October 2003, Chicago, Illinois.

[12] A. Leenaers, S, Van den Berghe, E. Koonen, C. Jarousse, F. Huet, M. Trotabas, M. Boyard, S. Guillot, L. Sannen, M. Verwerft, Post-irradiation Examination of Uranium–7 wt% Molybdenum Atomized Dispersion Fuel, Journal of Nuclear Materials, 335, (2004), pp. 39-47.

[13] K. Huang, C. C. Kammerer, D. D. Keiser, Y. H. Sohn, Diffusion Barrier Selection from Refractory Metal (Zr, Mo and Nb) Via Interdiffusion Investigation for U-Mo RERTR Fuel Alloy, Journal of Phase Equilibria and Diffusion, 35, (2014), pp. 146-156.

[14] K. T. Rie, A. Gebauer, Plasma-Assisted Chemical Vapour Deposition of Hard Coatings with Metallo-Organic Compounds, Materials Science and Engineering: A139, (1991), pp. 61-66.

[15] A. R. Barron, Atomic Layer Deposition, OpenStax CNX, 2009, http://cnx.org/contents/ae29812b-5c71-4740-ac36-6809c5282026@2@2.

[16] D. M. Mattox, Handbook of Physical Vapor Deposition (PVD) Processing (Second Edition), Elsevier, 2010.

[17] M. Y. Arrieta, (2012) Low Temperature Chemical Vapor Deposition of Zirconium Nitride in a Fuidized Bed, M.S. Thesis, Texas A&M University, College Station, TX.

[18] D. Kunii, O. Levenspiel, Fluidization Engineering, Butterworth-Heinemann, Newton, MA, 1991.

[19] Y. Xu, X.-T. Yan, Chemical Vapour Deposition, An Integrated Engineering Design for Advanced Materials, Springer-Verlag, London, 2010.

[20] H. O. Pierson, Handbook of Chemical Vapor Deposition (CVD) - Principles, Technology and Applications (2nd Edition), Elsevier Science, 2000.

[21] L. G. Gibilaro, Fluidization Dynamics: The Formulation and Applications of a Predictive Theory for the Fluidized State, Butterworth-Heinemann, 2001.

[22] W-C. Yang, Handbook of Fluidization and Fluid-Particle Systems, Marcel Dekker, 2003.

[23] A. Lucas, J. Arnaldos, J. Casal, L. Pulgjaner, Improved Equation for the Calculation of Minimum Fluidization Velocity, Industrial and Engineering Chemistry Process Design and Development, 25, (1986), pp. 426-429.

[24] Y. Kumashiro, K. Inagawa, Electric Refractory Materials: Thin Film Preparation, Marcel Dekker, Inc., 2000.

[25] A. Leenaers, S. Van den Berghe, C. Detavernier, Surface Engineering of Low Enriched Uranium-Molybdenum, Journal of Nuclear Materials, 440, (2013), pp. 220-228.

[26] D. D. Keiser, E. Perez, T. Weincek, A. Leenaers, S. Van den Berghe, Microstructural Characterization of a Thin Film ZrN Diffusion Barrier in an As-Fabricated U-7Mo/Al Matrix Dispersion Fuel Plate, Journal of Nuclear Materials, 458, (2015), pp. 406-418.

[27] H. B. Profijt, S. E. Potts, M. C. M. van de Sanden, W. M. M. Kessels, Plasma-Assisted Atomic Layer Deposition: Basics, Opportunities, and Challenges, Journal of Vacuum Science and Technology A: Vacuum, Surfaces, and Films, 29, (2011).

[28] J. Becker, S. Suh, S. I. Wang, R. G. Gordon, Highly Conformal Thin Films of Tungsten Nitride Prepared by Atomic Layer Deposition from a Novel Precursor, Chemistry of Materials, 15, (2003), pp. 2969-2976.

[29] S. E. Potts, C. J. Carmalt, C. S. Blackman, F. Abou-Chahine, N. Leick, W. M. M. Kessels, H. O. Davies, P. N. Heys, Bis(cyclopentadienyl) Zirconium(IV) Amides as Possible Precursors for Low Pressure CVD and Plasma-Enhanced ALD, Inorganica Chimica Acta, 363, (2010), pp. 1077-1083.

[30] S. Cho, K. Lee, P. Song, H. Jeon, Y. Kim, Barrier Characteristics of ZrN Films Deposited by Remote Plasma-Enhanced Atomic Layer Deposition Using Tetrakis(diethylamino)zirconium Precursor, Japanese Journal of Applied Physics, 46, (2007), pp. 4085-4088.

[31] B. Karlsson, R. P. Shimshock, B. O. Seraphin, Optical Properties of CVD-Coated TiN, ZrN, and HfN, Solar Energy Materials, 7, (1983), pp. 401-411.

[32] R. Fix, R. G. Gordon, D. M. Hoffman, Chemical Vapor Deposition of Titanium, Zirconium, and Hafnium Nitride Thin Films, Chemistry of Materials, 3, (1991), pp. 1138-1148.

[33] B. R. Westphal, R. D. Mariani, Method for the Production of Uranium Chloride Salt, U. S. Patent US 8475756 B1, U. S. Department of Energy, (2013).

[34] C. B. Alcock, Thermochemical Processes: Principles and Models, Elsevier Butterworth-Heinemann, 2001.

[35] I.-W. Kim, S.-J. Kim, D.-H. Kim, H. Woo, M.-Y. Park, S.-W. Rhee, Fourier Transform Infrared Spectroscopy Studies on Thermal Decomposition of Tetrakis-dimethyl-amido Zirconium for Chemical Vapor Deposition of ZrN, Korean Journal of Chemical Engineering, 21, (2004), pp. 1256-1259.

[36] H. Berndt, A.-Q. Zeng, H.-R. Stock, P. Mayr, Zirconium Carbonitride Films Produced by Plasma-Assisted Metal Organic Chemical Vapour Deposition, Surface & Coatings Technology, 74-75, (1995), pp. 369-374.

[37] K. T. Rie, J. Wöhle, and A. Gebauer, Synthesis of Thin Coatings by Plasma-Assisted Chemical Vapour Deposition using Metallo-Organic Compounds as Precursors, Surface and Coatings Technology, 59, (1993), pp. 202-206.

[38] NIST Chemistry WebBook, NIST Standard Reference Database Number 69 (2015).

[39] L. Dubois, Model Studies of Low Temperature Titanium Nitride Thin Film Growth, Polyhedron, 13, (1994), pp. 1329-1336.

[40] R. N. Guillemette, "Electron Microprobe Techniques," Methods of Soil Analysis, Part 5- Mineralogical Methods., Soil Science of America, Madison, WI, 2008.

[41] NIST Inorganic Crystal Structure Database, NIST Standard Reference Database 84, (2013).

[42] D. Crawford, TAMU Particles 3-12-2014, Idaho National Laboratory, Personal communication.

[43] O. Mireles, Nuclear and Emerging Technologies for Space 2014, Personal communication.

APPENDIX A

X-RAY DIFFRACTION SPECTRA

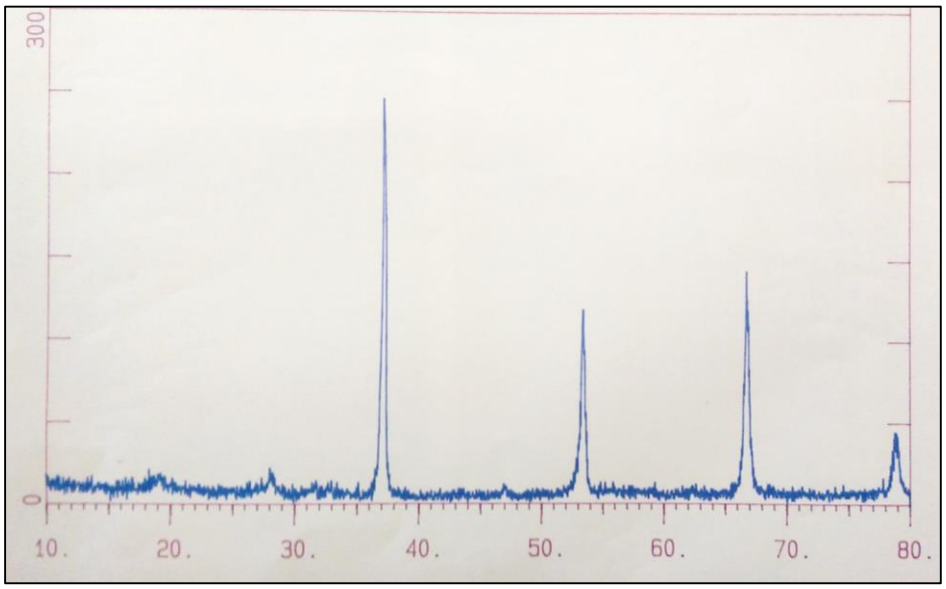

Figure A-0-1. Uncoated U-Mo XRD spectrum.

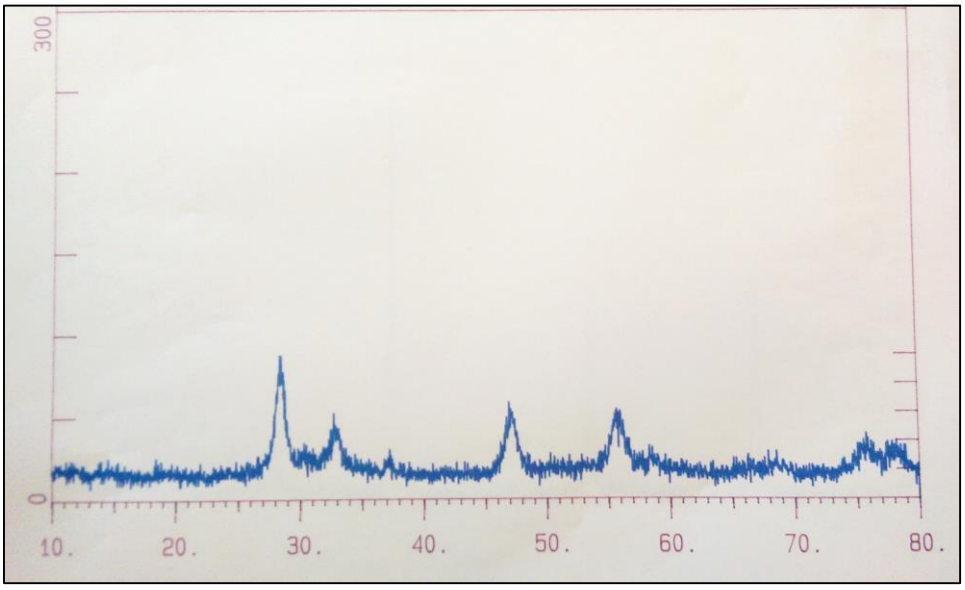

Figure A-0-2. Exp. 5 coated XRD spectrum.